DYNAMICS OF SMECTIC MEMBRANES AS STUDIED BY X-RAY AND NEUTRON SCATTERING

DYNAMICS OF SMECTIC MEMBRANES AS STUDIED BY X-RAY AND NEUTRON SCATTERING

PROEFSCHRIFT

ter verkrijging van de graad van doctor aan de
Technische Universiteit Eindhoven, op gezag van de
Rector Magnificus, prof.dr. R.A. van Santen, voor een
commissie aangewezen door het College voor
Promoties in het openbaar te verdedigen
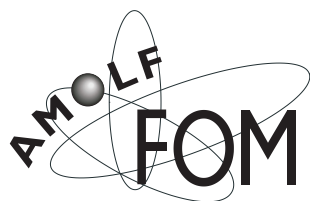op vrijdag 25 februari 2005 om 16.00 uur

door

Irakli Sikharulidze

geboren te Tbilisi, Georgië

Dit proefschrift is goedgekeurd door de promotoren:

prof.dr.ir. W.H. de Jeu
en
prof.dr. B.M. Mulder

'Well, I'll eat it,' said Alice,

'and if it makes me grow larger, I can reach the key;

and if it makes me grow smaller, I can creep under the door;

so either way I'll get into the garden,

and I don't care which happens!'

Alice's adventures in wonderland

Lewis Carroll

To my parents

This thesis is based on the following articles:

Chapters 3, 4, 5

I. Sikharulidze and W. H. de Jeu,

Dynamics of fluctuations in smectic membranes,

Physical Review E, (submitted).

Chapters 2, 6

I. Sikharulidze, I. P. Dolbnya, A. Madsen, and W. H. de Jeu,

X-ray photon correlation spectroscopy in a reflection geometry: Coherence and resolution,

Optics Communications **245**, in press (2005).

Chapter 6

W. H. de Jeu, A. Madsen, I. Sikharulidze and S. Sprunt,

Heterodyne and homodyne detection in fluctuating smectic membranes by photon correlation spectroscopy at x-ray and visible wavelengths,

Physica B **355**, in press (2005).

Chapter 5

I. Sikharulidze, B. Farago, I. P. Dolbnya, A. Madsen and W. H. de Jeu,

Surface and bulk-elasticity determined fluctuation regimes in smectic membranes,

Physical Review Letters **91**, 165504 (2003).

Chapter 5

I. Sikharulidze, I. P. Dolbnya, A. Fera, A. Madsen, B. I. Ostrovskii and W. H. de Jeu,

Smectic membranes in motion: approaching the fast limits of x-ray photon correlation spectoscopy,

Physical Review Letters **88**, 115503 (2002).

Contents

Chapter 1

Introduction

In this introductory chapter we summarize the main concepts that play a role in the work to be discussed in this thesis. First, we summarize the basics of smectic phases and smectic membranes. Then the nature of the smectic ordering and the associated fluctuation behavior is discussed. Next, after a summary of x-ray reflectivity of smectic membranes, the coherent properties of x rays are considered. This allows us to introduce photon correlation spectroscopy with coherent x rays, which is a main tool used in this thesis. The chapter finishes with an outline of the rest of the thesis.

1.1   Smectic liquid crystals

In a particular temperature range some substances exhibit properties characteristic of both the liquid and the crystal state. On the one hand, they behave like liquids as they flow and take the shape of the vessel they are poured in. On the other hand, they possess typical properties of a crystal like anisotropy of mechanical and optical properties. Materials exhibiting such a state are known as liquid crystals [1, 2]. The Smectic A (SmA) phase is formed by liquid crystals consisting of elongated molecules. In Fig. 1.1 we give three examples of such compounds that play an important role in the investigations to be described in this thesis. The SmA phase consists of stacks of liquid layers made up of molecules with their principal axis oriented on average perpendicular to the layers (see Fig. 1.2). The direction defined by the long axes is called the director. The molecules possess no positional order in the planes of the layers. The

K 33 CrB 48.5 SmA 63.5 N 73 I

4O.8

K 72 SmC 79 SmA 129 I
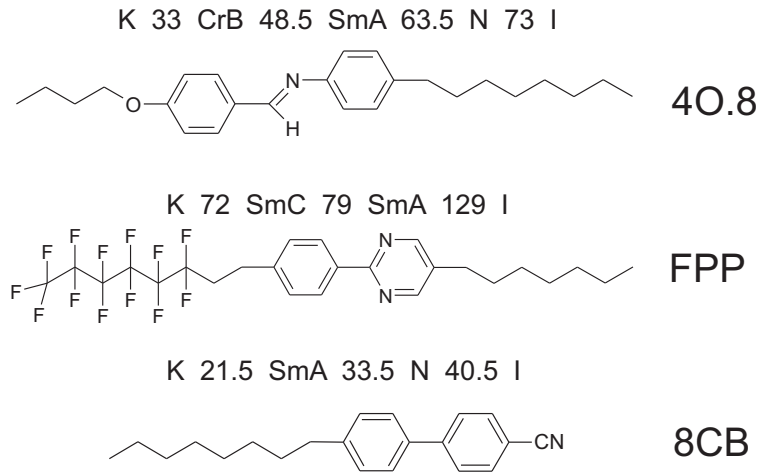
FPP

K 21.5 SmA 33.5 N 40.5 I

8CB

Figure 1.1: The compounds 4O.8, FPP and 8CB with their phase transition temperatures in °C. I stands for the isotropic phase, N for nematic, SmA and SmC for smectic A and smectic C, respectively, CrB for crystalline B and K for regular crystal phases.

periodic density profile $\rho(\mathbf{r})$ of SmA can be represented in terms of the Fourier series:

$$\rho(\mathbf{r}) = \rho_0(1 + \psi e^{-iq_0(z - u(\mathbf{r}))} + \text{c.c.} + \ldots), \tag{1.1}$$

where q_0 is defined by the smectic layer spacing d as $q_0 = 2\pi/d$, $u(\mathbf{r})$ is the displacement of a smectic layer parallel to the layer normal, away from its equilibrium position, ρ_0 is the average density and ψ the Fourier amplitude. For most applications higher order terms in Eq. (1.1) can be omitted. The order parameter of the smectic phase can be introduced as $\psi(\mathbf{r}) = |\psi| \exp(-iq_0 u(\mathbf{r}))$.

A unique property of smectic liquid crystals is their ability to form films that are freely suspended or free-standing over an aperture in a frame (smectic membranes). This property has been known since the beginning of the last century. Friedel [3] used it in his monograph on liquid crystals as an argument in favor of the existence of layers in the smectic phase. However, it was not before the 1970s that such films found extensive usage in experimental studies [4–6]. Some reviews are given in Ref. [7, 8]. The smectic layers align parallel to the two air-film surfaces, which are flat because the surface tension minimizes the surface area of the film. Apart from the edges, such films can be considered as substrate-free and they can be seen as membranes consisting of stacks of smectic layers. They have a high degree of uniformity: the alignment of the smectic layers is almost perfect, allowing to study single-domain samples of various thickness. The surface area can be as large as a thousand mm^2, while the thickness can be easily varied from thousands of layers (tens of μm) down to two layers (about 5 nm).
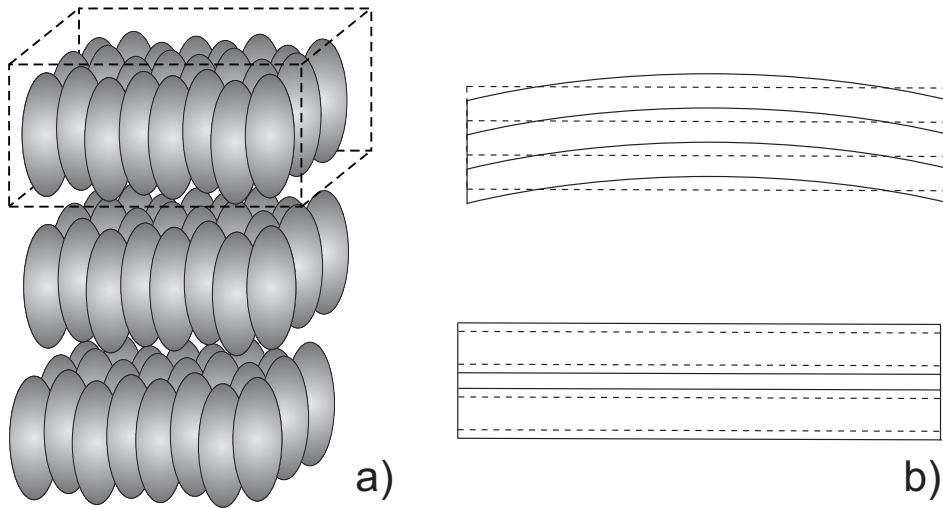
Figure 1.2: SmA phase model models. a) Molecular organization. b) Types of deformation: bending (top) and compression (bottom); the broken lines indicate the equilibrium positions of the layers.

The layered structure of SmA liquid crystals leads to the presence of an elastic energy associated with the ordering. As the layers are fluid, displacements of the molecules within these layers do not cost energy. Hence, for a displacement $u(\mathbf{r})$ we can expect the SmA free energy to depend only on its components along the director. Because translations of the membrane as a whole do not cost any elastic energy terms containing $u(\mathbf{r})$ are absent. Rotation around x or y axis with (x, y) plane parallel to the smectic layers also do not change the free energy. Consequently, terms $\nabla_x u(\mathbf{r})$ and $\nabla_y u(\mathbf{r})$ will be absent in the SmA free energy. The main contributions are given by compression and bending of the smectic layers as illustrated in Fig. 1.2b. The free energy corresponding to these deformations is known as the Landau-de Gennes free energy [1, 9]:

$$F_B = \frac{1}{2} \int\limits_V d^3\mathbf{r} \left\{ B[\nabla_z u(\mathbf{r})]^2 + K[\Delta_{xy} u(\mathbf{r})]^2 \right\},$$ (1.2)

where B and K are elastic constants and V denotes the volume of the sample. The first term in this equation corresponds to the compression energy of the membrane and the second term gives the contribution from the bending energy. In a smectic membrane with a finite thickness L we have extra contributions to the free energy due to the surface tension [10]. These can be expressed as:

$$F_S = \frac{1}{2} \int\limits_S d^2\mathbf{r} \, \gamma \left\{ [\nabla_{xy} u(\mathbf{r})|_{z=-L/2}]^2 + [\nabla_{xy} u(\mathbf{r})|_{z=L/2}]^2 \right\},$$ (1.3)

where γ is the surface tension and S represents the surface of the membrane. The total free energy F of a SmA membrane

$$F = F_B + F_S$$ (1.4)

is referred as the Landau-de Gennes-Hołyst free energy and is at the basis of all further discussions of fluctuations in smectic membranes.

1.2 Landau-Peierls instability

In a three-dimensional (3D) crystal the particles vibrate around well-defined lattice positions with amplitudes small compared to the lattice spacing. As the dimensionality of the system is decreased, fluctuations become increasingly important. As a result long-range translational order cannot exist in 2D and 1D; it would be destroyed by thermal fluctuations. The spatial dimension at which thermal fluctuations just prevent the existence of long-range order is called the lower marginal dimensionality. In this case, the positional correlations decay algebraically as a function of distance. Low-dimensional ordering and the associated fluctuation behavior are of considerable interest and can also be observed in 3D systems that are ordered in one direction only. Smectic liquid crystals belong to this class and are often used as model systems of specific types of ordering as they provide a variety of different phases and phase transitions.

On the basis of the Landau-de Gennes free energy we can investigate the stability of the smectic structure with respect to the fluctuations of the system. Let us consider the displacement of the smectic layers $u(\mathbf{q})$ expressed through their Fourier components:

$$u(\mathbf{r}) = \int \frac{d^3\mathbf{q}}{(2\pi)^3} \tilde{u}(\mathbf{q}) e^{i\mathbf{q}\cdot\mathbf{r}}. \tag{1.5}$$

Using this representation, the Landau-de Gennes free energy can be rewritten in the following form:

$$F = \frac{1}{2} \int \frac{d^3\mathbf{q}}{(2\pi)^3} (Bq_z^2 + Kq_{xy}^4)|\tilde{u}(\mathbf{q})|^2. \tag{1.6}$$

Each term in this sum corresponds to an independent fluctuation with a wave vector $\mathbf{q}$, which according to the equipartition theorem has an energy of $k_B T/2$. This defines the amplitude of each Fourier component:

$$|\tilde{u}(\mathbf{q})|^2 = \frac{k_B T}{Bq_z^2 + Kq_{xy}^4}. \tag{1.7}$$

From this equation we can calculate the mean-square displacement of the smectic layers:

$$\langle u^2(\mathbf{r}) \rangle = \int\limits_0^\infty dq_z \int\limits_0^\infty dq_{xy} \frac{q_{xy}}{(2\pi)^2} \frac{k_B T}{Bq_z^2 + Kq_{xy}^4}. \tag{1.8}$$

For small values of q_{xy} and q_z the integrals diverge because the Fourier amplitude $|\tilde{u}(\mathbf{q})|$ tends to infinity (infrared divergence). In case of a infinite membrane the fluctuation amplitude diverges logarithmically with its thickness:

$$\langle u^2(\mathbf{r}) \rangle = \frac{k_{\mathrm{B}}T}{8\pi\sqrt{KB}} \ln\left(\frac{L}{d}\right). \tag{1.9}$$

This expression indicates that long-wavelength fluctuations destroy the smectic layering as soon as the mean-square amplitude becomes of the order of the layer spacing. This effect is known as the Landau-Peierls instability [11, 12].

Strong fluctuations have a direct impact on the nature of the ordering in the system under investigation. This can be expressed in terms of the order parameter correlations that vanish with distance. Defining the order-parameter correlation function $G(\mathbf{r}) = \langle \psi(\mathbf{r})\psi^*(0) \rangle$ we can distinguish the following cases for a system of dimensionality p:

$$G(\mathbf{r}) \overset{|\mathbf{r}|\to\infty}{=} \begin{cases} \text{const}, & (p > 2), \\ |\mathbf{r}|^{-\eta}, & (p = 2), \\ \exp(-|\mathbf{r}|/\xi), & (p = 1). \end{cases} \tag{1.10}$$

The first case $p > 2$ corresponds to long-range order in the system because finite correlations extend to arbitrarily large distances. In the case $p = 1$ the correlations decay exponentially. In this situation we find a short-range order with the parameter ξ indicating the characteristic distance over which the correlations disappear. The case $p = 2$ corresponds to an intermediate situation. On the one hand the correlations decay algebraically and we cannot introduce a distance like ξ because the correlations decay slower than exponentially. In other words, the correlation length ξ is infinite, as for long-range order. On the other hand, the correlations disappear at infinity. This situation is commonly referred as quasi-long-range order. The transition from quasi to true long-range order occurs at the marginal dimensionality, for the present example given by $p = 2$. It originates from the infrared divergence in integrals similar as in Eq. (1.8). Hence, for a particular system its value depends on the actual form of the free energy.

The algebraic decay of the smectic layer ordering [13, 14] was demonstrated by measurements are the slow decay of the scattering around a Bragg position [15–17]. Apart from smectics, this behavior can also be observed in other systems for which the divergence of the Fourier amplitudes of long-wavelength fluctuations leads to divergence of the mean-square displacement. This includes a wide variety of systems comprising Langmuir films, Newtonian black

films, and surfactant and lipid membranes [8, 18]. The dynamics of the fluctuations in smectic membranes constitute the central issue in the investigations reported in this thesis.

1.3 X-ray reflectivity

X-ray reflectivity is a powerful technique to investigate the structure of layered systems like smectic membranes. X rays scattered from the different layers lead to the formation of an interference pattern (see Fig. 1.3a). The profile of this interference picture depends on the layer spacing and the electron density of the layers. In x-ray reflectivity measurements, we refer to the scattering configuration as specular reflectivity when the incident angle is equal to the reflected one. The reflectivity, defined as the ratio of the intensity of the scattered and the incident beam, can be expressed in terms of the electron density profile of the sample in the scattering plane $\rho(z)$ [19]:

$$R = \frac{4\pi}{q_z^2} \int_{-\infty}^{\infty} \frac{d\rho(z)}{dz} \exp(-iq_z z)dz. \tag{1.11}$$

Figure 1.3b shows an example of a reflectivity curve. This curve exhibits three distinct fea-
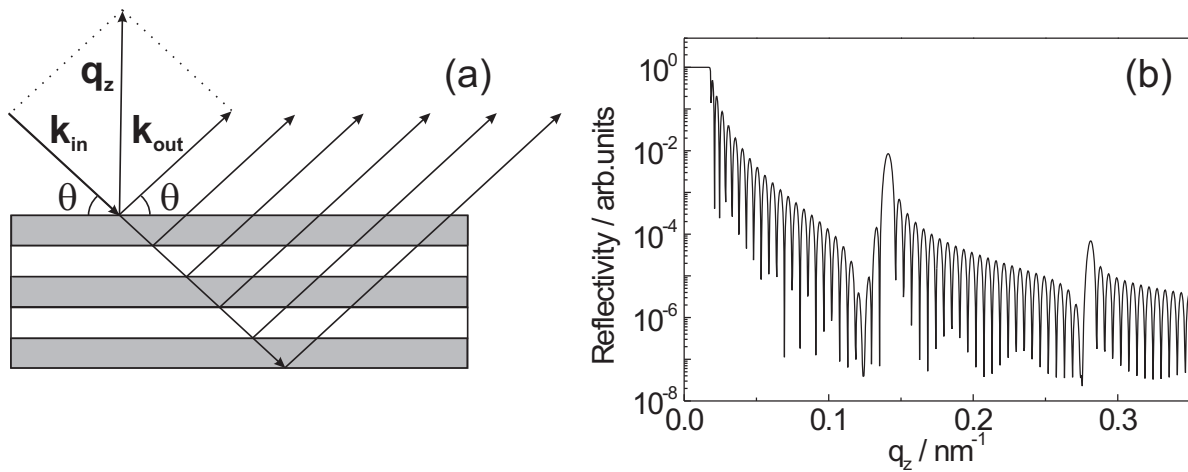
Figure 1.3: X-ray reflectivity. a) Scattering geometry in which $\mathbf{k_{in}}$ and $\mathbf{k_{out}}$ are the wave vectors of the incident and scattered beams, respectively; $\mathbf{q} = \mathbf{q_z} = \mathbf{k_{out}} - \mathbf{k_{in}}$ is the scattering vector. b) Calculated reflectivity curve for a 25-layer membrane.

tures. At small scattering angles a region of total external reflection is observed, where the reflectivity is equal to unity. This occurs because the refractive index of materials in the x-ray region is slightly smaller than one. At larger scattering angles we observe a series of oscillations. They originate from the interference of waves scattered from the membrane layers. The high-frequency oscillations are known as Kiessig fringes. They result from interference of

waves scattered at the top and bottom surfaces of the membrane. From the periodicity Δq_z of the Kiessig fringes one can calculate the thickness of the membrane using:

$$\Delta q_z = q_0/N = 2\pi/L, \tag{1.12}$$

where $N = L/d$ is the number of layers. The two pronounced maxima in Fig. 1.3b are Bragg reflections. They result from the interference of waves scattered from the periodic electron density variation associated with the layer structure. Inhomogeneities of the sample and roughness
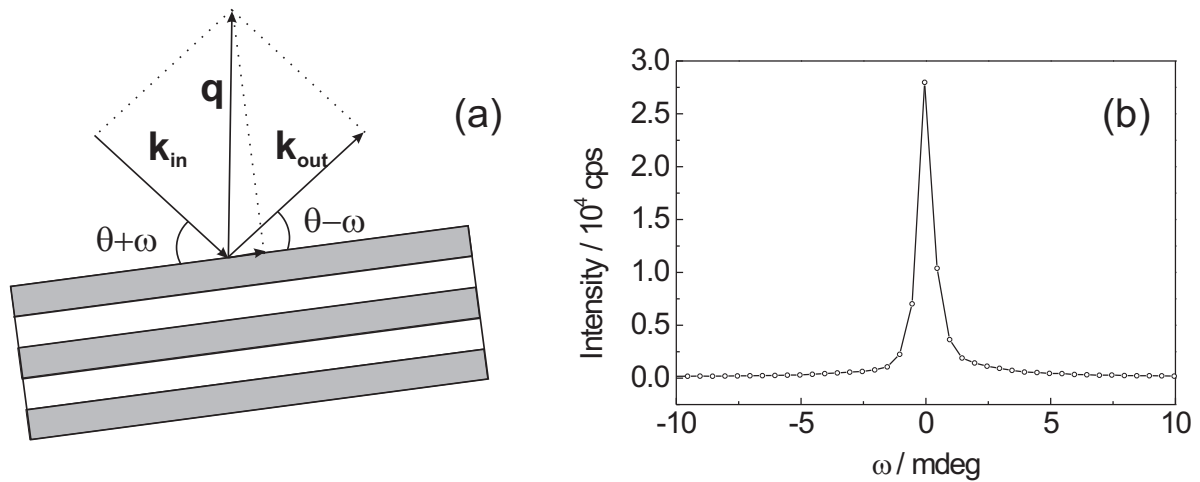

*Figure 1.4: Rocking scans. a) Scattering geometry in which $\mathbf{q} = (q_{xy}, q_z)$ and ω is the rocking angle. b) Experimental rocking curve of a 13-layer FPP membrane at the Bragg position. The almost perfect uniformity is reflected in the full-width at half maximum of 0.7 m*deg.

of the surfaces lead to smearing of the Kiessig fringes. The uniformity of a sample can be assessed by measuring a rocking curve. Such a curve is obtained by rocking the sample around a specular position. In this experiment a finite projection of the scattering vector on the surface of the membrane is created. Figure 1.4 shows an example of a rocking curve from a smectic membrane. The width of 0.7 mdeg reflects the mosaic distribution of the layer normals. The small value indicates that the sample is highly uniform. The main contribution to the width of the rocking curve comes from curvature induced by the non-perfect planarity of the supporting frame. The intensity at off-specular positions is due to diffuse scattering.

The average effects of the fluctuations in smectic membranes have been extensively investigated by static x-ray scattering [20–23]. An important result is that under most practical circumstances the fluctuations of the smectic layers are conformal: the layers fluctuate throughout the membrane 'unisono'. Evidently, a loss of conformality is expected at very thick membranes. In

thin membranes it has been observed by off-specular (diffuse) x-ray reflectivity for fluctuations with a small in-plane wavelength below about $30-50$ nm.

1.4   Coherence of x-rays

Coherence is an important concept for the description of static and time-resolved scattering experiments. Superposition of waves with different phases leads to the phenomenon of interference. In the classical interpretation, the interference patterns are produced as a result of superposition of secondary waves generated in the sample. In the ideal case the incident wave has a constant frequency and originates from either a point source (spherical wave) or a source at infinity (plane wave). In that situation the phases in any two points of the wave and at any two times are fully correlated. In reality, a light beam represents a superposition of waves generated by a source that is composed of many correlated or chaotic emitters positioned at a finite distance from the observer. In such a situation correlations between the phase at two different points decrease as they become more distant and as the time intervals between the measurements increases. The term coherence defines to which extent such a real beam resembles a single wave. The coherence is expressed in two length scales: the longitudinal (temporal) and the transversal (spatial) coherence length (see Fig. 1.5).

The longitudinal coherence length defines the distance between two points along the propagation direction of the beam over which the correlation between the phases is lost. An equivalent picture uses the coherence time, defined as the time interval for which phase correlations are lost at a fixed point. Such a decorrelation of the phases can occur because of superposition of waves with different frequencies. We denote the frequency spread in the beam as $\Delta\omega$ and consider waves to be out of phase if the phase difference reaches π. The coherence time is given as $t_{\mathrm{coh}} = \pi/\Delta\omega$. Using the relation $\Delta\omega = (2\pi c/\lambda^2)\Delta\lambda$, where c is the speed of light, we can express the longitudinal coherence length in the following form:

$$\xi_l = ct_{\mathrm{coh}} = \frac{\lambda^2}{2\Delta\lambda}. \tag{1.13}$$

Other conventions for the definition of the out-of-phase waves (for example, a phase difference 2π instead of π), lead to a difference of a factor two in this equation. The value of ξ_l defines the maximum path-way difference allowing the observation of interference phenomena. For modern lasers ξ_l can extend up to a few kilometers, while in x-ray region it is of the order of

a few microns. Still this value is large enough to allow us to observe Kiessig fringes in x-ray reflectivity experiments for membranes up to a thickness of several tens of microns.
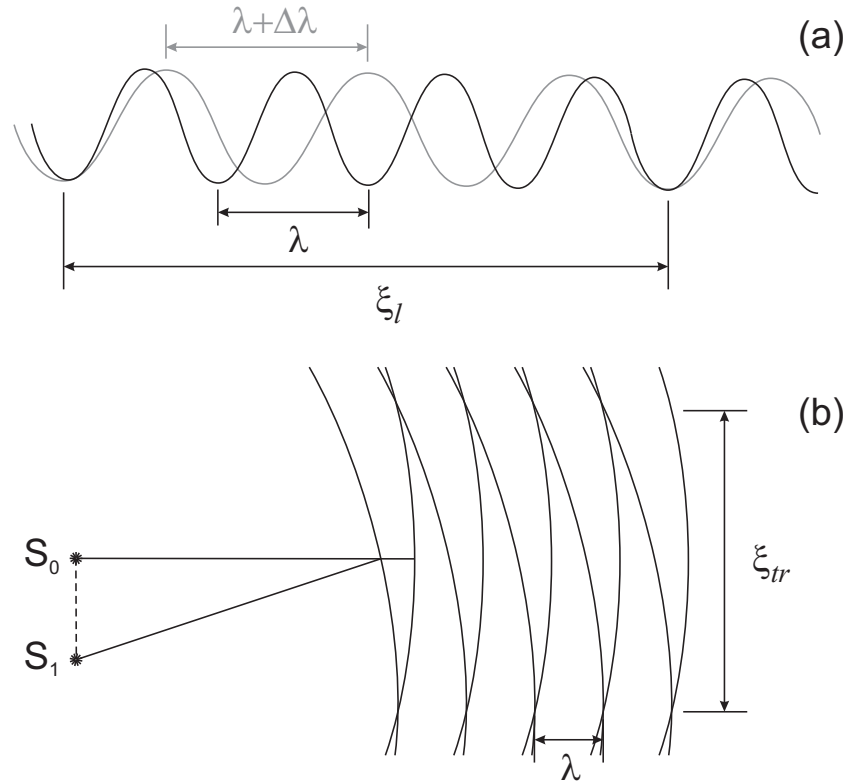

Figure 1.5: Coherence of waves. a) Longitudinal coherence. b) Transversal coherence.

The transverse coherence length defines the maximum distance of the phase correlations in the propagating wave along the wavefront. An extended source can be treated as a collection of point sources distributed over some area in space between S_0 and S_1 (see Fig. 1.5b). Moving across the wavefront created by S_0 we encounter changes of the phase of the wave propagating from S_1 (and in between). The distance over which the phases from these extreme positions change by factor π defines the transverse coherence length ξ_{tr}. If the size of the source is denoted by σ, the transverse coherence length at a distance R from the source is defined as:

$$\xi_{tr} = \frac{\lambda R}{2\pi\sigma} \tag{1.14}$$

The value of ξ_{tr} defines the maximum size of a spatially coherent beam that can be obtained from a given source. For lasers ξ_{tr} can be as large as a few meters, while the largest value for x rays achieved at modern synchrotron sources is just over 100 μm. In the x-ray regime spatially coherent beams can only be created at considerable cost of intensity, as one has to slit down the beam to submillimeter dimensions.

1.5   Time-resolved scattering techniques

Fluctuations lead to rearrangement of the scatterers in a sample that can be detected using various time-resolved scattering techniques [24, 25]. Scattering of spatially coherent light from a sample produces an image known as speckle pattern. It usually consists of an inhomogeneous distribution of the scattered intensity, which corresponds to the positions of the scatterers inside the coherence volume. If the scatterers move, the resulting intensity profile will change in time. Recording these intensity fluctuations one can calculate the intensity-intensity time correlation function (see Fig. 1.6). From this function one can deduce the characteristic decay time of the correlations τ describing the dynamics of the system. This principle lies at the basis of photon correlation spectroscopy (PCS). For successful measurements only a few coherence volumes should be present in the illuminated area, which requires a spatially coherent beam. Scattering from different coherence volumes smears out the speckle pattern resulting in an ensemble-averaged intensity profile. For ergodic systems this average is equal to the time-averaged intensity profile and the time-correlation function will tend to unity.
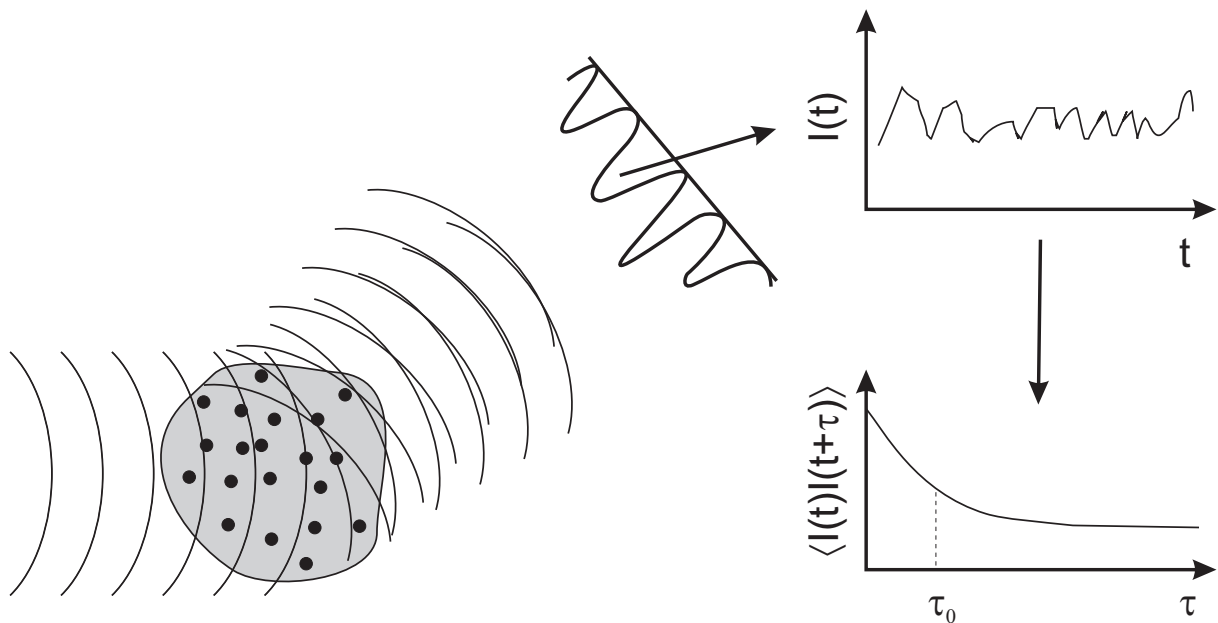
Figure 1.6: Principle of photon correlation spectroscopy.

Apart from the speckle pattern, scattering from a moving medium results in a frequency shift of the scattered light (Doppler effect). From measurements of this shift, one can also deduce information about the dynamics of the system. This can be achieved by filtering, in which a dispersive element like a diffraction grating is used to measure the frequency shifts directly, or by optical mixing. In latter case we can distinguish two measurement schemes:

homodyne and heterodyne detection. In the homodyne case, only the fluctuating scattered intensities are correlated, while in the heterodyne scheme the scattered signal containing a frequency shift is mixed with a reference signal. For PCS in the optical range (dynamic light scattering), heterodyne detection is widely preferred above homodyne detection as it provides higher sensitivity for weak scattered signals.
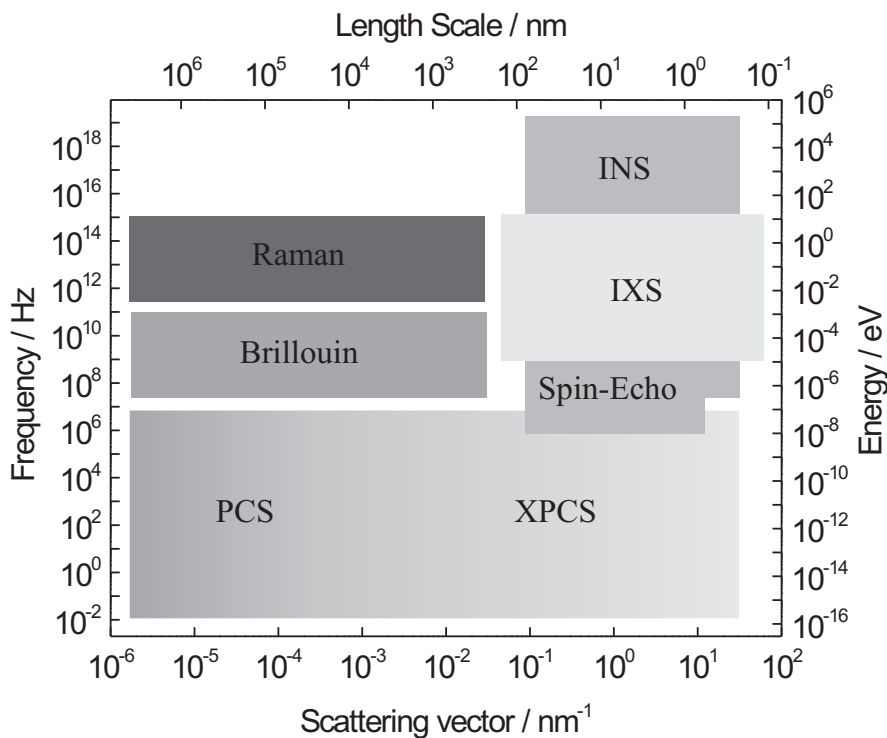
Figure 1.7: Time-resolved scattering techniques [26].

X-ray photon correlation spectroscopy (XPCS) is a relatively new, promising technique for studying dynamics in condensed matter systems, extending classical optical PCS into the x-ray domain [26–34]. In recent years several publications have appeared reporting results of the application of XPCS to hard [35–38] and soft [39–55] condensed matter systems. First experiments probing the dynamics of the fluctuations in smectic membranes using XPCS were carried out by Sorensen et al. [56] using soft x rays, and by de Jeu and coworkers using conventional x rays [57–59]. Dynamic light-scattering studies of smectic membranes with laser light were carried out by Böttger and Joosten [60] and Nallet, Roux and Prost [61]. XPCS provides a unique combination of length and timescales to be probed, which are not accessible by other techniques (see Fig. 1.7), enabling the possibility to probe 'slow' dynamics at molecular length scales. In contrast to visible light x rays can be used to measure opaque samples. Moreover x rays do not suffer from multiple scattering that complicates the data analysis. However, a

major problem in performing XPCS is the lack of x-ray lasers and the fact that x rays are scattered much weaker compared to visible light. These factors generally lead to the absence of strong signals in XPCS measurements. As a result XPCS is only possible using high intensity beams provided at undulator beamlines of modern third-generation synchrotrons. In this context smectic membranes provide excellent model systems for XPCS for which the intensity problem is partly overcome. The nearly perfect ordering provides strong x-ray reflections that can be utilized in XPCS, while smectic membranes also exhibit exceptional stability against beam damage.

1.6   This thesis

This thesis is concerned with the dynamics of fluctuations in SmA liquid crystal membranes. The ability of smectic liquid crystals to form free-standing membranes with a high degree of uniformity makes them very suitable model systems of low-dimensional ordering. The effects of the marginal dimensionality make a decisive impact on the fluctuations of the smectic layers. Moreover, quantization due to the finite thickness of smectic membrane leads to rich behavior in terms of fluctuation modes. Different factors as inertia, surface tension and the smectic elasticity are dominant for different wavelength ranges of the fluctuations, providing a range of different relaxation behavior. This variety in relaxation dynamics of smectic membranes provides in turn a great platform to evaluate the potential of XPCS. By extending the range of XPCS to short times in the range of tens of nanoseconds, also a comparison with Neutron spin echo (NSE) techniques could be made [58, 59].

The outline of this thesis is as follows: In chapter 2 we present the theory underlying XPCS and NSE experiments. We describe how the results of both techniques can be analyzed in terms of intermediate scattering function $S(\mathbf{q}, t)$. For XPCS we underline two detection schemes: homodyne and heterodyne. We discuss the conditions for which each of these schemes is realized and the role of the spatial coherence in XPCS experiments.

In chapter 3 we discuss the experimental setup used for XPCS and NSE measurements at the European Synchrotron Radiation Facility (ESRF, Grenoble) and at the Institute Laue-Langevin (ILL, Grenoble), respectively. Particular attention is given to the description of scattering geometry in these experiments. Chapter 3 also contains a description of the smectic liquid crystal compounds investigated and the temperature controlled sample holders used. In addition, we review the influence of an x-ray beam on the stability of smectic membranes.

In chapter 4 the theory of the fluctuations in smectic membranes is presented. We relate $S(\mathbf{q}, t)$ to the smectic layer displacement correlation function. We evaluate $S(\mathbf{q}, t)$ using a continuum theory of liquid crystals based on the Landau-de Gennes free energy. Three relaxation regimes are derived for smectic membranes: oscillatory, surface dominated exponential and bulk-elasticity dominated exponential regimes. We analyze the influence of fluctuations with different wavelengths on the intensity correlation function.

In chapter 5 measurements are presented indicating three different relaxation patterns in SmA membranes. In thin samples, we observe fast relaxations with well-pronounced oscillations. In thicker samples, the oscillations become less pronounced, the relaxation times increase and the oscillations become slower. In 4O.8 and 8CB samples, we observed at the specular Bragg position a change from oscillatory to simple exponential relaxation after passing a critical sample thickness. In FPP membranes, for all accessible thickness at the specular Bragg position only oscillatory relaxations were detected. At off-specular positions only exponential relaxations were observed. An experimentally determined 'detection window' is introduced to explain the measurements.

In chapter 6 we take a closer look at the detection mechanism of membrane fluctuations in XPCS measurements. Considering that the speckle pattern generated by scattering of a spatially coherent beam from a smectic membrane can be disturbed only by fluctuations with a wavelength comparable or less than the size of the coherence volume, we show that experimental variations (like changing the detector slits) can result in shifts of the observed correlation functions.

Chapter 2

Time-resolved scattering techniques

In this chapter we introduce the theory describing x-ray photon correlation spectroscopy (XPCS) and neutron spin echo (NSE) experiments. The results are presented for both cases in terms of an intermediate scattering function and a smectic-layer-displacement correlation function. We also discuss the differences between homodyne and heterodyne detection schemes in XPCS and the influence of the spatial coherence and resolution of the x-ray scattering setup on XPCS measurements.

2.1 X-ray photon correlation spectroscopy

2.1.1 X-ray scattering

Intensity patterns observed in a scattering experiment are the result of interference of secondary waves emerging from the sample. Figure 2.1 shows the geometry corresponding to a scattering process. We assume that the distances from the source and to the detector are large compared to the size of the scattering volume. Hence, we consider scattering at the far field (Fraunhoffer case), for which the wave vectors $\mathbf{k_{in}}$ and $\mathbf{k_{out}}$ of the incident and scattered waves remain the same at all points of the sample. The total scattered electric field $E(\mathbf{q})$ is equal to a superposition of the secondary waves originating from the sample. If we consider two points A and B in the sample, then waves propagating from these two points will have a phase difference δ defined as:

$$\delta = \frac{2\pi}{\lambda}\left(\mathbf{k_{in}} \cdot \mathbf{r} - \mathbf{k_{out}} \cdot \mathbf{r}\right) = -\frac{2\pi}{\lambda}\mathbf{q} \cdot \mathbf{r}, \tag{2.1}$$

where $\mathbf{q} = \mathbf{k_{out}} - \mathbf{k_{in}}$ is the scattering vector and λ is the wavelength of the radiation. Taking
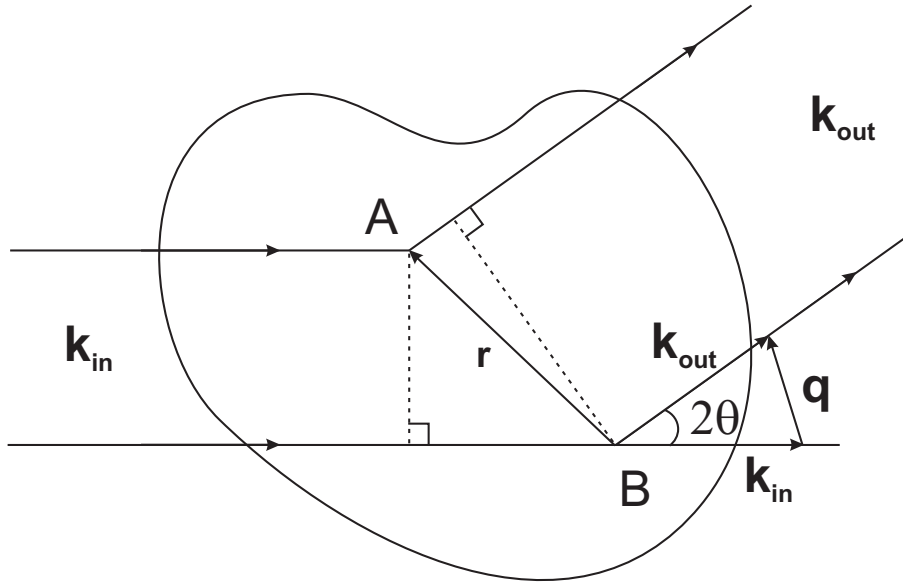
Figure 2.1: X-ray scattering experiment.

one point in the sample and summing up all the secondary waves taking into account the phase shifts given by Eq. (2.1), we can represent $E(\mathbf{q})$ in the following form:

$$E(\mathbf{q}) = E_0 r_{el} P(\theta) \frac{e^{ik_{out}R}}{R} \int_V \rho(\mathbf{r}) e^{i\mathbf{q}\cdot\mathbf{r}} d^3\mathbf{r}. \tag{2.2}$$

Here E_0 is the amplitude of the incident wave, $r_{el} = 2.818 \cdot 10^{-15}$ m is the classical electron radius, $P(\theta)$ is a constant factor related to the polarization of the incident wave and $\rho(\mathbf{r})$ is the electron density distribution in the sample.

The intensity of the scattered beam $I(\mathbf{q}) = \langle E(\mathbf{q})E^*(\mathbf{q})\rangle$ is defined by the structure factor $S(\mathbf{q})$ defined as:

$$S(\mathbf{q}) = \iint d^3\mathbf{r_1} d^3\mathbf{r_2} \langle \rho(\mathbf{r_1})\rho(\mathbf{r_2})\rangle e^{-i\mathbf{q}\cdot(\mathbf{r_1}-\mathbf{r_2})}, \tag{2.3}$$

where $\mathbf{r_1}$ and $\mathbf{r_2}$ are points in the scattering volume. In a cylindrical coordinate system $\mathbf{r} = (\mathbf{r}_{xy}, z) = (x, y, z)$ with the z-axis perpendicular to the surface of the membrane, the density profile of a smectic stack of liquid layers at position $z - nd$ can be represented as

$$\rho(\mathbf{r}_{xy}, z, t) = \rho_{layer}(z) * \sum_{n=0}^{N} \delta(z - nd - u(\mathbf{r}_{xy}, nd, t)). \tag{2.4}$$

Here n indicates a specific smectic layer, N the total number of layers, $u(\mathbf{r}_{xy}, nd, t)$ the displacement of the nth smectic layer from its equilibrium position, and $\rho_{layer}(z)$ the density profile of

a single smectic layer. Introducing Eq. (2.4) into the structure factor we obtain:

$$S(\mathbf{q}) = |\widetilde{\rho}_{layer}(q_z)|^2 \sum_{m,n} e^{i(m-n)dq_z} \iint d\mathbf{r}_{1,xy} d\mathbf{r}_{2,xy} e^{-i\mathbf{q}_{xy}\cdot(\mathbf{r}_{1,xy}-\mathbf{r}_{2,xy})}$$
$$\sum_{m,n} \exp\left\{-\frac{q_z^2}{2} g(\mathbf{r}_{1,xy} - \mathbf{r}_{2,xy}, md, nd)\right\}, \tag{2.5}$$

where $g(\mathbf{r}_{1,xy} - \mathbf{r}_{2,xy}, md, nd) = \langle[u(\mathbf{r}_{1,xy}, md, t) - u(\mathbf{r}_{2,xy}, nd, t)]^2\rangle$ is the static correlation function of the layer displacements and $\widetilde{\rho}_{layer}(q_z)$ represents the Fourier transform of the density profile of a single smectic layer. We can also define the dynamic correlation function $g(\mathbf{r}_{1,xy} - \mathbf{r}_{2,xy}, md, nd, t)$ by taking the displacements of the layers at different moments of time:

$$g(\mathbf{r}_{1,xy} - \mathbf{r}_{2,xy}, md, nd, t) = \langle[u(\mathbf{r}_{1,xy}, md, \tau) - u(\mathbf{r}_{2,xy}, nd, \tau + t)]^2\rangle \tag{2.6}$$

Using this dynamic correlation function in Eq. (2.5), we obtain the intermediate scattering function $S(\mathbf{q}, t)$, which plays a central role in time-resolved scattering measurements like XPCS and NSE.

2.1.2 Intensity-intensity time correlation function

XPCS experiments are based upon optical mixing as used in dynamic light scattering [24, 25]. The scattered intensity is integrated out at the detector without any prior filtering. The recorded intensity is fed into a hardware autocorrelator that computes the normalized intensity correlation function

$$g_2(t) = \frac{\langle I(\tau)I(\tau + t)\rangle}{\langle I(\tau)\rangle^2}, \tag{2.7}$$

where $I(t) = |E(t)|^2$ is the intensity at the detector. Similarly we can define

$$g_1(t) = \frac{\langle E(\tau)E^*(\tau + t)\rangle}{\langle I(\tau)\rangle}. \tag{2.8}$$

The time dependence in the field correlator in this equation is somewhat delicate. The phase of the wave in the incident beam is correlated on the scale of the coherence time t_{coh}, which is in our setup of the order of 10^{-14} s. Obviously any dynamic event to be measured is orders of magnitude slower at timescales for which the phases of the incident waves are not correlated anymore. To obtain useful information we should consider correlations of the amplitude of the scattered field only.

The intensity-intensity time correlator $\langle I(0)I(t)\rangle$ that determines XPCS experiments of smectic membranes is defined as

$$\langle I(0)I(t)\rangle = \frac{1}{T}\int_0^T d\tau\, E(\tau)E^*(\tau)E(t+\tau)E^*(t+\tau). \qquad (2.9)$$

In this equation, the scattered field $E(\tau)$ can be expressed as the Fourier transform of the density of the sample $\rho(\mathbf{r}, t)$ (see Eq. (2.2)). Consequently, the intensity correlator can be rewritten in the following form:

$$\langle I(0)I(t)\rangle = \iiiint d\mathbf{r}_1 d\mathbf{r}_2 d\mathbf{r}_3 d\mathbf{r}_4\, e^{-i\mathbf{q}(\mathbf{r}_1-\mathbf{r}_2)-i\mathbf{q}(\mathbf{r}_3-\mathbf{r}_4)}\langle \rho(\mathbf{r}_1,0)\rho(\mathbf{r}_2,0)\rho(\mathbf{r}_3,t)\rho(\mathbf{r}_4,t)\rangle. \qquad (2.10)$$

The integration is performed over the coherence volume, which can differ in size from the scattering volume. In the case of XPCS one would like to match the sizes of these two volumes. In the further discussion we assume that this is the case and use the terms coherence and scattering volume as synonyms.

A smectic membrane is homogeneous in the (x,y)-plane, while it has an inhomogeneous, layered structure in the z-direction. The density of a membrane can be split into two parts: $\rho(\mathbf{r}_{xy},z,t) = \rho_0(z,t) + \Delta\rho(\mathbf{r}_{xy},z,t)$, in which $\rho_0(z,t)$ represents the average displacement of a layer within the scattering volume in the z-direction at time t, and $\Delta\rho(\mathbf{r}_{xy},z,t)$ denotes time-dependent fluctuations. We assume that the membranes are incompressible and that all the layers undulate conformally ('unisono'). In this case $\rho_0(z,t)$ contains only translations of the scattering volume that do not change the scattered intensity, and we can drop the index n in the layer displacement function $u_n(\mathbf{r}_{xy},t)$. Then the total scattered field can be split in two parts:

$$E(t) = E_0(t) + \delta E(t), \qquad (2.11)$$

where $E_0(t)$ and $\delta E(t)$ correspond to $\rho_0(z,t)$ and $\Delta\rho(\mathbf{r}_{xy},z,t)$, respectively. In this situation we can consider $E_0(t)$ as a constant 'reference' signal. With this representation of the scattered field $g_1(\tau)$ and $g_2(\tau)$ take the following form:

$$g_1(t) = \frac{\langle \delta E(\tau)\delta E^*(\tau+t)\rangle}{\langle I_s\rangle}, \qquad (2.12)$$

$$g_2(t) = \frac{\langle \delta E(\tau)\delta E^*(\tau)\delta E(\tau+t)\delta E^*(\tau+t)\rangle}{\langle I_s\rangle^2}, \qquad (2.13)$$

where $I_0 = \langle E_0 E_0^* \rangle$ and $I_s = \langle \delta E(t) \delta E^*(t) \rangle$. Using these definitions and Eq. (2.11), the intensity correlator in Eq. (2.9) can be expressed in the form [62]:

$$\langle I(0)I(t) \rangle = (I_0 + I_s)^2 + 2I_0 I_s \mathrm{Re}[g_1(t)] + I_s^2[g_2(t) - 1].\qquad(2.14)$$

This formalism allows us to distinguish heterodyne and homodyne detection schemes. The heterodyne regime is characterized by $\delta E(t) \ll E_0$, for which situation the weak scattered intensity I_s is amplified by the strong reference signal I_0. Consequently, the last term in Eq. (2.14) can be omitted and the correlator is determined by $g_1(t)$. In the case of homodyne detection the reference signal I_0 is absent. Then the right-hand side in Eq. (2.14) equals $I_s^2 g_2(t)$. By definition I_0 is related to translations of the scattering volume and thus contributes in XPCS a δ-function-like signal at the specular position. By changing the scattering geometry we can either catch this reflection or not. In this way the presence of the reference signal I_0 can be controlled and the measurement can be switched between homodyne and heterodyne detection.

Both $g_1(t)$ and $g_2(t)$ can be expressed in terms of the density correlations in the membrane. The function $g_1(t)$ is proportional to the intermediate scattering function:

$$\langle \delta E(\tau) \delta E^*(\tau + t) \rangle \sim S(\mathbf{q}, t) = \int d\mathbf{r}_1 d\mathbf{r}_2 e^{-i\mathbf{q} \cdot (\mathbf{r}_1 - \mathbf{r}_2)} \langle \Delta\rho(\mathbf{r}_1, \tau) \Delta\rho(\mathbf{r}_2, \tau + t) \rangle,\qquad(2.15)$$

If we assume the density fluctuations $\Delta\rho(\mathbf{r}, t)$ to be Gaussian, we can express $g_2(t)$ as a function of $g_1(t)$. Using Wick's theorem to factorize the four-point density correlator in Eq. (2.10) [63], we obtain:

$$\begin{aligned}
\langle \Delta\rho(\mathbf{r}_1, 0) \Delta\rho(\mathbf{r}_2, 0) \Delta\rho(\mathbf{r}_3, t) \Delta\rho(\mathbf{r}_4, t) \rangle &= \langle \Delta\rho(\mathbf{r}_1, 0) \Delta\rho(\mathbf{r}_2, 0) \rangle \langle \Delta\rho(\mathbf{r}_3, t) \Delta\rho(\mathbf{r}_4, t) \rangle \\
&+ \langle \Delta\rho(\mathbf{r}_1, 0) \Delta\rho(\mathbf{r}_3, t) \rangle \langle \Delta\rho(\mathbf{r}_2, 0) \Delta\rho(\mathbf{r}_4, t) \rangle \\
&+ \langle \Delta\rho(\mathbf{r}_1, 0) \Delta\rho(\mathbf{r}_4, t) \rangle \langle \Delta\rho(\mathbf{r}_2, 0) \Delta\rho(\mathbf{r}_3, t) \rangle.
\end{aligned}\qquad(2.16)$$

Introducing this expansion into Eq. (2.10), $g_2(t)$ can be written as a sum of three terms: $g_2(t) = I_1 + I_2 + I_3$, each of which is the Fourier transform of the corresponding term in Eq. (2.16). In I_1 the two positions in the correlators are taken at the same time. Consequently, after time averaging they become time-independent and I_1 results in the average intensity squared. In case of an infinite scattering volume the integration in Eq. (2.10) is extended till infinity and the correlator $\langle \rho(\mathbf{r}_1, 0) \rho(\mathbf{r}_3, t) \rangle$ in I_2 depends only on the vector difference $\mathbf{r}_1 - \mathbf{r}_3$. As a consequence this term in Eq. (2.16) contributes to the scattering at a zero angle only, and is usually omitted. The remaining term I_3 is equal to the squared modulus of $g_1(t)$. As a result Eq. (2.10) transforms
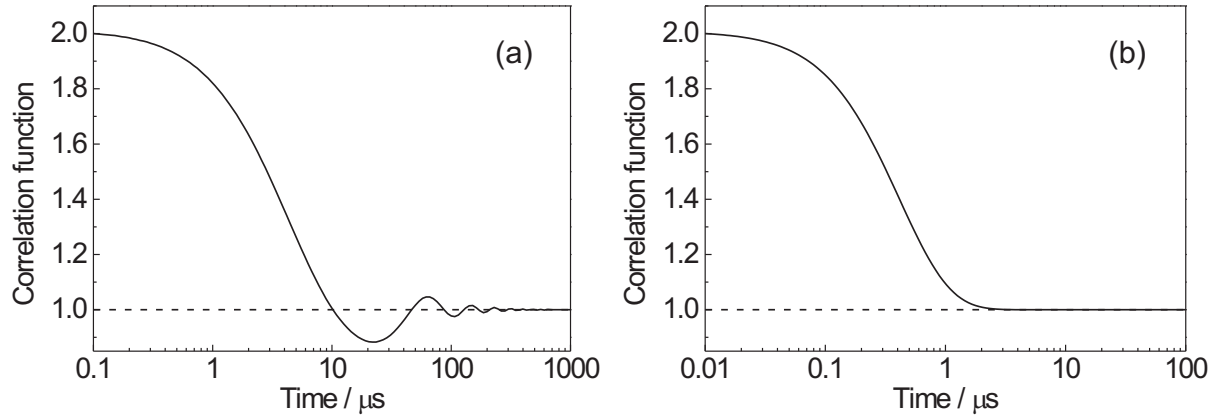
Figure 2.2: Intensity correlation functions calculated for a 2 μm thick membrane: (a) hetorodyne case; (b) homodyne case. The graphs are renormalized for clarity.

into the following equation, known as the Siegert relation:

$$g_2(t) = 1 + |g_1(t)|^2. \tag{2.17}$$

Note that the validity of this relation depends critically on the neglect of the term I_2. The consequences of inclusion of I_2 are considered in Sec. 2.1.3.

Figure 2.2a shows the example of a correlation function in the heterodyne detection scheme. According to Eq. (2.14), in this case $g_1(t)$ defines the profile of the measured intensity correlation function. Such oscillating profiles have been frequently observed in XPCS measurements at specular positions where the reference intensity I_0 is present [58]. In contrast at off-specular positions this signal is absent: homodyne regime. XPCS measurements in this situation indicate a simple exponential relaxation of the intensity correlation function that can be fitted using the Siegert relation [58].

2.1.3   Effects of the finite-size coherence volume

The finite size of the coherence volume can lead to a non-zero contribution of the term I_2 in Eq. (2.16). This has direct consequences for the validity of the Siegert relation. Let us denote the lateral size of the coherence volume as $2R$. Introducing Eq. (2.4) into the correlator of I_2, we can calculate the corresponding contribution to Eq. (2.9). We shall use the new variables $\xi = \mathbf{r}_{1,xy} + \mathbf{r}_{3,xy}$ and $\eta = (\mathbf{r}_{1,xy} - \mathbf{r}_{3,xy})/2$. Introducing integration limits corresponding to the finite size and using that I_2 is a product of complex conjugate numbers, we obtain the following result:
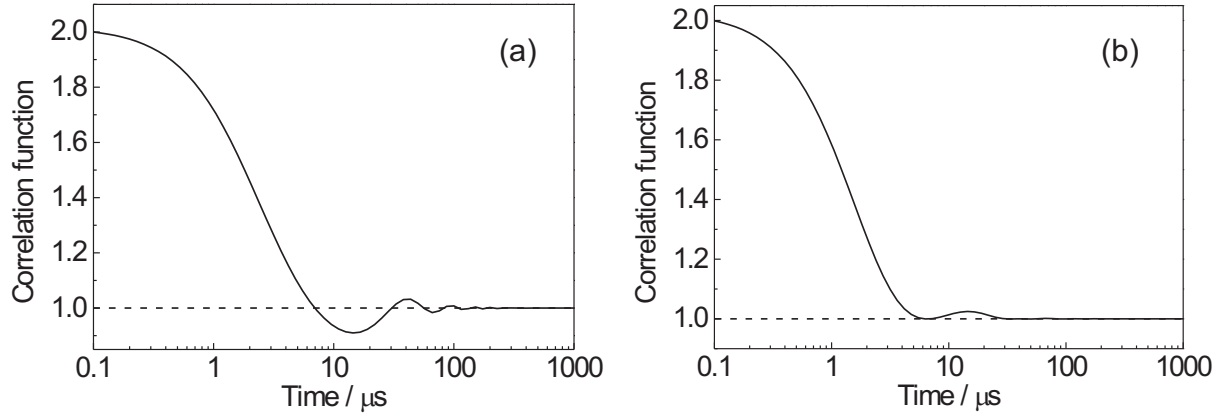
Figure 2.3: Calculation of $g_2(t)$ for a 100 layer membrane: (a) without the term I_2; (b) including I_2. The graphs are renormalized for clarity.

$$I_2 = \iiiint d\mathbf{r}_1 d\mathbf{r}_3 d\mathbf{r}_2 d\mathbf{r}_4 e^{-i\mathbf{q}(\mathbf{r}_1+\mathbf{r}_3)} e^{i\mathbf{q}(\mathbf{r}_2+\mathbf{r}_4)} \langle \Delta\rho(\mathbf{r}_1,0)\Delta\rho(\mathbf{r}_3,t)\rangle \langle \Delta\rho(\mathbf{r}_2,0)\Delta\rho(\mathbf{r}_4,t)\rangle$$

$$= \left| \int_{-R}^{R} d\eta \int dz_1 dz_3 e^{-iq_z(z_1+z_3)} \langle \Delta\rho(\eta,z_1,0)\Delta\rho(-\eta,z_2,t)\rangle \int_{-2(R-\eta)}^{2(R-\eta)} d\xi e^{-i\mathbf{q}_{xy}\xi} \right|^2$$

$$= |\widetilde{\rho}_{layer}(q_z)|^2 \left| 4\int_0^R d\eta \sum_{m,n=1}^N \exp\{-i(m+n)d\} \langle e^{-iq_z(u(-\eta,0)+u(\eta,t))}\rangle \frac{\sin(2q_{xy}(R-\eta))}{q_{xy}R} R \right|^2 . \quad (2.18)$$

For integration limits at infinity, this term would contribute a δ-function to the scattering on the specular ridge ($\mathbf{q}_{xy} = 0$). For a finite-resolution setup, the δ-function contribution smears out and transforms into a $\sin(x)/x$-type function with a finite width in $\mathbf{q}_{xy}$-space still centered at $\mathbf{q}_{xy} = 0$. Defining $g_+(\eta,t) = \langle(u(-\eta,0)+u(\eta,t))^2\rangle$ and using $\langle\exp(ix)\rangle = \exp(-\langle x^2\rangle/2)$ we can rewrite I_2 in the following form:

$$I_2 = |\widetilde{\rho}_{layer}(q_z)|^2 \left| 4\int_0^R d\eta \exp\left(-\frac{q_z^2}{2}g_+(\eta,t)\right) \frac{\sin(2q_{xy}(R-\eta))}{q_{xy}R} R \right|^2 . \quad (2.19)$$

In a similar way we can derive an expression for I_3. Defining new variable now as $\xi = \mathbf{r}_{1,xy} + \mathbf{r}_{4,xy}$, $\eta = (\mathbf{r}_{1,xy} - \mathbf{r}_{4,xy})/2$ and writing $g_-(\eta,t) = \langle(u(-\eta,0)-u(\eta,t))^2\rangle$ we obtain:

$$I_3 = |\widetilde{\rho}_{layer}(q_z)|^2 \left| 4\int_0^R d\eta \exp\left(-\frac{q_z^2}{2}g_-(\eta,t)\right) \cos(q_{xy}R)(R-\eta) \right|^2 . \quad (2.20)$$

Using Eqs. (2.19) and (2.20) we can finally write $g_2(t)$ as

$$g_2(t) = 1 + \cfrac{1}{\left| \displaystyle\int_0^R d\eta \exp\left(-\frac{q_z^2}{2}g_-(\eta,0)\right)\cos(q_{xy}R)(R-\eta)\right|^2}$$

$$\left(\left| \displaystyle\int_0^R d\eta \exp\left(-\frac{q_z^2}{2}g_+(\eta,t)\right)\frac{\sin(2q_{xy}(R-\eta))}{q_{xy}R}R\right|^2 + \right.$$

$$\left.\left| \displaystyle\int_0^R d\eta \exp\left(-\frac{q_z^2}{2}g_-(\eta,t)\right)\cos(q_{xy}R)(R-\eta)\right|^2\right). \tag{2.21}$$

Figure 2.3 shows the effect of the contribution of I_2 to the calculation of the intensity correlation function for finite sizes. The curve in Fig. 2.3b indicates that the presence of I_2 shifts all oscillations above the baseline, creating a profile that cannot be obtained on the basis of the Siegert relation. Such oscillations have been observed in homodyne light scattering experiments of smectic membranes [64], which suggests that the term I_2 can be important for a correct treatment of scattering data in this regime.

2.1.4   Coherence and resolution in XPCS

The wave field $E(t)$ scattered from a particular coherence volume interferes with itself but not with the field originating from neighboring volume elements. As a result we can represent the scattering intensity as a sum of intensities scattered by each coherence region. Each component is related to the structure within the coherence volume and if this structure is changing in time the scattered intensity will also exhibit a time dependence. On the basis of this approach we can express the scattered intensity and the intensity correlator of Eq. (2.7) as:

$$\langle I(t)\rangle = \sum_{i=1}^M \langle I_i(t)\rangle,$$

$$\langle I(\tau)I(\tau+t)\rangle = \left\langle \sum_{i,j=1}^M I_i(\tau)I_j(\tau+t)\right\rangle = \sum_{i=1}^M \langle I_i(\tau)I_i(\tau+t)\rangle + \sum_{i=1}^M \langle I_i(\tau)\rangle \sum_{j=1}^M \langle I_j(\tau)\rangle, \tag{2.22}$$

where M is the number of coherence regions. Furthermore we used the property that the scattered intensities from different coherence volumes are not correlated and $\langle I_i(t)I_j(\tau+t)\rangle = \langle I\rangle^2$ if $i \neq j$. According to Eq. (2.22) both the first, time-dependent term in $\langle I(\tau)I(\tau+t)\rangle$ and $\langle I(t)\rangle$ increase proportionally to the number of coherence volumes in the scattering region. Consequently $g_2(t)$ will decrease if the number of coherence volumes increases. Maximum

performance is achieved for a spatially highly coherent beam in which the coherence and the scattering volume match.

In optical mixing experiments we can distinguish homodyne and heterodyne detection schemes. The homodyne mode works with a superposition of the scattered fields $E(t) = \sum E_s(t)$, while in heterodyne scheme the field $E_s(t)$ scattered by the sample is mixed with the constant reference field E_{ref}. If in the homodyne situation the fields $E_s(t)$ are statistically independent random variables, $E(t)$ will follow a Gaussian distribution that is completely characterized by its first and second moment. This implies that for the homodyne scheme the intensity correlator in $g_2(t)$ − which is a 4-field correlator − is related to the 2-field correlator $g_1(t)$ through Siegert relation Eq. (2.17). It is valid for systems with many independent scatterers or when we have many coherence volumes within a scattering region (although this situation is unfavorable from the experimental point of view; see above). A direct consequence of Eq. (2.17) is that $g_2(t) \geq 1$. When the scatterers become correlated, collective effects come into play and Eq. (2.17) is not longer valid. In the experimental section we shall encounter correlation functions with time intervals where $g_2(t) < 1$.

In the case of heterodyne mixing an additional source is present. This field E_{ref} does not depend on time and can interfere with $E_s(t)$ from the sample: $E(t) = E_{ref} + E_s(t)$. The static reference field can either be external or can come from the sample itself. In Sec. 2.1.2 the field from the equilibrium membrane structure E_0 was considered as a reference signal. If we can separate the scattered intensity from the sample into a time-dependent and a time-independent part, similar arguments as used above can be applied [65]. In photon correlation spectroscopy (PCS) experiments a special grating is often placed in the beam to create a strong secondary source, which increases the sensitivity of the instrument. This can be seen from Eq. (2.14); assuming $|E_{ref}| \gg |E_s(t)|$ we can write

$$\langle I(\tau)I(\tau + t)\rangle \approx I_{ref}^2 + 2I_s I_{ref}\text{Re}[g_1(t)]. \tag{2.23}$$

Compared to the homodyne regime two points are remarkable. First we observe in heterodyne regime $g_1(t)$ and not its squared value. This has a direct implication on the relaxation time observed in the homodyne and heterodyne detection schemes. Particularly, if $g_1(t)$ decays exponentially with the relaxation time τ, than in homodyne experiment based on Eq. (2.17) we would observe the relaxation time $\tau/2$, while in heterodyne mode according to Eq. (2.23) we would detect the time τ [66]. In the Sec. 6.5 we shall use this fact in the interpretation of the experimental data. Second the intensity of the local oscillator amplifies the contribution of the

weakly scattered signal, which makes heterodyne detection the preferred choice in PCS. As we shall see in Sec. 6.5 this increase in intensity does not necessary lead to an increase in contrast of the correlation function.

A rigorous description of the scattering of partially coherent light can be given using the mutual coherence function $\mu(\mathbf{r}_1, \mathbf{r}_2) = \langle E(\mathbf{r}_1, t)E^*(\mathbf{r}_2, t)\rangle$ that can be represented in the following form [67]:

$$\mu(\mathbf{r}_1, \mathbf{r}_2) = \langle E(\mathbf{r}_1, t)E^*(\mathbf{r}_2, t)\rangle = \Psi(\mathbf{r}_1)\Psi(\mathbf{r}_2)g(\mathbf{r}_1 - \mathbf{r}_2)I/A. \tag{2.24}$$

Here A is the scattering area to be integrated over, $\Psi(\mathbf{r})$ is an amplitude factor and $g(\mathbf{r}_1 - \mathbf{r}_2)$ a coherence factor. The latter can be related to the transverse coherence lengths ξ_x and ξ_y according to

$$g(\mathbf{r}_1 - \mathbf{r}_2) = \exp\left(-\frac{(x_1 - x_2)^2}{2\xi_x^2}\right)\exp\left(-\frac{(y_1 - y_2)^2}{2\xi_y^2}\right). \tag{2.25}$$

Using Eq. (2.24) we can write the structure factor $S_t(\mathbf{q})$ at time t in the following form:

$$S_t(\mathbf{q}) = \int d\mathbf{r}_1 d\mathbf{r}_2 e^{-i\mathbf{q}(\mathbf{r}_1 - \mathbf{r}_2)}\Psi(\mathbf{r}_1)\Psi(\mathbf{r}_2)g(\mathbf{r}_1 - \mathbf{r}_2)F(\mathbf{r}_1, \mathbf{r}_2)\langle\rho(\mathbf{r}_1)\rho(\mathbf{r}_2)\rangle, \tag{2.26}$$

where $F(\mathbf{r}_1, \mathbf{r}_2)$ contains the Fresnel phase factors [67]. Note that this is not a time-averaged expression but refers to the scattered intensity $I(t)$ at a particular time t. In order to include the finite resolution of the setup, we must convolute $S_t(\mathbf{q})$ with the resolution function $R(\mathbf{q})$ that defines the range of scattering vectors $(\Delta q_x, \Delta q_y)$ probed at momentum transfer q.

The Fourier transform $\widetilde{R}(\mathbf{r}_1 - \mathbf{r}_2)$ of the resolution function can be expressed in a Gaussian form as [68]

$$\widetilde{R}(\mathbf{r}_1 - \mathbf{r}_2) = \exp\left(-\frac{1}{2}\Delta q_x^2(x_1 - x_2)^2\right)\exp\left(-\frac{1}{2}\Delta q_y^2(y_1 - y_2)^2\right) \tag{2.27}$$

and this form can be incorporated into the expression for $S_t(\mathbf{q})$:

$$S_t(\mathbf{q}) = \int d\mathbf{r}_1 d\mathbf{r}_2 e^{-i\mathbf{q}(\mathbf{r}_1 - \mathbf{r}_2)}\Psi(\mathbf{r}_1)\Psi(\mathbf{r}_2)g(\mathbf{r}_1 - \mathbf{r}_2)\widetilde{R}(\mathbf{r}_1 - \mathbf{r}_2)F(\mathbf{r}_1, \mathbf{r}_2)\langle\rho(\mathbf{r}_1)\rho(\mathbf{r}_2)\rangle. \tag{2.28}$$

The coherence volume is defined through $g(\mathbf{r}_1 - \mathbf{r}_2)$ and $\widetilde{R}(\mathbf{r}_1 - \mathbf{r}_2)$ by the transverse 'incident' coherence lengths ξ_x and ξ_y. Note that the coherence of the radiation at some point $\mathbf{r}$ is defined by the whole optical system [69]. Eqs. (2.25), (2.27) and (2.28) indicate that the coherence properties of the incident beam and the resolution of the setup have a similar influence on the scattering function. Hence we can combine in an heuristic way $g(\mathbf{r}_1 - \mathbf{r}_2)$ and $\widetilde{R}(\mathbf{r}_1 - \mathbf{r}_2)$ into

an 'effective' resolution of the setup given by

$$\Delta'q_x^2 = \Delta q_x^2 + 1/\xi_x^2,$$
$$\Delta'q_y^2 = \Delta q_y^2 + 1/\xi_y^2. \tag{2.29}$$

In Sec. 6.2 we present experiments displaying the effects of resolution changes and modifications of the coherence volume on the XPCS data.

2.2 Neutron spin echo

The main idea of neutron spin echo measurements is to detect changes in the energy of a neutron by using the Larmor precession as 'stopwatch' with the spin of neutron acting as 'pointer'. Changes in the energy of the neutrons influence the angular speed of the spin rotation and consequently lead to differences in the rotation angle, which can be detected and analyzed. Figure 2.4 illustrates the principle of the neutron spin echo technique [70, 71]. The incoming
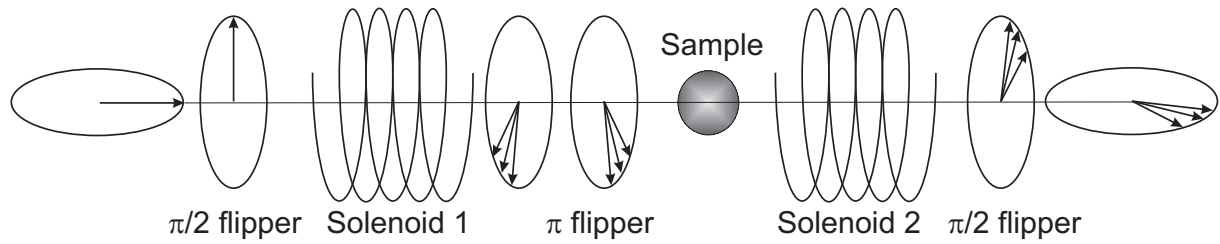

Figure 2.4: Principle of NSE spectromety.

quasi-monochromatic beam of neutrons with their spins polarized along the flight path passes through a $\pi/2$ flipper coil. Subsequently, upon passing through the first solenoid the spins will rotate due to Larmor precession. The rotation angle ϕ depends on the time a neutron spends flying through the coil and can be expressed as:

$$\phi = \frac{\gamma H l}{v}, \tag{2.30}$$

where $\gamma = 2.916$ kHz/Oe is the Larmor constant, H is the strength of magnetic field and l is the length of solenoid 1. This leads to a spread in the angle θ of various neutrons, in dependence of their original velocity v. At the end of solenoid 1 the neutron beam passes through a π-flipper. Consequently, at solenoid 2 the spin will rotate in the opposite direction over an angle ϕ':

$$\phi' = \frac{\gamma H'l'}{v}. \tag{2.31}$$

After another $\pi/2$ flip, at the end of the instrument the spins are rotated by an angle $\phi - \phi'$ relative to their initial orientation. If no sample is present the velocity of the neutrons in the first and the second coils are equal and the initial orientation of the spins will be restored if $Hl = H'l'$. This situation is achieved after the tuning process of the NSE spectrometer.

In presence of a sample the scattering process results in a change of the neutron energy, thus changing the velocity:

$$\hbar\omega = \frac{mv'^2}{2} - \frac{mv^2}{2} \tag{2.32}$$

From this energy change we can calculate the difference $\phi - \phi'$ as:

$$\phi - \phi' = \gamma Hl\left(\frac{1}{v} - \frac{1}{v'}\right) \approx \frac{\gamma Hl}{2v^3}(v'^2 - v^2) = \frac{\gamma Hl}{mv^3}\hbar\omega. \tag{2.33}$$

Once the neutrons pass the second $\pi/2$-flipper the projection of the resulting spin on the initial polarization direction (say x) is analyzed. this projection can be represented as:

$$S_x = \langle\cos(\phi - \phi')\rangle = \left\langle \cos\left(\frac{\gamma Hl}{mv^3}\hbar\omega\right)\right\rangle. \tag{2.34}$$

The probability of recording a neutron with scattering vector $\mathbf{q}$ and energy change $\hbar\omega$ is given by the dynamic structure factor $S(\mathbf{q},\omega)$. The scattering vector $\mathbf{q}$ is defined by the scattering geometry. Introducing the notation

$$t_{NSE} = \frac{\gamma Hl\hbar}{mv^3} = \frac{\gamma Hlm^2}{2\pi h^2}\lambda^3, \tag{2.35}$$

we can calculate the average as:

$$S_x = \frac{\displaystyle\int S(\mathbf{q},\omega)\cos(\omega t_{NSE})d\omega}{\displaystyle\int S(\mathbf{q},\omega)d\omega}. \tag{2.36}$$

The denominator of this equation has the form of a Fourier transform, which is an intermediate scattering function $I(\mathbf{q},t)$. The average spin projection can be represented in terms of $I(\mathbf{q}, t_{NSE})$ as:

$$S_x = \frac{\mathrm{Re}I(\mathbf{q}, t_{NSE})}{I(\mathbf{q}, 0)}. \tag{2.37}$$

As the 'effective' time parameter t_{NSE} is determined by the magnetic field, $I(\mathbf{q}, t)$ can be measured by varying H. Figure 2.5 illustrates the signal measured in the NSE experiments. It is recorded by changing current in the few extra turns wound at the end of the solenoid 2. This
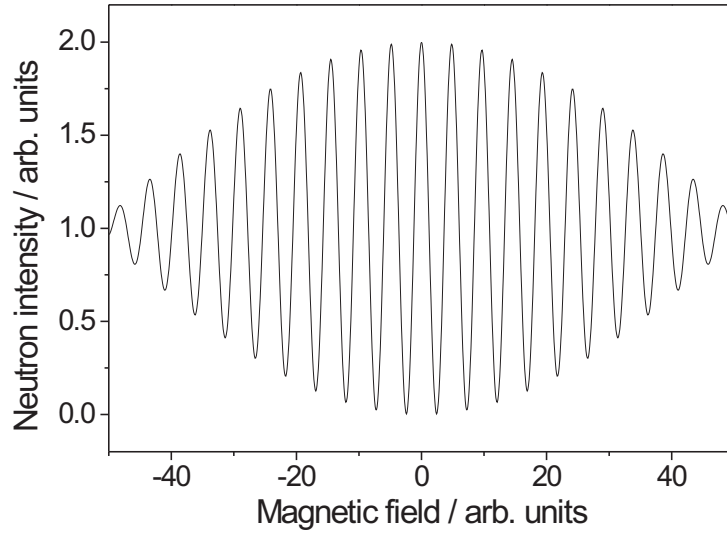
Figure 2.5: Neutron spin echo from a polychromatic neutron beam.

leads to extra spin rotations resulting in the observation of an oscillating profile at the detector, referred as a spin echo. The width of the "wave packet" in Fig. 2.5 is related to the monochromaticity of the beam. The amplitude of this echo is equal to the spin projection S_x, which defines the value of $I(\mathbf{q}, t_{NSE})$ for the corresponding magnetic field H. Varying H and extracting from the echo signals the values of S_x we can retrieve the intermediate scattering function $I(\mathbf{q}, t)$.

From Eq. (2.35) we see that $t_{NSE} \sim \lambda^3$: the most effective way of extending the accessible time range is to use neutrons with larger wavelengths. On the other hand, an increase of λ reduces the accessible range of the scattering vectors $\mathbf{q}$ because the corresponding scattering angles become larger and are limited by the instrument. The polarization of the neutrons results in a significant loss of neutron flux. Combined with monochromatization of the beam this would make NSE almost unusable. Fortunately, the measurements can be performed using quasi-monochromatic neutron beam.

Chapter 3

Experimental

In this chapter we introduce the smectic liquid crystal samples used in the experiments. We discuss the sample preparation procedure, including the sample frames, the two-stage oven and the optical reflectometer setup. Next, we consider the configuration of beamline ID10A at the European Synchrotron Radiation Facility (ESRF, Grenoble), where the x-ray photon correlation spectroscopy (XPCS) measurements were performed, and the scattering geometry used. Then the effect of the strong x-ray beam on the stability of the smectic membranes is described. In the last part we discuss the neutron spin echo (NSE) setup at beamline IN15 at the Institut Laue-Langevin (ILL, Grenoble).

3.1   Preparation of smectic membranes

We studied the smectic liquid crystalline compounds N-(4-*n*-butoxybenzilidene)-4-*n*-octylaniline (4O.8), 4-heptyl-2-[4-(2-perfluorhexylethyl)phenyl]-pyrimidin (FPP) and 4-octyl-4′-cyanobiphenyl (8CB). Their molecular structure and phase transitions have been given in Fig. 1.1. The experiments were done at lower end of the SmA temperature region, around 50, 100 and 27°C for 4O.8, FPP and 8CB, respectively. In Table 3.1 we summarize values of the relevant material parameters of these compounds.

For the XPCS measurements a rectangular stainless-steel frame with sharp edges and a variable area was employed, in which two blades could be moved by a micrometer screw (see Fig. 3.1). Starting with smectic material at (almost) closed blades, membranes up to tens of μm thick and $5-10$ mm long were stretched using 15 mm and 25 mm wide frames. For x-ray reflectivity studies a large footprint of the incident x-ray beam must be accommodated.

Table 3.1: Material parameters of the compounds investigated (after [8]).

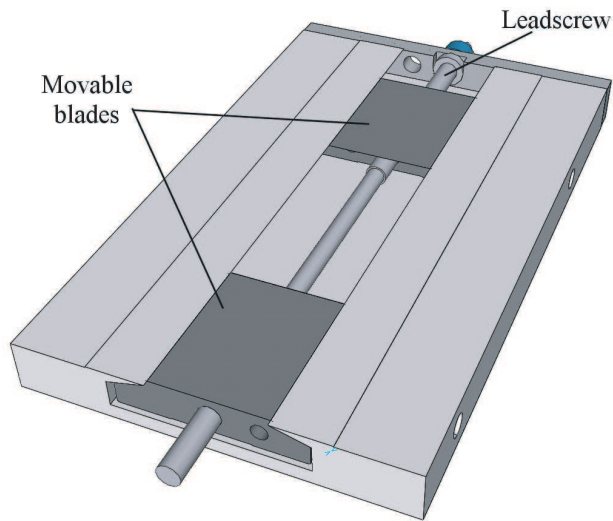| Parameter	4O.8	FPP	8CB
$\gamma/(10^{-3}\ \mathrm{N/m})$	21	13	25
$\eta_3/(\mathrm{kg\ m^{-1}s^{-1}})$	0.05	0.015	0.1
$K/(10^{-12}\ \mathrm{N})$	5	10	20
$B/(10^7\ \mathrm{N/m^2})$	0.10	75	1.8

Figure 3.1: Stainless steel frame used for preparing smectic membranes.

The sharp blades forced the membrane close to the top of the holder, reducing shadowing of the beam. The samples were placed inside a two-stage oven with thin kapton windows (see Fig. 3.2) [23, 72]. The oven was pumped down to 10^3 Pa to prevent parasitic x-ray scattering from air and sample degradation due to the possible oxidation.

For NSE measurements, in order to accommodate the large neutron beam, large-size membranes of 50×50 mm^2 were stretched on an aluminum frame. The frame was mounted inside the supporting aluminum stage. NSE measurements were done at the room temperatureusing 8CB only. These large-size membranes were not of uniform thickness; instead, several different regions were observed with a thickness from about half a micron at the top of the frame up to a few microns at the bottom. In order to gain contrast in the neutron scattering, we used 8CB with deuterated phenyl rings [73].

To prepare appropriate thick membranes, the stretching frame is put inside the open inner oven and placed in a large preparation oven. The latter oven allows manipulation of the sam-
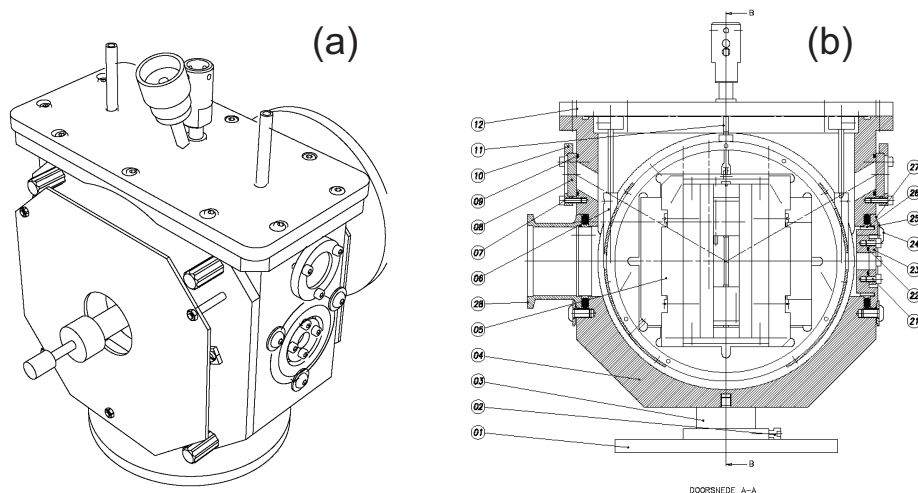
Figure 3.2: Two-stage oven used in XPCS measurements. (a) Side view. (b) Movable frame mounted inside the oven.

ple via flexible gloves in the window of the door. The temperature of the preparation oven is set to about $2-3°$C below the upper limit of the existence range of the smectic phase for the particular compound. Initially the blades of the frame are almost closed, but not fully to prevent damaging the sharp edges. A smectic droplet is spread over the remaining gap; subsequently the blades are opened by steps of a few hundred microns. Between each step the membrane is allowed to equilibrate for $5-10$ minutes. During this process defects arise on the surface of the membrane. The further evolution of these defects depends strongly on the preparation temperature. If the temperature is too low, the defects persist due to the high viscosity of the liquid crystal. If the temperature is too high, thinner areas can appear spontaneously and lead to thinning of the membrane. Only in the proper temperature regime relatively thick membranes up to about 10 μm can be made. Sharp blades are essential to obtain uniform samples and thus maximize the scattering intensity, but at the same time seem to limit the thickness that can be reached. Directly after preparation, a film usually consists of regions of different thickness, from which it equilibrates to a uniform thickness. The equilibration time varies from minutes to days depending on the specific compound, the temperature, and the type of frame. Usually the thinnest region grows at the expense of the thicker ones. The two surfaces of a membrane induce an almost perfect alignment of the smectic layers: the residual curvature of the film is mainly due to the non-planarity of the edges of the holder. The resulting mosaic distribution, expressed as the angular spread of the surface normal, can be $\lesssim 0.001°$ over an area of about $100 \times 500\ \mu$m^2 (footprint at high resolution) [74]. After completion of the stretching process the

membrane is cooled down to the measurement temperature. Subsequently the inner oven is closed, transported to the x-ray setup and placed in the pre-heated outer oven.
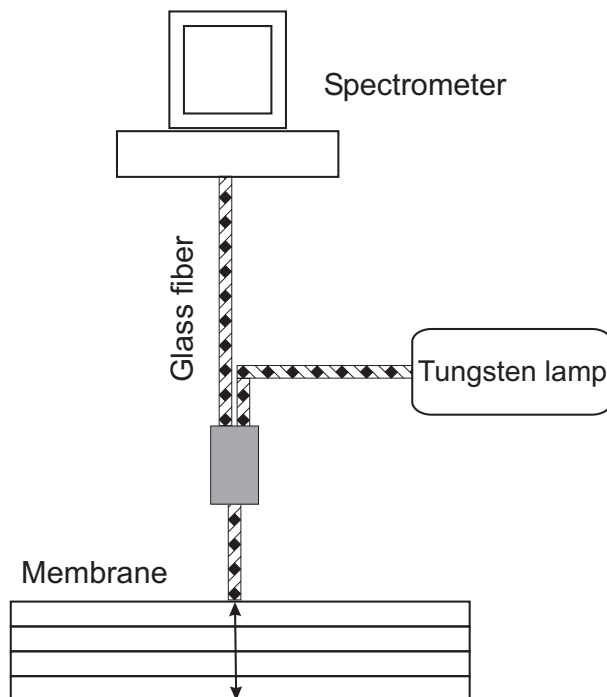

Figure 3.3: Scheme of optical reflectometer setup.
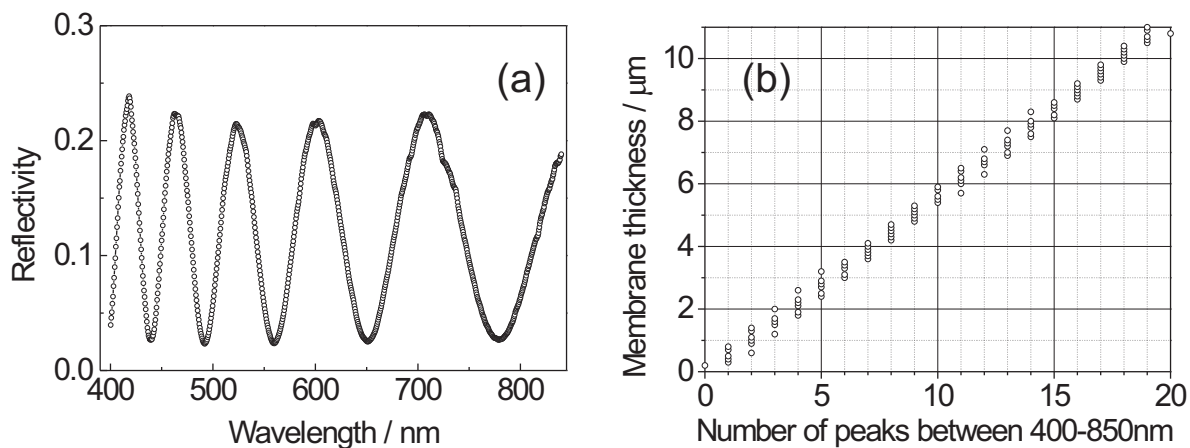
Figure 3.4: Optical reflectivity. (a) Example of the optical reflectivity curve from the smectic membrane. (b) The dependence of membrane thickness on the number of observed interference maximas.

The membrane thickness was monitored by optical reflectivity during both the preparation stage and the experiments (see Fig. 3.3) [7, 72, 75, 76]. An optical fiber was mounted perpendicular to the surface of the membrane. Polychromatic light from a tungsten lamp was guided through the fiber. The light reflected from the membrane was fed into a spectrometer. Due to the interference of the light scattered from the top and the bottom surfaces of the membrane, a

wavelength dependence in the reflected intensity is obtained:

$$I(\lambda) = \frac{f \sin^2\left(\dfrac{2\pi n_\parallel L}{\lambda}\right)}{1 + \sin^2\left(\dfrac{2\pi n_\parallel L}{\lambda}\right)}, \tag{3.1}$$

where $n_\parallel$ is the refractive index, L is the thickness of the membrane, λ is the wavelength of the radiation and f is related to the refractive index $n_\parallel$. L and f were used as parameters for fitting the experimental spectra. The spectra were measured in the interval $400 < \lambda < 800$ nm. As the refractive index depends on the wavelength, the average value of $n_\parallel = 1.5$ was used in fittings in this spectral range. Figure 3.4a shows an example of the data collected in this way. Oscillations observed in this graph correspond to different interference orders. The number of maxima observed in the figure is a good reference for a quick estimation of the membrane thickness. Figure 3.4b shows the dependence of the membrane thickness on the number of observed interference maxima.

For the membrane thicknesses up to few hundred layers the number of smectic layers can be precisely determined from specular x-ray reflectivity. Reflection occurs both at the front and the back interface, leading to constructive or destructive interference as a function of the incoming angle (Kiessig or interference fringes, see Sec. 1.3). As indicated by Eq. (1.12), the period of the fringes is inversely proportional to the number of smectic layers N, which can be determined unambiguously.

3.2 X-ray photon correlation spectroscopy measurements

XPCS experiments have been performed at the undulator beamline ID10A (Troïka I) of the European Synchrotron Radiation Facility (ESRF, Grenoble) (Fig. 3.5). The x-ray radiation arises from three undulators placed in series in the storage ring, giving an effective source with full-width-at-half-maximum (FWHM) dimensions of 928×23 μm^2 (H$\times$V). The measurements have been carried out in the uniform filling mode of the storage ring (992 bunches at intervals of 2.8 ns). Fig. 3.6 gives the scattering geometry. Preliminary collimation is done by Slit 1 and Slit 2 set to 300×300 μm^2 and 200×200 μm^2, respectively. A single-bounce Si(111) monochromator (Mono 2) operating in a horizontal scattering geometry selects energies of 8 or 13.4 keV, leading to a wavelength λ of 0.155 or 0.925 nm, respectively. Subsequently, the beam is reflected by a Si mirror to suppress higher order light. The choice of the energy has a major influence on the stability of the samples [77] and will be discussed later. The sample position is at a distance

of 45 m from the source. The transverse coherence length (see Eq. (1.14)) is $\lesssim 10 \ \mu$m in the horizontal direction (ξ_{H}) and $\gtrsim 100 \ \mu$m in the vertical direction (ξ_{V}). A compound refractive beryllium lens is used to increase the incident intensity by focusing the beam in the vertical direction. Focusing reduces ξ_{V}, matching it to the coherence length ξ_{H} in the horizontal direction. The bandpass of the monochromator Mono 2, given by $\Delta\lambda/\lambda \approx 10^{-4}$, determined the longitudinal coherence length ξ_l of about 1.5 μm. The maximum path length difference of the beam in a smectic membrane of the thickness L is given by $2L\sin\theta$ and should not exceed the value of ξ_l. At the quasi-Bragg position ($\theta \simeq 1.5°$) this means that L should not be larger than about 30 μm.

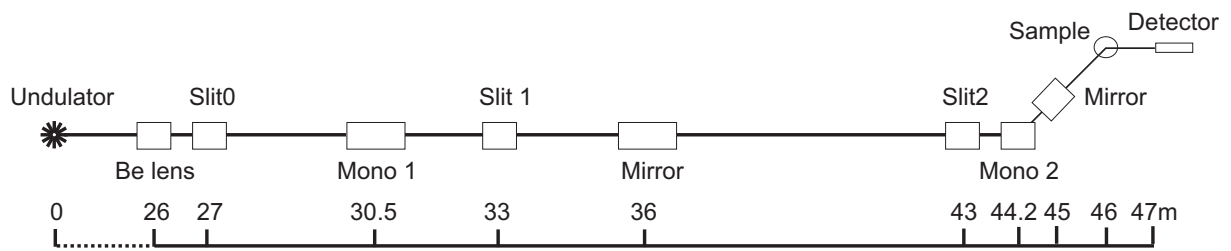*Figure 3.5: Scheme of the XPCS setup at beamline ID10A of the ESRF.*

We used 10 μm and 100 μm pinholes in front of the sample to select the spatially coherent part of the beam. The incident beam on the sample was observed to be structured. These distortions are attributed to speckles occurring from imperfections in the windows and other optical elements in the beam path, and cause some uncertainty in the spatial coherence lengths of the beam. Guard slits were placed after the pinhole to remove parasitic scattering. The coherent photon flux at the sample was for a 10 μm pinhole about 1×10^9 counts s^{-1}/100 mA at 8 keV and about 3×10^7 counts s^{-1}/100 mA at 13.4 keV.

A fast avalanche photodiode (Perkin Elmer C30703) [78] with an intrinsic time resolution $\lesssim 4$ ns was used as detector at a distance of 1.5 m from the sample, with pre-detector slit gaps varying from 0.01 mm to 0.2 mm. The resolution of the setup was estimated as $\Delta q_x \approx 10^{-4}$ nm^{-1} and $\Delta q_y = \Delta q_z \approx 10^{-3}$ nm^{-1}. The intensity-intensity time auto-correlation function was measured in real time using a hardware multiple-tau digital autocorrelator FLEX01-8D (correlator.com, sampling time down to 8 ns). Thanks to the perfect match between the millidegree mosaicity of the smectic membranes and the high resolution of the setup we could reach count rates in the range of tens of MHz. For one experiment the arrival times of all individual pulses from the detector were stored using a 2 GHz multiscaler board, and the correlation function was calculated later. Fig. 3.7 shows such a direct measurement with 0.5 ns
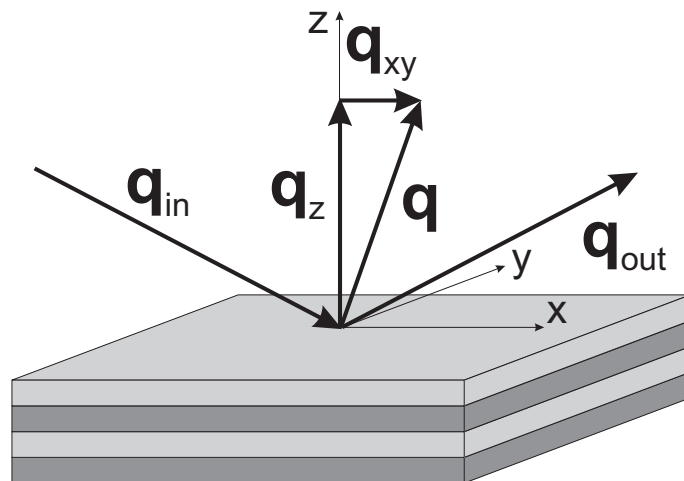
Figure 3.6: Scattering geometry. $\mathbf{q_{in}}$ and $\mathbf{q_{out}}$ represent the incident and scattered wave vector, respectively, and $\mathbf{q}$ is the scattering vector. q_{xy} and q_z are the projections of $\mathbf{q}$ on the surface and on the normal to the surface of the smectic membrane, respectively.

resolution of the bunch-structure of the storage ring. It nicely demonstrates the ultimate time limit of 2.8 ns for XPCS in this situation.
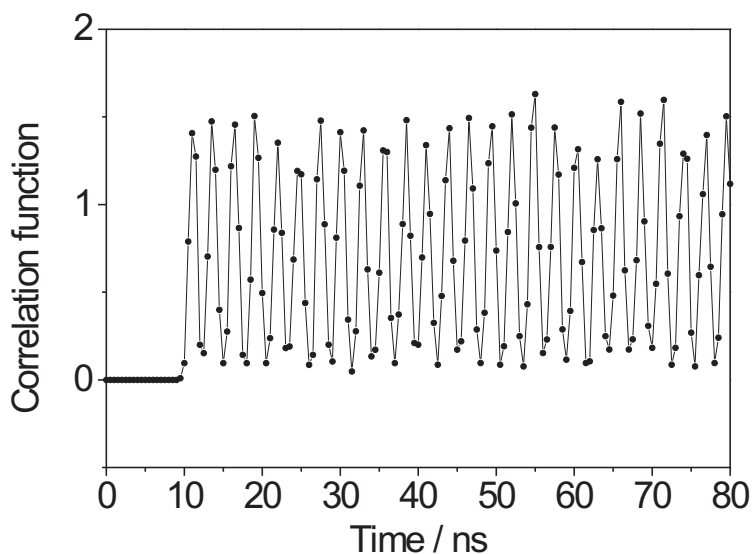
Figure 3.7: Direct measurement of the bunch structure of the ESRF storage ring in the continuous mode.

Initially we worked with the strongest third harmonic of the undulator at 8 keV; in later experiments we switched to the fifth harmonic at 13.4 keV. At this energy the x rays are less absorbed, leading to an improved stability of the smectic membranes. On the other hand, at 13.4 keV the intensity is about 30 times less, mainly because the focussing Be lens is not optimized anymore. This provided no great problem as the intensity at the detector was limited anyhow to about 1 MHz by the hardware correlator. Already for micron thickness membranes

we needed considerable attenuation to bring the intensity down to the working interval. Finally, upon increasing the energy also the transverse coherence length of the x rays drops. Consequently, we expected a decrease in contrast. However, in practice we observed $20-30\%$ contrast, rather similar to the 8 keV case. Evidently the limiting factor for the contrast of the correlation function is in the quality of both the sample and the optical elements in the beamline.

In most cases we worked with vertical membranes for which gravity assists in equilibrating the sample [79]. Consequently the scattering plane was horizontal and the Be lens could be used advantageously to focus in the vertical direction.

3.3 Beam absorption and sample stability

In modern third-generation synchrotrons the high brilliance of the beam can have a destructive effect on many samples, in particular in the case of soft matter. For soft films on a substrate the x-ray beam probably generates free electrons in the substrate; these in turn migrate to the soft film and have a devastating ionizing effect. In the absence of a substrate, smectic membranes show a remarkable resistance to high energy loads. The problems we encountered were not so much associated with irreversible beam damage but rather with heat absorption by the sample. Though in the case of XPCS the pinhole collimation reduces the total intensity strongly, the local flux does not change ($> 10^{13}$ photons s^{-1}mm^{-2} @ Si(111), 8 keV). Hence even the high-resolution setup used in XPCS experiments puts exceptional stability requirements on the sample.

The heat generated by 8 keV x rays in a smectic membrane can be estimated as follows. At the Bragg angle $\theta \simeq 1.5°$ the path length for a membrane of thickness $L = 1.7~\mu$m is given by $L/\sin\theta \simeq 65~\mu$m. The absorption of hydrocarbons over this length is about 2% of the incident intensity of 10^9 photons/s, which amounts to 2×10^7 photons/s. At 8 keV this is equivalent to about 3×10^{-8} W. The width W of the beam and the height H perpendicular to the scattering plane are of the order of 10 μm, the size of the pinhole. Hence the absorption takes place in a volume $V = (L/\sin\theta)WH \simeq 6 \times 10^{-6}$ mm^3. For a density $\rho = 10^3$ kg/m^3 and a specific heat of 2×10^3 J/(kg°C), this leads to an increase of the initial temperature in the illuminated volume of the order of $3°$C/s. At 13.4 keV the absorption is a factor 4 less. The absorption volume is embedded in the membrane and heat is expected to spread out laterally through the film by conduction and convection. It is not easy to estimate these effects, but evidently an appreciable
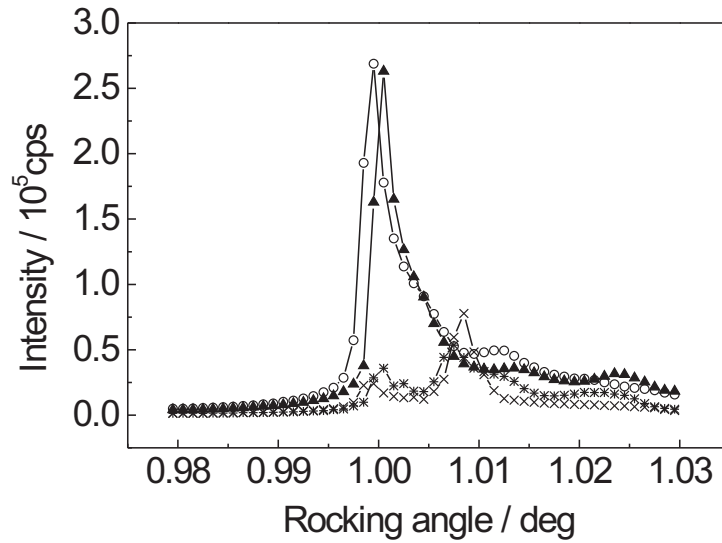
Figure 3.8: Effects of beam absorbtion on the rocking curve of a 1.7 μm FPP membrane (10 μm pinhole). Circles: Initial rocking curve. Crosses: After removal of one attenuator (3× increased intensity). Asterisks: Immediately after inserting the attenuator again. Triangles: After equilibrating for 6 minutes.

temperature increase can occur. Upon approaching the transition to a nematic or an isotropic phase this can lead to spontaneous thinning of the membrane.

The heat generated is sufficient to cause some convective instabilities inside the smectic membrane [80]. This results in fluctuations of the reflected intensity. Figure 3.8 shows changes of the rocking curve induced by removal of an attenuator of 25 μm Cu leading to three times more intensity. This increase of incident intensity results in a decrease (!) of the scattered intensity. After inserting the attenuator back, the original rocking curve profile is restored after a few minutes. We attribute this behavior to hydrodynamic instabilities in the sample arising from convective flow caused by local density changes due to heating. This disturbs the orientation of the layer structure of the membrane leading to a changing rocking curve as shown in Fig. 3.8. Evidently we are working at the limits of stability of the smectic membranes themselves. In the case of a 100 μm pinhole the heat load per unit volume is still the same, but the absolutely absorbed heat is two orders of magnitude larger. Hence variation of the pinhole can cause large changes in sample stability.

3.4   Neutron spin echo measurements

Neutron spin echo measurements were performed at spectrometer IN15 of the Institut Laue-Langevin (ILL, Grenoble, France) [81]. Figure 3.9 shows a schematic view of the NSE spectrom-

eter. The neutron beam of a size of about 40×10 mm^2 (V×H) was used to give approximately square footprint at the first Bragg angle. Neutrons initially pass a velocity selector, which gives about 15% monochromaticity. Wavelengths of 0.9 nm and 1.5 nm were selected, resulting in accessible time scales up to 40 ns and 100 ns, respectively. The neutron beam is polarized through reflection from the first supermirror. The first $\pi/2$-flipper rotates the spins by 90°, so that they precess when they pass through the first solenoid. At the end they pass through the π-flipper which changes their orientation by 180°. After scattering by the sample the neutrons pass the second solenoid and the second $\pi/2$-flipper. The resulting spin orientation is analyzed by reflecting the neutrons from the second supermirror.
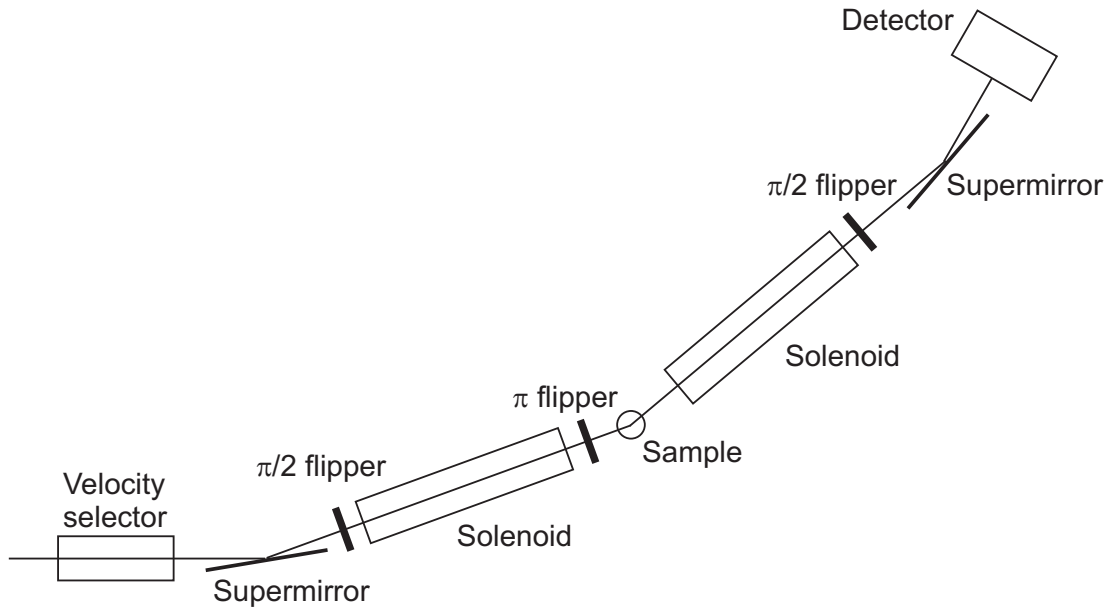
Figure 3.9: Schematic view of the NSE spectrometer.

The reflected neutrons were registered by a 2D position-sensitive detector. Each point of the detector corresponds to a specific value of the projection q_{xy} of the scattering vector on the surface of the membrane (see Fig. 3.10). If $k = 2\pi/\lambda$ is the wave vector of the neutron beam we can write for the beam incident on the membrane

$$q_x = k\cos\left(\frac{\vartheta_0}{2} + \omega\right), \tag{3.2}$$

$$q_y = 0 \tag{3.3}$$

$$q_z = k\sin\left(\frac{\vartheta_0}{2} + \omega\right). \tag{3.4}$$

Figure 3.10: Scattering geometry in neutron spin echo measurements of a smectic membrane in a reflection geometry.

For the outgoing beam we obtain

$$q_x = k \cos(\Delta\phi) \cos\left(\frac{\vartheta_0}{2} + \Delta\psi - \omega\right), \tag{3.5}$$

$$q_y = k \sin(\Delta\phi), \tag{3.6}$$

$$q_z = k \cos(\Delta\phi) \sin\left(\frac{\vartheta_0}{2} + \Delta\psi - \omega\right). \tag{3.7}$$

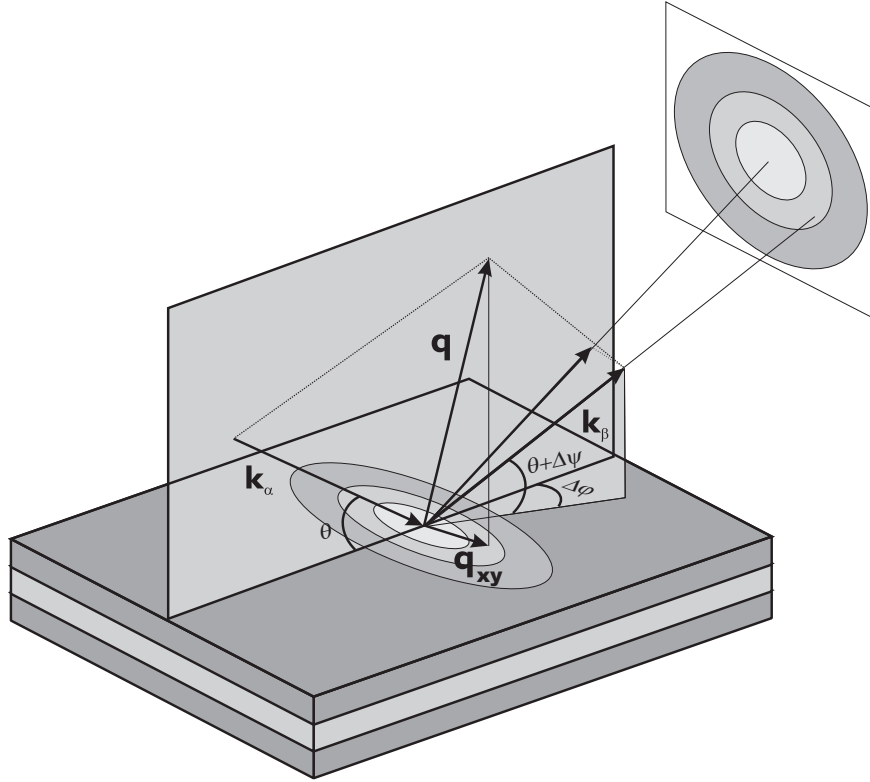Summing up the components in q_x and q_y we arrive at the following expression for q_{xy} which corresponds to a point on the detector at angular displacement (δ, φ):

$$q_{xy} = \frac{2\pi}{\lambda} \sqrt{(\cos(\Delta\varphi) \cos(\theta + \Delta\psi - \omega) - \cos(\theta + \omega))^2 + \sin^2(\Delta\varphi)}. \tag{3.8}$$

To extract the q_{xy}-dependence of the relaxation time we grouped points on the detector with close values of q_{xy}. As the scattering directions with the same projection on the surface of the membrane form a cone, the corresponding points on the detector will form ellipses. Dividing the detector surface into three elliptic areas and integrating the contributions from all points in these regions, we constructed at each scattering angle three correlation functions.

In the NSE measurements, $S(q,t)$ was assumed to behave as a Kohlrausch-Williams-Watts (KWW) function [82, 83]:

$$S(q,t) = \exp\left\{-\left(\frac{t}{\tau_{\mathrm{KWW}}}\right)^{\beta}\right\}. \tag{3.9}$$

This form arises from a broad superposition of exponentials with some distribution function $f(\tau)$ [84]:

$$\int_{-\infty}^{+\infty} f(\ln\tau)\exp\left(-\frac{t}{\tau}\right)d(\ln\tau) = \exp\left\{-\left(\frac{t}{\tau_{\mathrm{KWW}}}\right)^{\beta}\right\}. \tag{3.10}$$

In this case $S(q,t)$ can be written as

$$S(q,t) = \int_{0}^{\infty} d\tau\, f(\tau)\exp\left(-\frac{t}{\tau}\right). \tag{3.11}$$

From this equation, we can define the average value of τ as

$$\langle\tau\rangle = \int_{0}^{\infty} \tau f(\tau)d\tau. \tag{3.12}$$

Now we can calculate the following integral:

$$\int_{0}^{\infty} S(q,t)dt = \int_{0}^{\infty}\int_{0}^{\infty} dt\, d\tau\, f(\tau)\exp\left(-\frac{t}{\tau}\right) = \int_{0}^{\infty} d\tau\, f(\tau)\tau = \langle\tau\rangle. \tag{3.13}$$

On the other hand we can use Eq. (3.11) and calculate the above integral exactly:

$$\int_{0}^{\infty} S(q,t)dt = \frac{\Gamma(1/\beta)}{\beta}\tau_{\mathrm{KWW}}. \tag{3.14}$$

Equating the results of the last two equations we conclude:

$$\langle\tau\rangle = \frac{\Gamma(1/\beta)}{\beta}\tau_{\mathrm{KWW}}. \tag{3.15}$$

Fitting the NSE curves with a KWW exponential function and using Eq. (3.15), we obtained the average value of the relaxation time for each area section of the detector.

Chapter 4

Theory of fluctuations in smectic membranes

In this chapter the theory of fluctuations in smectic membranes is presented, based on the continuum model. Three different types of relaxation behavior are considered: oscillatory relaxation, surface dominated exponential relaxation and bulk-elasticity dominated exponential relaxation. We discuss the transition between these regimes as defined by the specific wave vector of the fluctuation. In addition, the implications of different relaxation profiles on the intermediate scattering function are described.

4.1 Fluctuation spectra

Extensive theoretical models of fluctuations in smectic membranes have been developed in recent years [10, 85–94]. In this section we consider the theory of fluctuations in smectic membranes following the lines of Ref. [90]. These authors applied Fourier transforms both in space and time, solving the equation of motion in $(\mathbf{q}, \omega)$-space. In the following treatment we give somewhat different derivation of their results avoiding switching into ω-space and solving the equation of motion in $(\mathbf{q}, t)$-coordinates. We find such an approach more transparent, as in x-ray photon correlation spectroscopy (XPCS) as well as in neutron spin echo (NSE) experiments the energy of photons is not discriminated and the results are obtained in terms of the time-dependant intermediate scattering function $S(\mathbf{q}, t)$.

Let us consider fluctuations of a rectangular smectic-A membrane of thickness L and lateral sizes (L_x, L_y). The free energy has the form of Eq. (1.4):

$$F = \frac{1}{2} \int d^2 r_{xy} \int_{-L/2}^{L/2} dz \Big\{ B[\nabla_z u(x,y,z)]^2 + K[\nabla_{xy}^2 u(x,y,z)]^2 + $$

$$\gamma \left([\nabla_{xy} u(x,y,z=-L/2)]^2 + [\nabla_{xy} u(x,y,z=L/2)]^2 \right) \Big\} \tag{4.1}$$

This functional form leads to the following equation of motion

$$\rho_0 \frac{\partial^2 u(x,y)}{\partial t^2} = \eta_3 \frac{\partial}{\partial t} \nabla_{xy}^2 u(x,y) + (B\nabla_z^2 - K\Delta_{xy}^2) u(x,y), \tag{4.2}$$

which must be completed with boundary conditions at the surfaces and edges of the membrane:

$$-\frac{\gamma}{B} \nabla_{xy}^2 u(x,y,z=\pm L/2,t) \pm \nabla_z u(x,y,z=\pm L/2,t) = 0, \tag{4.3}$$

$$u(0,y,z,t) = 0, \, u(L_x,y,z,t) = 0,$$
$$u(x,0,z,t) = 0, \, u(x,L_y,z,t) = 0. \tag{4.4}$$

Eq. (4.3) can be obtained by minimizing the free energy F with respect to the surface displacements $u(x,y,z = \pm L/2,t)$ [90]. Because Eq. (4.2) is a fourth-order equation in $r_{xy}(x,y)$, two more boundary conditions are required at the lateral edges. These extra conditions will not have a major influence because the wavelengths of the fluctuations observed are orders of magnitude smaller than the size of the membrane. We have chosen the following two additional conditions, mainly because these are the only ones allowing to solve Eq. (4.2) analytically:

$$u''(0,y,z,t) = 0, \, u''(L_x,y,z,t) = 0,$$
$$u''(x,0,z,t) = 0, \, u''(x,L_y,z,t) = 0. \tag{4.5}$$

To analyze the scattering data the displacement-displacement time correlation function $g(\mathbf{r}_{xy},z,z',t) = \langle [u(0,z',0) - u(\mathbf{r}_{xy},z,t)]^2 \rangle$ must be computed. This correlation function can be expressed in the following form:

$$g(\mathbf{r}_{xy},z,z',t) = G(z,z) + G(z',z') - 2G(\mathbf{r}_{xy},z,z',t), \tag{4.6}$$

$$G(z,z') = \langle u(0,z',0)u(0,z,0)\rangle, \tag{4.7}$$

$$G(\mathbf{r}_{xy},z,z',t) = \langle u(0,z',0)u(\mathbf{r}_{xy},z,t)\rangle. \tag{4.8}$$

In Eq. (4.2) derivatives of $\mathbf{r}_{xy}$ appear only as Laplace operators. Hence, we can expand the solution in a series of eigenfunctions of the Laplace operator that fulfills the boundary conditions Eqs. (4.3) and (4.5):

$$u(x, y, \theta, z, t) = \sum_{m,n=0}^{\infty} A_{mn}(z, t) \sin\left(\frac{\pi m}{L_x}x\right) \sin\left(\frac{\pi n}{L_y}y\right). \tag{4.9}$$

From this equation we obtain the correlation function $G(\mathbf{r}_{xy}, z, z', t)$ in the following form:

$$G(\mathbf{r}_{xy}, z, z', t) = \int_0^{L_x}\int_0^{L_y} dx dy \sum_{m,n}\sum_{k,p} A_{mn}(z, t)A_{kp}(z', t)$$

$$\sin\left(\frac{\pi m}{L_x}x\right)\sin\left(\frac{\pi n}{L_y}y\right)\sin\left(\frac{\pi k}{L_x}(x+x')\right)\sin\left(\frac{\pi p}{L_y}(y+y')\right)$$

$$= \sum_{m,n} G_{mn}(z, z', t)\cos\left(\frac{\pi m}{L_x}x'\right)\cos\left(\frac{\pi n}{L_y}y'\right). \tag{4.10}$$

An equation similar to Eq. (4.2) holds for the corresponding Fourier amplitudes $G_{mn}(z, z', t)$ [90]:

$$\rho_0 \frac{\partial^2 G_{mn}(z, z', t)}{\partial t^2} = -\eta_3 q_{mn}^2 \frac{\partial}{\partial t} G_{mn}(z, z', t) + (B\nabla_z^2 - Kq_{mn}^4)G_{mn}(z, z', t), \tag{4.11}$$

in which

$$q_{mn}^2 = \left(\frac{\pi m}{L_x}\right)^2 + \left(\frac{\pi n}{L_y}\right)^2 \tag{4.12}$$

denotes the wave vector of layer undulations. $G_{mn}(z, z', t)$ fulfils following the following initial and boundary conditions:

$$G_{mn}(z, z', 0) = G_{mn}^0(z, z'). \tag{4.13}$$

$$\frac{\gamma q_{mn}^2}{B} G_{mn}(z = \pm L/2, z', t) \pm \nabla_z G_{mn}(z = \pm L/2, z', t) = 0, \tag{4.14}$$

Here $G_{mn}^0(z, z')$ is the Fourier amplitude of the equilibrium correlation function calculated in Ref. [85] corresponding to the wave vector q_{mn}. In order to solve Eq. (4.11) we separate the variables t and z:

$$\frac{\partial^2 G_{mn}(z, z', 0)}{\partial^2 z} + \frac{\Upsilon}{B} G_{mn}(z, z', 0) = 0, \tag{4.15}$$

$$\rho_0 \frac{\partial^2 G_{mn}(z, z', t)}{\partial t^2} + \eta_3 q_{mn}^2 \frac{\partial}{\partial t} G_{mn}(z, z', t) + (Kq_{mn}^4 + \Upsilon)G_{mn}(z, z', t) = 0, \tag{4.16}$$

where Υ is a constant. The solution can be represented in the form

$$G_{mn}(z, z', t) = A(\Upsilon, t) \sin\left(\sqrt{\frac{\Upsilon}{B}} z\right) + B(\Upsilon, t) \cos\left(\sqrt{\frac{\Upsilon}{B}} z\right). \tag{4.17}$$

In order to fulfil the boundary conditions on the top and the bottom surface of the film we need the roots of the following equations:

$$\cot\left(\lambda_i \frac{L}{2}\right) = -\frac{\gamma q_{mn}^2}{\lambda_i B}, \tag{4.18}$$

$$\tan\left(\mu_i \frac{L}{2}\right) = \frac{\gamma q_{mn}^2}{\mu_i B}. \tag{4.19}$$

From these equations we get an infinite spectrum of solutions $\{\lambda_i, \mu_i\}$ defining layer-compression wave vectors. Now $G_{mn}(z, z', t)$ can be represented in the form:

$$G_{mn}(z, z', t) = \sum_{i=0}^{\infty} A(\lambda_i, t) \sin\left(\lambda_i z\right) + B(\mu_i, t) \cos\left(\mu_i z\right), \tag{4.20}$$

where $A(\lambda_i, t)$ and $B(\mu_i, t)$ are solutions of Eq. (4.16). They can be written as:

$$A(\lambda_i, t) = S_1(\lambda_i) \exp\left(-\frac{t}{\tau_{s,1}}\right) + S_2(\lambda_i) \exp\left(-\frac{t}{\tau_{s,2}}\right), \tag{4.21}$$

$$B(\mu_i, t) = C_1(\mu_i) \exp\left(-\frac{t}{\tau_{c,1}}\right) + C_2(\mu_i) \exp\left(-\frac{t}{\tau_{c,2}}\right). \tag{4.22}$$

Here $\tau_{c,(1,2)}$ and $\tau_{s,(1,2)}$ denote fluctuation relaxation times. Applying the initial conditions we find:

$$A(\lambda_i, t) = \frac{G^s(\lambda_i, z')}{\tau_{s,1} - \tau_{s,2}} \left(\tau_{s,1} \exp\left(-\frac{t}{\tau_{s,1}}\right) - \tau_{s,2} \exp\left(-\frac{t}{\tau_{s,2}}\right)\right), \tag{4.23}$$

$$B(\mu_i, t) = \frac{G^c(\mu_i, z')}{\tau_{c,1} - \tau_{c,2}} \left(\tau_{c,1} \exp\left(-\frac{t}{\tau_{c,1}}\right) - \tau_{c,2} \exp\left(-\frac{t}{\tau_{c,2}}\right)\right), \tag{4.24}$$

where

$$G^s(\lambda_i, z') = \frac{2}{L} \int_{-L/2}^{L/2} G_{mn}^0(z, z') \sin\left(\lambda_i z\right) dz, \tag{4.25}$$

$$G^c(\mu_i, z') = \frac{2}{L} \int_{-L/2}^{L/2} G_{mn}^0(z, z') \cos\left(\mu_i z\right) dz. \tag{4.26}$$

Using the expression for $G^0_{mn}(z, z')$ given in Ref. [85] we can find exact analytical forms for the above integrals:

$$G^s(\lambda_i, z') = \frac{2k_B T}{BL(g^2 + \lambda_i^2)} \left\{ \sin(\lambda_i z') - \frac{\frac{\gamma q_{mn}^2}{B} \sin\left(\frac{\lambda_i L}{2}\right) + \lambda_i \cos\left(\frac{\lambda_i L}{2}\right)}{\frac{\gamma q_{mn}^2}{B} \sinh\left(\frac{gL}{2}\right) + g \cosh\left(\frac{gL}{2}\right)} \sinh(gz') \right\}, \qquad (4.27)$$

$$G^c(\mu_i, z') = \frac{2k_B T}{BL(g^2 + \mu_i^2)} \left\{ \cos(\mu_i z') + \frac{\frac{\gamma q_{mn}^2}{B} \cos\left(\frac{\mu_i L}{2}\right) - \mu_i \sin\left(\frac{\mu_i L}{2}\right)}{\frac{\gamma q_{mn}^2}{B} \cosh\left(\frac{gL}{2}\right) + g \sinh\left(\frac{gL}{2}\right)} \cosh(gz') \right\}, \qquad (4.28)$$

where $g = \sqrt{K/B}q_{mn}^2$. The times $\tau_{s,(1,2)}$ and $\tau_{c,(1,2)}$ depend on the wave vector q_{mn} and the parameters $\{\lambda_i, \mu_i\}$ and can be found from the following relation:

$$\tau_{s,(1,2)}(\lambda_i) = \frac{2\rho}{\eta_3 q_{mn}^2} \left(1 \pm \sqrt{1 - \frac{4\rho}{\eta_3^2 q_{mn}^4}(K q_{mn}^4 + B\lambda_i^2)} \right)^{-1}, \qquad (4.29)$$

$$\tau_{c,(1,2)}(\mu_i) = \frac{2\rho}{\eta_3 q_{mn}^2} \left(1 \pm \sqrt{1 - \frac{4\rho}{\eta_3^2 q_{mn}^4}(K q_{mn}^4 + B\mu_i^2)} \right)^{-1}. \qquad (4.30)$$

Summarizing the above calculations we can write the real-space correlation function in the following form:

$$G(x, y, z, z', t) = \sum_{m,n=1}^{\infty} \cos\left(\frac{\pi m}{L_x} x\right) \cos\left(\frac{\pi n}{L_y} y\right)$$

$$\left\{ \sum_{i=0}^{\infty} \frac{\tau_{c,1} \exp\left(-\frac{t}{\tau_{c,1}}\right) - \tau_{c,2} \exp\left(-\frac{t}{\tau_{c,2}}\right)}{\tau_{c,1} - \tau_{c,2}} G_i^c(\mu_i, z') \cos(\mu_i z) + \right. \qquad (4.31)$$

$$\left. \frac{\tau_{s,1} \exp\left(-\frac{t}{\tau_{s,1}}\right) - \tau_{s,2} \exp\left(-\frac{t}{\tau_{s,2}}\right)}{\tau_{s,1} - \tau_{s,2}} G_i^s(\lambda_i, z') \sin(\lambda_i z) \right\}$$

From Eqs (4.27) and (4.28) we note that $G_i^s(\lambda_i, z')$ and $G_i^c(\mu_i, z')$ decrease for increasing values of the undulation wave vector q_{mn} and the compression wave vectors $\{\lambda_i, \mu_i\}$. This means that Eq. (4.31) is dominated by the fluctuations with the smallest wave vector (largest wavelength). In the further discussion we concentrate on the compression mode with the smallest wave vector given by μ_1. The corresponding relaxation times $\tau_{c,1}$ and $\tau_{c,2}$ further will be referred to as τ_1 and τ_2. Relaxation times corresponding to the higher order modes with larger values of $\{\lambda_i, \mu_i\}$ have been discussed in Refs. [91], but seem to be not accessible experimentally.

Let us consider the high-compressibility limit for which $B \to \infty$. In this approximation we can find analytical solutions for Eqs. (4.18) and (4.19). Approximating the tangent in Eq. (4.19)

by a linear function we obtain μ_1 as:

$$\mu_1 = \sqrt{\frac{2\gamma}{LB}} q_{mn}. \tag{4.32}$$

Using this value for μ_1 we find for $G_1^c(q_{mn}, z')$ the following expression:

$$G_1^c(q_{mn}) = \frac{2k_BT}{KLq_{mn}^4 + 2\gamma q_{mn}^2}. \tag{4.33}$$

Eq. (4.31) now reduces to the form:

$$G(x,y,t) = 2k_BT \sum_{m,n=1}^{\infty} \frac{1}{KLq_{mn}^4 + 2\gamma q_{mn}^2} \cos\left(\frac{\pi m}{L_x}x\right) \cos\left(\frac{\pi n}{L_y}y\right) \frac{\tau_1 \exp\left(-\frac{t}{\tau_1}\right) - \tau_2 \exp\left(-\frac{t}{\tau_2}\right)}{\tau_1 - \tau_2}. \tag{4.34}$$

Introducing μ_1 into Eqs. (4.30) and (4.29) the relaxation times τ_1 and τ_2 are given by

$$\frac{1}{\tau_{1,2}} = \frac{\eta_3 q_{mn}^2}{2\rho_0}\left(1 \mp i\sqrt{\frac{4\rho_0}{\eta_3^2 q_{mn}^4}\left(Kq_{mn}^4 + \frac{2\gamma}{L}q_{mn}^2\right) - 1}\right). \tag{4.35}$$
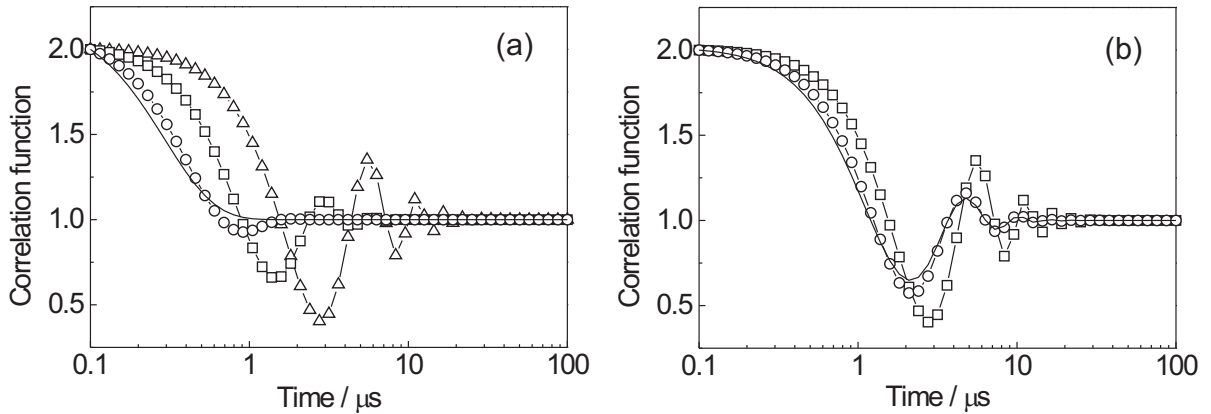

Figure 4.1: Calculated correlation functions for a 10 mm long and a 0.5 μm thick FPP membrane. (a) Single fluctuations with wave vector number m as follows: triangles: 500, squares: 1000, circles: 2000, solid line: 3000. (b) Dependence of the correlation function on the upper limit of the sum in Eq. (4.34) for the lower limit set at 500. Upper limits as follows: squares: 501, circles: 1000, solid line: 2000.

Eq. (4.34) indicates that the layer-displacement correlation function depends on a superposition of contributions of fluctuations with different wave vectors. By changing the limits of the summation we can investigate which wave vectors contribute most to the correlation function. For the sake of simplicity we consider for this exercise a one-dimensional case, omitting

the y-dependence in the correlation function $G(x, y, t)$. Now the summation in Eq. (4.34) is performed over one index only and the wave vector is defined as $q_m = (\pi m / L_x)$. Figure 4.1a shows the result of a series of calculations of the intensity correlation function in which $G(x, t)$ is defined by a single fluctuation. This is achieved by taking only one term in Eq. (4.34) with index m corresponding to the chosen wave vector. We observe that for higher-order fluctuations the generated oscillations are weaker. At a cross-over point $m = 3000$ all oscillations disappear. Figure 4.1b displays the cumulative effect of the fluctuations on the intensity correlation function. Fixing the lower limit of the summation in $G(x, t)$ at $m = 500$ and extending the summation to larger values of m, we see that compared to Fig. 4.1a the oscillations hardly change. This behavior indicates that the resulting correlation function is mainly defined by the first terms in the sum in Eq. (4.34) which correspond to the smallest wave vectors. This argument is used as a basis for the definition of a 'window' of wave vectors dominating the correlation functions in XPCS measurements which is introduced in Sec. 5.2.2.

4.2   Relaxation regimes

According to Eq.(4.35) the relaxation times τ_1 and τ_2 can be given in the following form:

$$\frac{1}{\tau_{1,2}} = a(q_{mn}) \mp i f(q_{mn}), \tag{4.36}$$

where

$$a(q_{mn}) = \frac{\eta_3 q_{mn}^2}{2\rho_0}, \tag{4.37}$$

$$f(q_{mn}) = \frac{\eta_3 q_{mn}^2}{2\rho_0} \sqrt{\frac{4\rho_0}{\eta_3^2 q_{mn}^4} \left(K q_{mn}^4 + \frac{2\gamma}{L} q_{mn}^2 \right) - 1}. \tag{4.38}$$

Figure 4.2 shows the dependence of the real part of the relaxation times τ_1 and τ_2 on the wave vector of a particular fluctuation. The nature of the dispersion curve changes at a cross-over wave vector q_c for which the square-root in Eq. (4.38) changes sign. For the small values q_{mn} involved we can disregard the term $K q_{mn}^4$. Then the relaxation times τ_1 and τ_2 can be represented in the following form:

$$\tau_{1,2} \approx \frac{2\rho_0}{\eta_3 q_{mn}^2} \left(1 \mp i \sqrt{\frac{8\rho_0\gamma}{\eta_3^2 L q_{mn}^2} - 1} \right)^{-1}. \tag{4.39}$$
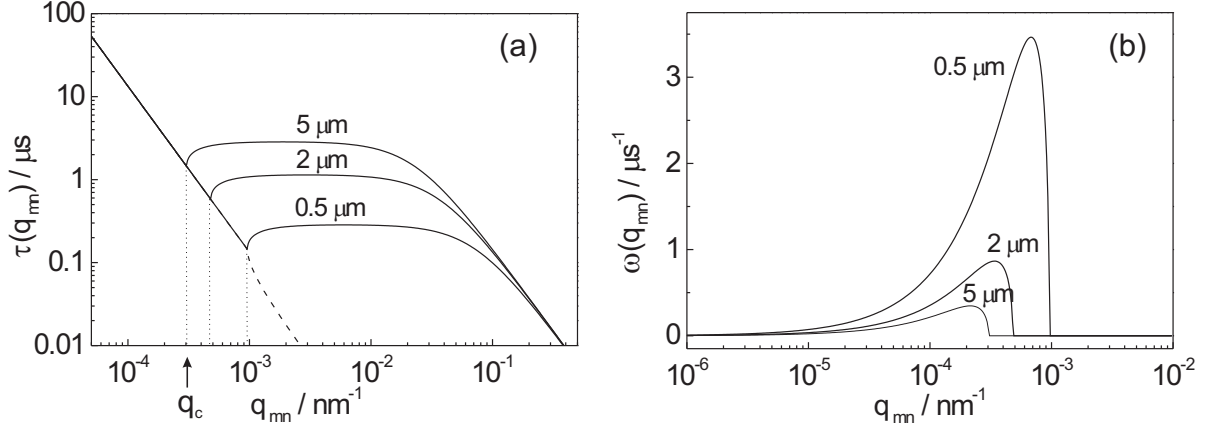
Figure 4.2: Dispersion curves for the relaxation of fluctuations of 8CB membranes for three different thicknesses calculated according to Eq. (4.41) and Eq. (4.42) using the parameters from Table 3.1. (a) Dependence of the relaxation time on the wave vector q_{mn}. The dotted lines indicate for each thickness the transition wave vector q_c; the dashed line give the fast relaxation branch for 0.5 µm. (b) Dependence of the frequency of the fluctuations on the wave vector q_{mn}.

This cross-over is given by:

$$q_c \approx \sqrt{\frac{8\rho_0\gamma}{\eta_3^2 L}}. \tag{4.40}$$

In the region $q_{mn} < q_c$ the function $f(q_{mn})$ is real. This regime corresponds to a combination of exponential relaxation and oscillatory behavior. From Eqs. (4.37) and (4.38) we derive the following expressions for the relaxation time τ and the frequency ω (imaginary part of the relaxation time):

$$\tau(q_{mn}) = \mathrm{Re}\left(\frac{1}{\tau_{1,2}}\right)^{-1} = \frac{2\rho_0}{\eta_3 q_{mn}^2}, \tag{4.41}$$

$$\omega(q_{mn}) = \mathrm{Im}\left(\frac{1}{\tau_{1,2}}\right) = \frac{\eta_3 q_{mn}^2}{2\rho_0}\sqrt{\frac{8\rho_0\gamma}{\eta_3^2 L q_{mn}^2} - 1}. \tag{4.42}$$

Note that the relaxation time does not depend on the membrane thickness while the frequency decreases with thickness as $1/\sqrt{L}$. The behavior of $\tau(q_{mn})$ and $\omega(q_{mn})$ according to Eqs. (4.41) and (4.42) is illustrated in Fig. 4.2 for three membranes of different thicknesses.

In the region $q_{mn} > q_c$ both solutions are real. Figure 4.2 shows that τ_2 strongly decreases with increasing wave vector q_{mn}. The contribution of this fast relaxation to the correlation function is weighted by the value of τ_2 (see Eq. (4.34)) and consequently also decreases strongly with wave vector. Hence we can neglect this branch and consider in the region $q_{mn} > q_c$ only the slow branch with relaxation time τ_1. In this regime the elastic term $K q_{mn}^4$ cannot be disregarded anymore. Using $8\rho_0\gamma/(\eta_3^2 L q_{mn}^2) \ll 1$, for large q_{mn} the square root can be

expanded and we can write τ_1 in the simplified form:

$$\tau_1 = \frac{\eta_3}{2\gamma/L + K q_{mn}^2}. \tag{4.43}$$

According to this equation we can subdivide the region $q_{mn} > q_c$ into two different subregimes. For $K q_{mn}^2 < 2\gamma/L$ we can omit the second term in the denominator of Eq. (4.43) and arrive at

$$\tau_1 = \eta_3 L/(2\gamma). \tag{4.44}$$

In this 'surface relaxation regime' the relaxation time depends only on the surface tension, the membrane thickness and the viscosity. For $K q_{mn}^2 > 2\gamma/L$ the second term in the denominator of Eq. (4.43) dominates and

$$\tau_1 = \eta_3/(K q_{mn}^2). \tag{4.45}$$

In this 'bulk-elasticity dominated relaxation regime' the relaxation time depends on the bending elastic constant K and on the viscosity, but it is neither sensitive to the surface tension nor to the membrane thickness anymore.

Chapter 5

Relaxation in smectic membranes

We present a comprehensive account of the dynamics of layer-displacement fluctuations in smectic liquid-crystal membranes as studied by x-ray photon correlation spectroscopy (XPCS) and neutron spin echo (NSE). Combining these two techniques at fast relaxation times, three distinct relaxation regimes can be distinguished. For thin membranes, at the specular Bragg position oscillatory relaxation occurs, which transforms for thicker samples into exponential decay. At off-specular angles, above a critical angle exponential relaxation is observed in XPCS that does not depend on the scattering angle, indicating relaxation times independent of the wavelength of the fluctuations. The relaxation of the fluctuations in this regime is dominated by the surface tension. Using NSE larger off-specular angles can be reached than for XPCS, for which the relaxation time decreases with the scattering angle. This regime is dominated by the bulk elasticity of the smectic membrane. The results are described using the concept of a detection 'window', which incorporates the effects of the mosaic distribution and of the center of mass movement of the smectic membranes.

5.1   Experimental results

In this chapter we present measurements of the three fluctuation regimes in smectic membranes that were discussed in Sec. 4.2. The results include a transition from oscillatory relaxation of the fluctuations (due to inertial effects) to simple exponential relaxation of overdamped fluctuations, both as a function of membrane thickness and of the off-specular angle. Emphasis is on the factors that influence the dominating wavelength from the fluctuation spectrum. The choice of this quantity is particularly intricate in the limit $q_{xy} \to 0$.
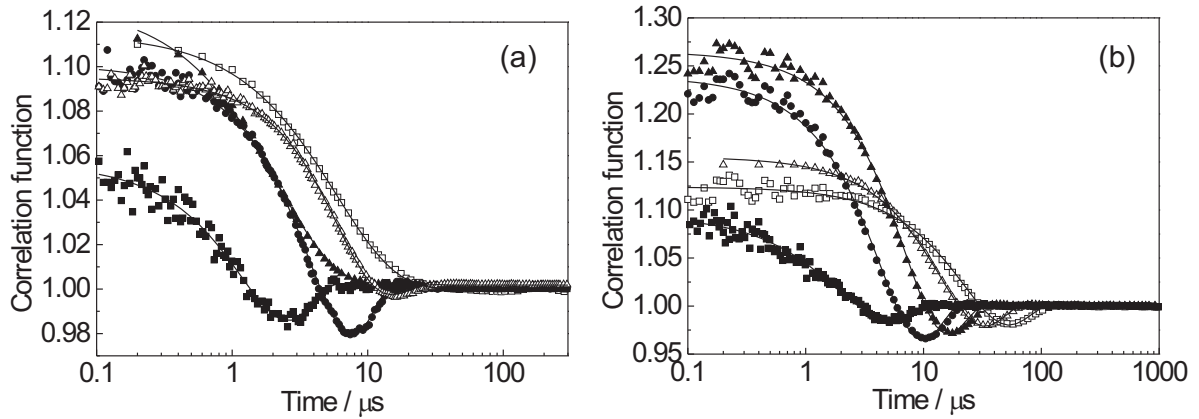
Figure 5.1: Correlation functions from XPCS of smectic membranes of different thicknesses; lines indicate fits to Eq. (5.1). (a) 4O.8; filled squares: 0.45 μm; filled circles: 1.0 μm; filled triangles: 2.2 μm; open triangles: 6.0 μm; open squares: 10.0 μm. (b) FPP; filled squares: 0.48 μm; filled circles: 2.8 μm; filled triangles: 5.9 μm; open triangles: 13.2 μm; open squares: 15.0 μm.

Figure 5.1 shows typical intensity correlation functions from XPCS of smectic 4O.8 and FPP membranes of various thicknesses at the first-order specular Bragg position. The experimental curves were fitted to a simple oscillatory relaxation function:

$$\frac{\langle I(t)I(0)\rangle}{\langle I\rangle^2} = A\exp(-t/\tau)\cos(\omega t + \phi). \tag{5.1}$$

Here A, τ, ω and ϕ are fitting parameters representing contrast, relaxation time, frequency and phase. In thin membranes we note for both compounds a clear oscillatory behavior. In thicker membranes the oscillations shift to larger times, while for thick 4O.8 membranes the oscillations disappear completely and only exponential relaxation is left. In FPP membranes, at the first Bragg position the oscillatory relaxation is present for all thicknesses measured. The only exponential relaxation found in FPP membranes at any specular position was at the second Bragg peak (see Fig. 5.2).

The fitted values for the relaxation time τ and the frequency ω for all samples of different thicknesses measured are given in Tables 5.1 and 5.2, while their thickness dependence is plotted in Fig. 5.3. Even though the scatter of the experimental points is considerable, we can conclude that τ increases and ω decreases with membrane thickness. Note in Table 5.1 the anomalous behavior of a relatively thin 2.2 μm 4O.8 membrane that shows exponential relaxation, while both thinner and thicker membranes still display oscillatory behavior.

Figure 5.4a shows a series of off-specular measurements of 8CB membranes. Already for a small offset from the specular position corresponding to 10 mdeg, the oscillatory profile trans-
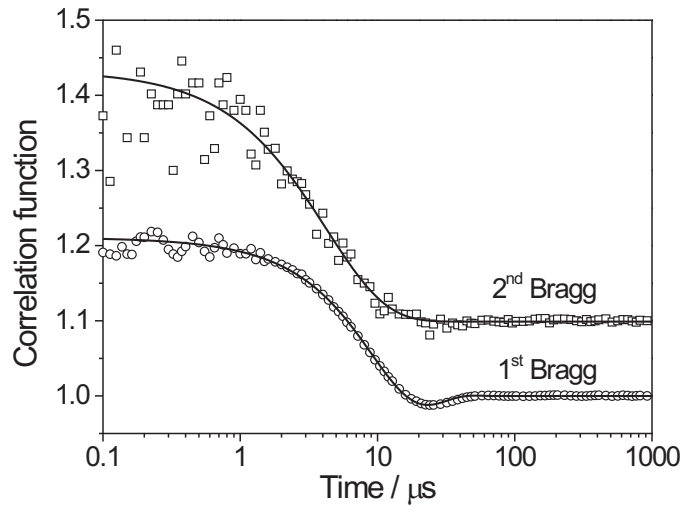
Figure 5.2: Correlation functions measured at the first and second Bragg positions of a 13.2 μm thick FPP membrane.

Table 5.1: Fitting parameters for 4O.8 membranes of different thicknesses (first Bragg peak)

Thickness$/\mu$m	A	τ/μs	ω/μs^{-1}	$\phi/$ rad
0.037	0.06	2.0	0.86	0.40
0.068	0.04	3.9	0.32	0.52
0.3	0.03	5.9	0.29	0.41
1.0	0.10	5.4	0.33	0.08
2.2	0.13	2.2	0	0
5.0	0.05	9.7	0.14	−0.09
6.0	0.11	5.3	0.19	−0.48
10.0	0.11	5.9	0	0

forms into pure exponential relaxation. The relaxation time remains about constant for all measured off-specular positions (see Fig. 5.4b). Figure 5.5 illustrates the transition process from oscillatory to exponential relaxation in more detail for an FPP membrane. Close to the specular Bragg position oscillations are still detected; at slightly larger off-specular scattering angles the behavior changes into exponential relaxation.

On several occasions we obtained for highly ordered membranes a poor contrast for the correlation functions at the specular reflection position. This occurred in spite of the fact that such samples with a narrow mosaic distribution show sharp and very intense specular reflec-

Table 5.2: Fitting parameters for FPP membranes of different thicknesses (first Bragg peak)

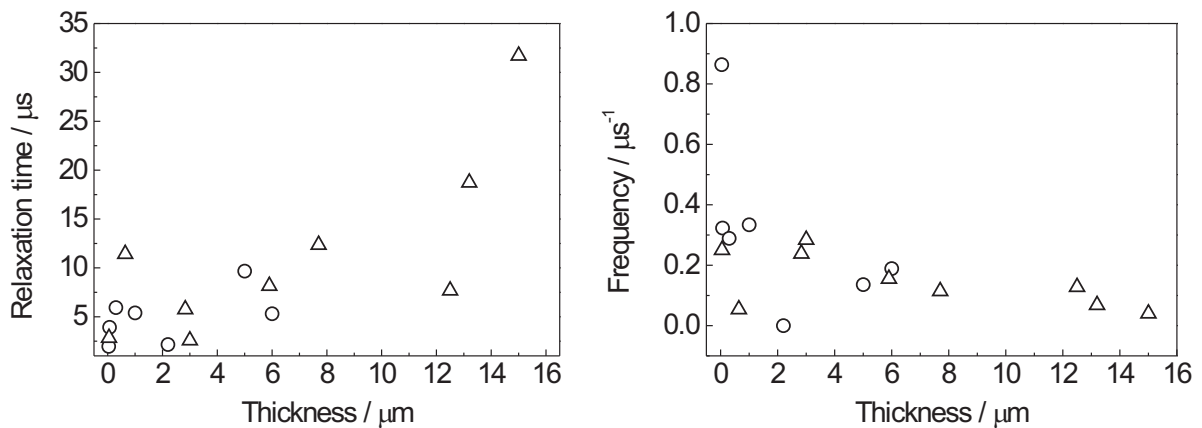| Thickness/μm	A	τ/μs	$\omega/\mu s^{-1}$	$\phi/$ rad
0.047	0.15	2.8	0.25	0.88
0.64	0.15	11.4	0.05	0.95
2.8	0.24	5.8	0.24	0.17
3.0	0.24	2.6	0.28	0.02
5.9	0.27	8.2	0.15	−0.04
7.7	0.21	12.3	0.11	0.13
12.5	0.23	7.7	0.13	−0.49
13.2	0.16	18.7	0.07	0.20
15.0	0.13	31.7	0.04	0.33

Figure 5.3: Dependence of relaxation time and frequency of the oscillations on membranes thickness; circles: 4O.8; triangles: FPP.

tions. This effect is illustrated in Fig. 5.6. At the center of the rocking curve hardly any contrast is left, which starts to develop as soon as we shift slightly (only 0.5 mdeg) off-specular.

Figure 5.7a displays data obtained for 8CB membranes by NSE. At the specular position no relaxation is observed in this time range, below 50 ns, in agreement with the XPCS results of Fig. 5.4a. The curves measured close to the specular position indicate a slow relaxation, while at the larger off-specular positions the relaxation time decreases (see Fig. 5.7b). This behavior differs strongly from the approximately constant values of τ from XPCS at small off-specular angles shown in Fig. 5.4.
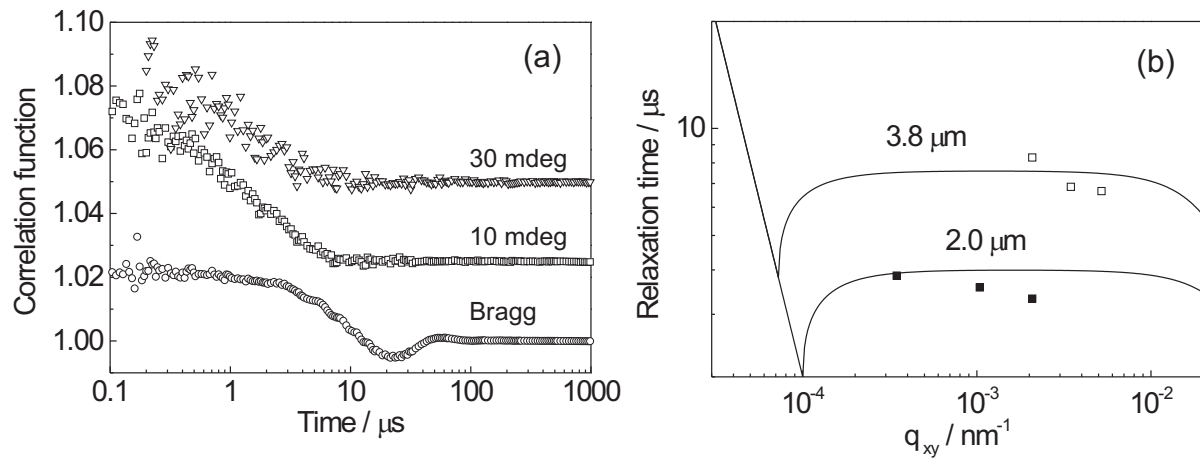
Figure 5.4: XPCS measurements of 8CB membranes. (a) Correlation functions for a thickness of 2.0 μm at the off-specular scattering angles indicated. (b) Experimental relaxation times at off-specular positions for the thicknesses indicated; solid lines give the theoretically calculated dispersion curves.

Figure 5.5: Autocorrelation functions of a 13.2 μm thick FPP membrane around the first Bragg position. Filled circles: specular position; open triangles: 10 mdeg offset; filled triangles: 12 mdeg offset; open circles: 15 mdeg offset. The upper curves have been vertically shifted for clarity (from top to bottom) by 0.085, 0.06 and 0.03, respectively.

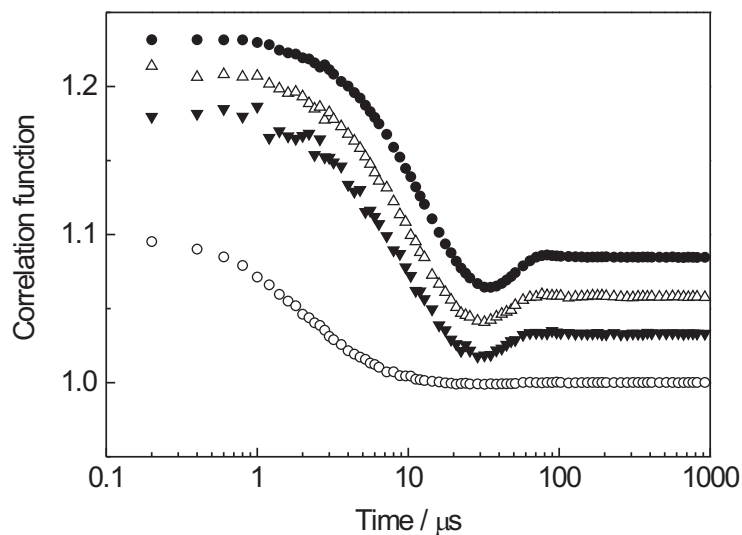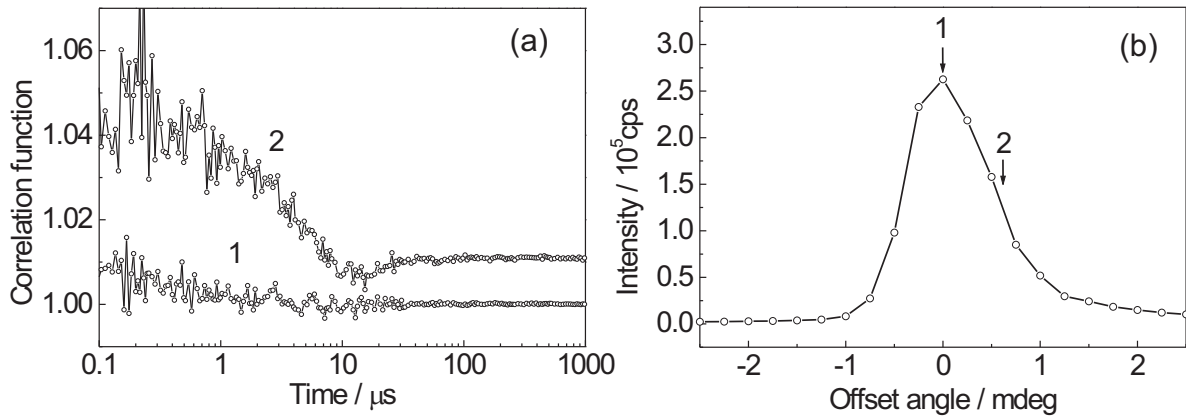*Figure 5.6: XPCS measurements of a highly ordered (1 mdeg mosaic distribution) 0.05 μm thick FPP membrane. (a) Correlation functions at the specular position q_z=1.16 nm^{-1} (1) and at half intensity (2). Curve 2 has been vertically shifted by 0.01 for clarity. (b) Rocking curve indicating the measurement positions.*
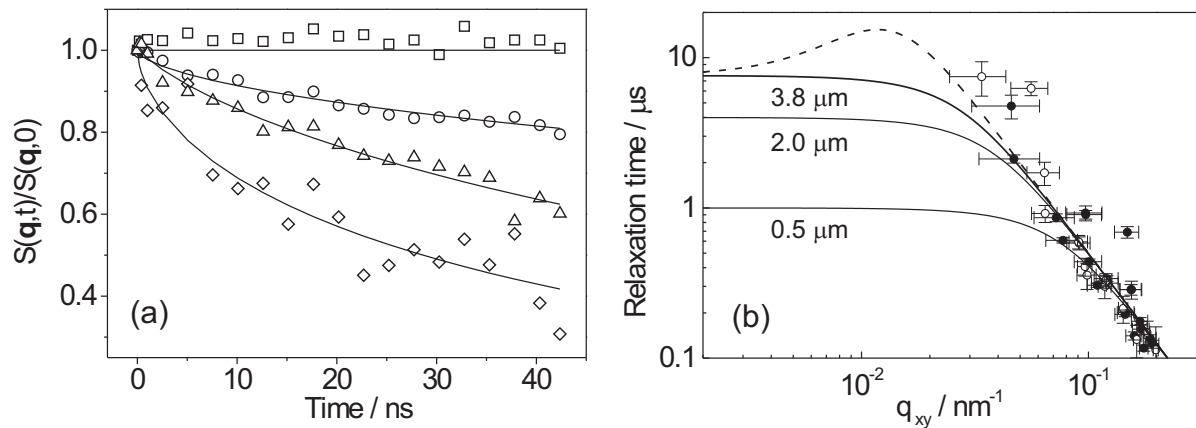
Figure 5.7: NSE results of thick (μm range) 8CB membranes around the first Bragg position. (a) Intermediate scattering function for different positions; squares: specular; circles: 0.1 nm^{-1} offset; triangles: 0.15 nm^{-1} offset; diamonds: 0.24 nm^{-1}; full lines: fits to a KWW function with $\beta = 0.59$. (b) Experimental relaxation times for various samples; open circles: NSE at 1.5 nm; closed circles: NSE at 0.9 nm; solid line: dispersion curves calculated for the thicknesses indicated (incompressible membranes); dashed line: calculation for the 3.8 μm membrane with finite compressibility ($B = 10^6$ N/m^2).

5.2   Discussion

5.2.1   Off-specular results: Surface and bulk-elastic regimes

In order to probe with XPCS fluctuations of a particular wavelength, the projection of the scattering vector on the membrane surface should match the wave vector of interest. In x-ray reflectivity this is accomplished by choosing an off-specular angle corresponding tho the desired value of q_{xy}. In Fig. 5.4b the relaxation times from such off-specular measurements have

been plotted together with the theoretical dispersion curves. In the range accessible by XPCS no dependence of the relaxation time on q_{xy} is observed, in agreement with the plateau in the theoretical dispersion curves. The relaxation times scale with the thickness of the membrane as expected from Eq. (4.43). Note that at these off-specular positions no reference signal is present, resulting in a homodyne detection scheme. According to the Siegert relation then the intensity correlation function is proportional to $|g_1(t)|^2$, which results for exponential decay in a relaxation time $\tau/2$. Hence the values obtained from the experiment have been multiplied by 2 to obtain τ.

For the relatively fast relaxation times involved in smectic membranes, XPCS requires a minimum intensity of the order of 10^4 cts/s. Hence in spite of large count rates at the specular Bragg position, the steep decrease of the scattered intensity with off-specular angle limits the accessible range of q_{xy}-values. As a results the accessible wave vector values are all at the plateau region of the dispersion curve. Larger off-specular scattering angles could be achieved in NSE experiments. The large size of the neutron beam in combination with the integration over the detector area results in sufficiently large count rates at off-specular positions as large as several degrees. As NSE is a quasi-elastic scattering technique, each scattered neutron carries useful information. Pairs of photon detection events must be counted to calculate the intensity correlation. As the wavelength of the neutrons is comparable to the x-ray wavelength in XPCS, the NSE scattering offset angles of several degrees result in values of q_{xy} that are up to two orders of magnitude larger than probed by XPCS.

In Fig. 5.7b the averaged values of the NSE relaxation time (see Eq. (3.15)) are plotted together with the theoretical dispersion curves. The data shows a q_{xy}-dependence that is related to bulk elastic effects. From Eq. (4.43) we expect a $1/q_{xy}^2$ dependence of the relaxation time, well in agreement with the experimental results. Moreover, no thickness dependence is present anymore, as expected from theory, which is convenient in light of the nonuniform thickness of the large-size NSE samples. This lead to measurement results that are a superposition of data for different values of L.

In the above discussions we assumed so far that the smectic membranes are incompressible. This approximation works well for fluctuations with a wave vector in the oscillatory or surface regime. It breaks down at larger q_{xy}-values [21], for which a finite compressibility might play a role. As indicated in Fig. 5.7b, the effect of a finite compressibility on the relaxation times manifests itself in a transition region between the surface and bulk-elasticity regimes. Some NSE results in Fig. 5.7b in the vicinity of this area extend above the high-compressibility limit,

which could indicate that finite compressibility comes into play. However, these relaxation times are in the time range up to 100 ns, which is at the limit of the possibilities of NSE. Hence the correlation functions in this region carry significant uncertainty, which prevents any further quantitative evaluation.

5.2.2   Specular results: Oscillating regime

From the discussion so far it is clear that with decreasing off-specular angle fluctuations are probed with a smaller wave vector. Ultimately, at the specular position we reach the limit $q_{xy} = 0$. According to Fig. 4.2a in this limit the relaxation time should become infinite, while the experiments of Fig. 5.1 indicate finite times. Evidently, it is a priori not clear what is the decisive wave vector q_{mn} at the specular ridge. The experimental results suggests that also at the specular position a window of finite q_{xy}-values determines the XPCS results by selecting fluctuations q_{mn} in the oscillatory regime. Accepting this concept for a moment, we can investigate some of its implications. We note from Fig. 4.2b that the frequency of the oscillations should become smaller for thicker membranes, which fits to the observed shift of the minimum of the oscillations to longer times for thicker membranes in Fig. 5.1. For even thicker 4O.8 membranes the wave-vector window selects fluctuations from the exponential regime above the cross-over wave vector q_c, leading to exponential relaxations at the specular ridge (Fig. 5.1). At the same membrane thickness, q_c is larger for FPP than for 4O.8. As q_c varies as $1/\sqrt{L}$ (see Eq. (4.40)), this causes for FPP potential exponential relaxations at the specular Bragg position to shift to larger thicknesses beyond our experimental possibilities. Exponential relaxation at the specular ridge has only been observed for FPP at the second Bragg position. This indicates that the wave-vector window of contributing fluctuations has indeed shifted to larger values and passed q_c.

The above explanation evidently requires that we can establish a window of q_{xy}-values that defines the range of wave vectors q_{mn} dominating the XPCS measurements at the specular position. In the following we propose such a mechanism by a combination of two 'filters', cutting the low and the high wave-vector range, respectively. The high-pass 'filter' is related to the movement of the illuminated area of the membrane as a whole (center-of-mass movement), the low-pass 'filter' to the width of the rocking curve (mosaic distribution).

In Sec. 2.1.2 we introduced the reference intensity signal I_0, which is related to the movement of the coherence volume as a whole. In other words to the movement of the center-of-mass (CM) of the coherence volume. Fluctuations of a wavelength larger that the size of the
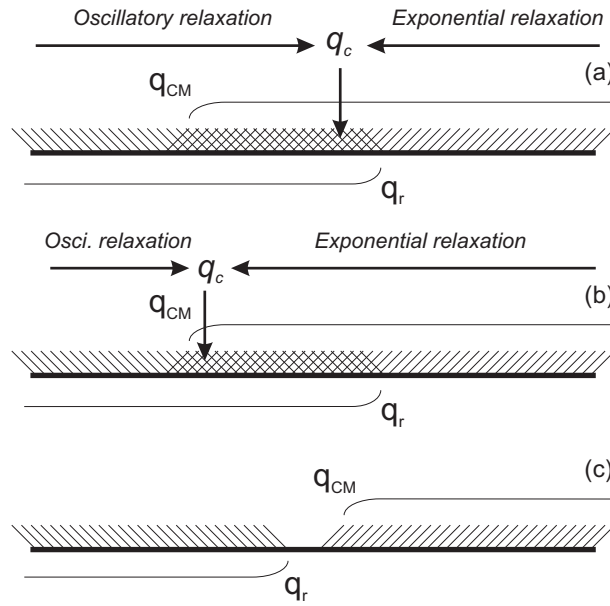
Figure 5.8: Schematic representation of the window defined for XPCS by the center-of-mass movement and the mosaic distribution (see text). (a) The correlation function exhibits oscillatory relaxation when q_c is situated at the high-q side of the window. (b) As q_c shifts to lower q-values in the window exponential relaxation takes over. (c) Representation of zero contrast near $q_{xy} = 0$.

coherence volume contribute effectively mainly to this CM movement. In contrast, fluctuations of a wavelength smaller than the coherence volume hardly shift the center of mass, but do contribute to the correlation function measured in XPCS. Let us define q_{CM} as the wave vector of a fluctuation of a wavelength matching the size of the coherence volume. The value of q_{CM} is defined by the coherence properties of the incident beam and the resolution of the setup. For 4O.8 the experimentally observed transition to the exponential regime occurs close to a thickness $L \approx 10\ \mu$m. Using Eq. (4.40) we can calculate the corresponding value $q_c \approx 0.08\ \mu$m^{-1} which corresponds to a projection of the transverse coherence length on the membrane of about $80\ \mu$m. Accepting this value for a moment, the transition thickness for FPP would be $L \approx 70\ \mu$m (using the parameters from Table 3.1). As the thickest samples measured were $\lesssim 20\ \mu$m, this explains indeed why for FPP no transition to the exponential regime was observed at the specular Bragg position. On the other hand, at the second Bragg peak exponential relaxation was observed for a 13.2 μm FPP membrane (see Fig. 5.2). Because of the twice smaller projection of the coherence length at this position, here the transition thickness would be four times smaller at about 17 μm, which is the right order of magnitude. We conclude that the estimates given explain the trend in the data rather well, but quantitatively the projected coherence length of about $80\ \mu$m is a factor $3-4$ too small. Such difference might be related to the speckle structure which was observed in the incident beam and could have been caused by some optical ele-

ments in the fly path. In summary, q_{CM} gives the position of a 'high-pass filter' of wave vectors of fluctuations contributing to the correlation function measured by XPCS. Short wave vectors (long wavelengths) below this value contribute mainly to the CM movement.

A second factor that influences the XPCS results is the mosaic distribution of the sample. It can be quantified using the width of the rocking curve, to be indicated as q_r. This width indicates a range of projections of scattering vectors that contribute to the intensity measured at the Bragg position. Each contribution corresponds to scattering from fluctuations with a wave vector matching the projection of the scattering vector on the surface of the membrane. The intensity profile of the rocking curve weights the contribution of each particular wave vector to the total intensity at the Bragg position. Hence q_r can be considered as a 'low-pass filter' of fluctuations influencing the XPCS signal, cutting off input from larger q_{xy}-values. The contribution of each fluctuation is proportional to the intensity at the corresponding off-specular position. This will effectively suppress input from fluctuations with large values of q_{mn}.

Considering the three parameters: q_{CM}, q_r and q_c we can build a complete picture of the XPCS results. The quantities q_{CM} and q_r define a window ('bandpass') determining the range of the wave vectors detected. In Fig. 5.8 we indicate three possible scenarios that depend crucially on the position of q_c with respect to this window. In case (a) the cross-over wave vector q_c is positioned close to the upper edge of the window. In this situation mainly fluctuations *below* q_c contribute to the scattered intensity and we observe oscillatory behavior. In case (b) the positions of q_{CM} and q_r are still the same, but q_c is situated closer to the lower edge of the window. Consequently, fluctuations *above* q_c will prevail and we expect to observe simple exponential relaxation in XPCS. In case (c) there is no intersection between low- and high-pass filter. This means that fluctuations contributing to the XPCS signal only translate the scattering volume as a whole without changing the total intensity. This results in the absence of the contrast in specular measurements. This situation corresponds to the measurement at $q_{xy} = 0$ indicated in Fig. 5.6.

Let us make some estimates to connect the results of Fig. 5.6 in more detail to Fig. 5.8c. At the specular position ($q_z = 1.16$ nm^{-1}) the width of rocking curves from the most uniform, resolution-limited samples is below 1 mdeg. An offset of 1 mdeg corresponds to a projection of the scattering vector on the surface $q_x = 2.0 \cdot 10^{-5}$ nm^{-1} or a lateral size of about 300 μm. This values is comparable to the estimated length of the coherence volume. Consequently, at the specular ridge fluctuations are detected with a wavelength larger than the coherence volume. As argued above, these do not contribute to the XPCS signal. On the other hand, contributions
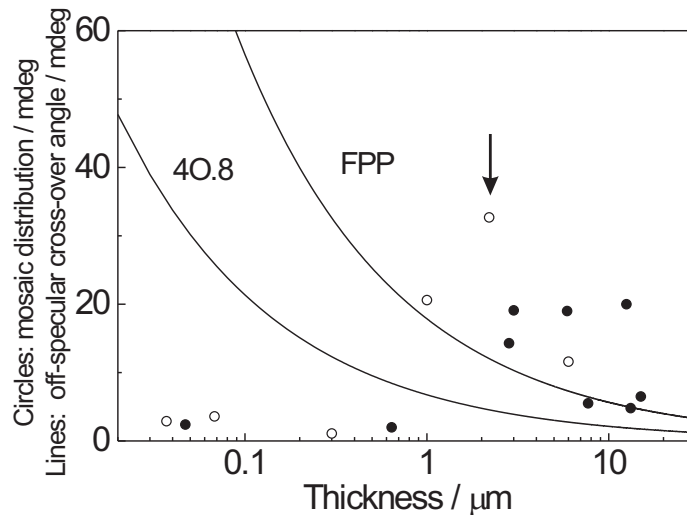
Figure 5.9: Lines: Thickness dependence of the scattering angle corresponding to q_c for 4O.8 and FPP membranes. Circles: rocking curve widths for 4O.8 (open circles) and FPP (filled circles) for the thicknesses investigated. The arrow indicates exponential relaxation; all other points correspond to the oscillatory relaxation regime.

from shorter wavelength fluctuations are not detected at the Bragg position because of the narrow resolution; they start to contribute only at off-specular positions. This is exactly the situation pictured in Fig. 5.8c. As a result only membranes with a rocking curve width larger than about 1 mdeg provide enough contrast to measure a correlation function at the specular Bragg position.

Figure 5.9 displays the scattering angle corresponding to q_c versus membrane thickness. Superimposed are rocking curve widths from which we can estimate whether the observed relaxation should be oscillatory or exponential. For points below the cross-over curve, the main contribution to the resulting XPCS signal stems from fluctuations with oscillatory relaxation. For the points well above the curve, fluctuations with exponential relaxations will play a major role. In Fig. 5.9 we see several point above the corresponding curves which still exhibit oscillatory relaxation. This indicates that the influence of overdamped relaxations in this cases is not strong enough to suppress the contributions from oscillating fluctuations. The only point exhibiting exponential relaxation is indicated by an arrow. It is a thin 2.2 μm 4O.8 membrane with accidentally an unusually large 32 mdeg broad mosaic distribution, lying well above the corresponding curve. As a consequence overdamped fluctuations become dominant in the measurements of this sample and we observe exponential relaxation, even through some thicker membranes with narrower rocking curves still exhibit oscillatory behavior.

In Sec. 4.2 we discussed the surface dominated exponential relaxation regime for fluctuations with a wave vector $q_{xy} > q_c$ leading to a relaxation time $\tau = \eta_3 L/(2\gamma)$. This result has been previously obtained in a quasi-stationary model neglecting inertia of the smectic membrane [56]. In such a model no oscillatory regime is present and the exponential relaxation regime extends to $q_{xy} = 0$. A linear dependence of the relaxation time on thickness was reported by Price *et al.* [56] at the specular Bragg position for samples of various different materials with thicknesses $\gtrsim 5$ μm. Figure 5.9 indicates that for these thicknesses exponential relaxations could be dominant. However, In these early XPCS measurements with soft x rays, the mosaic distribution of the smectic membranes was rather large. According to Fig. 5.9, which might also play a role. Such large values of q_r lead in Fig. 5.8 to a broad overlap area; in particular the right edge of the window extends to large wave-vector values. This results in dominance of fluctuations with exponential relaxation, in agreement with the observation of exclusively exponential relaxation in the XPCS experiment of Ref. [56].

5.3   Conclusions

Combining XPCS and NSE methods we have mapped out the three different relaxation modes in smectic liquid crystal membranes predicted by theory: oscillatory relaxations, surface dominated exponential relaxations and bulk-elasticity dominated exponential relaxations. A critical wave vector q_c separates the first from the latter regimes. Fluctuations with a wave vector $q_{mn} < q_c$ exhibit oscillatory relaxation. In the region $q_{mn} > q_c$ fluctuations lead to simple exponential relaxation. For small wave vectors q_{mn} (but above q_c) the exponential relaxation time does not depend on the wave vector and is defined by surface tension, thickness and viscosity of the membrane. This behavior has been observed in a series of off-specular XPCS experiments, for which the relaxation time was independent of the scattering angle. For larger wave vectors q_{mn} the exponential relaxation times are determined by the bending elasticity of the smectic layers and decrease as $1/q_{mn}^2$. This regime has been probed by NSE measurements thanks to the accessibility of an order of magnitude larger off-specular scattering angles compared to XPCS. The NSE results indicate a decrease of the relaxation time with increasing scattering angle as predicted.

XPCS measurement at specular positions are dominated by a 'window' of wave vectors cutting longer and smaller values. This window results from a combination of the finite resolution of the setup selecting long wavelength fluctuations, and the size of the coherence volume inside which short wavelength fluctuations perturb the density profile, and is given by the overlap

of these two regimes. For thin membranes this window is dominated by fluctuations with $q_{mn} < q_c$, resulting in oscillatory behavior of the intensity correlation function. For thicker membranes the cross-over wave vector q_c shifts towards smaller values and the window of contributing fluctuations is dominated by exponential relaxations. For extremely well-ordered membranes characterized by a narrow rocking curve $\lesssim 1$ mdeg, the wave vector window is empty, which results in the absence of any contrast in the specular correlation function.

Chapter 6

Coherence in x-ray photon correlation spectroscopy experiments

In x-ray photon correlation spectroscopy (XPCS) the degree of coherence of the x-ray beam determines the contrast of the observed intensity correlation function. In this chapter we present XPCS measurements of smectic liquid crystal membranes in a reflectivity geometry showing that both coherence and resolution can influence the time dependence of the correlation function. Variation of the pre-detector slits as well as of the projected coherence length on the membrane induce a time dependence of the intensity correlation function. We also treat several practical aspects and limitations we encountered during our XPCS studies. Finally the conditions for heterodyne detection at the specular ridge and homodyne detection at off-specular conditions are discussed.

6.1   Introduction

In the absence of x-ray lasers a paramount problem in XPCS is to get sufficient scattered intensity. A sufficient degree of coherence can only be obtained by selecting via a pinhole the central flat wavefront from an incoherent source at large distance. For the small wavelength involved in x rays the beam must be collimated down to micron size, which results in a large loss of intensity. In addition effects of beam damage put a limit on the incoming flux of the x rays that can be accepted. As a consequence scattering geometries have to be used in XPCS that differ from those in conventional photon correlation spectroscopy (PCS). This has unveiled new ways in which both the coherence properties of light and the resolution of the setup influence the measurements.

Because of the Landau-Peierls instability the layer-displacement correlation function $\langle u(\mathbf{r}_1, 0) u(\mathbf{r}_2, t) \rangle$ diverges when the wave vector of the fluctuations approaches $\mathbf{q} \rightarrow 0$. To avoid this complication a cut-off parameter has been introduced, which defines the longest wavelength of the fluctuation present in the system [10] (see Sec. 4.2). For finite-size membranes this parameter is expected to be at the order of the lateral dimension of the membrane. However, fitting of the experimental data revealed that the cut-off value was closer to the footprint of the beam on the surface of the membrane [58, 59]. This result establishes a connection with the dimension of the coherently illuminated volume of the sample from which the scattering image (speckle pattern) originates. For a complex optical system the phase profile over the wavefront is intricate [95]. In this case one can describe the coherence properties of the beam by the complex degree of coherence $\mu(\mathbf{r}_1, \mathbf{r}_2)$ (see Sec. 2.1.4). This parameter can be measured in, for instance, a double slit experiment. In that situation the transverse coherence length can be identified with the slit separation corresponding to the maximum of the zeroth order of $\mu(\mathbf{r}_1, \mathbf{r}_2)$. However, maxima corresponding to higher orders of $\mu(\mathbf{r}_1, \mathbf{r}_2)$ are present that manifest phase correlations in the wavefront at longer distances. The latter correlations could play a vital role as they probe fluctuations with a long wavelength that provide a dominant contribution to $S(\mathbf{q}, t)$, since they diverge for $\mathbf{q} \rightarrow 0$.

In order to quantify the observed changes in correlation functions one could attempt to fit them directly to Eq. (2.5) for $S(\mathbf{q}, t)$. However, because of the complicated intrinsic q-dependence, which has to be integrated out, we started with a more empirical approach based on the simpler functional dependence (oscillatory relaxation) of Eq. (5.1):

$$\frac{\langle I(0) I(t) \rangle}{\langle I \rangle^2} = A \exp(-t/\tau) \cos(\omega t + \phi). \tag{6.1}$$

The arguments given above suggest that variations of the scattering volume could lead to different relaxation profiles. In the following sections we present several experiments illustrating this statement. First we show that variation of the detector slits results in a shift of the correlation function. Subsequently we discuss changes of the projection of the coherence length that also induce a time dependence of intensity correlation function. Finally the question of homodyne vs. heterodyne detection will be considered.

6.2 Resolution effects from the pre-detector slits

In this section we illustrate the influence of the resolution of the setup on the time dependence of the intensity relaxation function at the quasi-Bragg peak of FPP ($q_0 = 2.14$ nm^{-1}) by changing the detector slit in either the horizontal or the vertical direction. A first set of measurements was made with a 10 μm pinhole and a horizontal scattering plane (vertical membrane). The results are displayed in Fig. 6.1. Opening of the horizontal detector slit results in a strong loss of contrast and a shift of the correlation function towards longer relaxation times. On the other hand opening the vertical (out-of-plane) detector slit leads only to minor changes. Similar results are found in the case of a horizontal membrane (vertical scattering plane), in which the horizontal and vertical slits switch over their roles (see Fig. 6.2). In Fig. 6.3 we give results for a 100 μm pinhole (vertical membrane). In this case both the vertical and the horizontal slit influences the correlation function, slowing down the correlation time while also the contrast diminishes.

The results for the curves from Fig. 6.1, Fig. 6.2 and Fig. 6.3 are given in Table 6.1, Table 6.2 and Table 6.3, respectively. The frequency of the oscillatory part is constant for vertical membranes. On the other hand the phase factor remains overall constant within the experimental accuracy. The results for contrast and relaxation times can be summarized as follows.

- For the 10 μm pinhole increasing the in-plane pre-detector slit leads to (i) an important loss of contrast, and (ii) an increase of the relaxation time. Increasing the out-of-plane detector slits gives (i) a small but significant decrease of contrast and (ii) no change of the relaxation time. These results are independent on whether the scattering plane is horizontal or vertical. Note that a decrease of contrast is not necessarily connected with a variation of the correlation time.

- For the 100 μm pinhole the initial contrast is less than in the previous case. Upon increasing the width of a pre-detector slit (either in-plane or out-of-plane) the contrast is strongly reduced and the relaxation time increases.
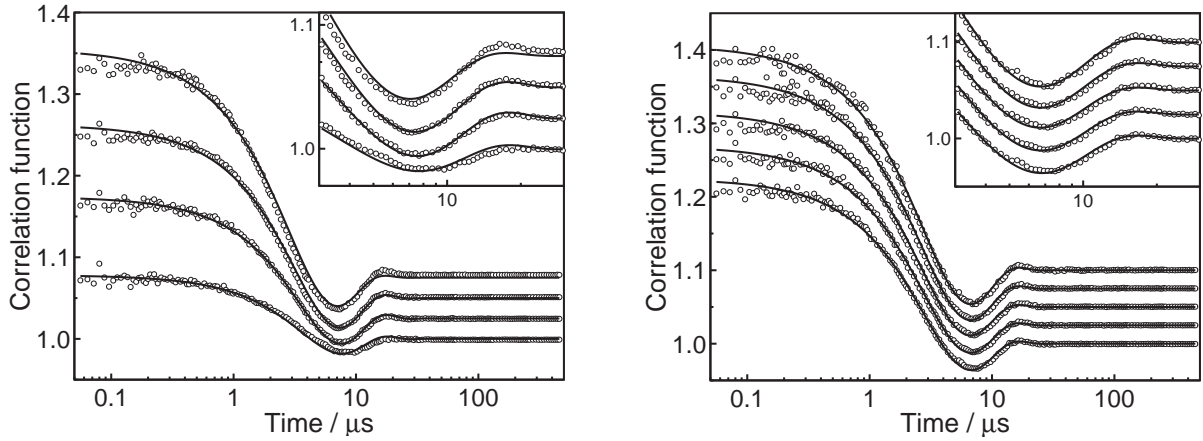
Figure 6.1: Correlation functions from a 1.7 μm vertical FPP membrane (10 μm pinhole). Left: Vertical slit fixed at 0.02 mm, horizontal slit (from top to bottom): 0.03, 0.06, 0.1, 0.2 mm. Right: Horizontal slit fixed at 0.02 mm, vertical slit (from above): 0.01, 0.03, 0.06, 0.1, 0.2 mm. Fit parameters in Table 6.1.

In-plane slit/mm	$A \pm 0.01$	$(\tau \pm 0.1)/\mu s$
0.03	0.29	3.8
0.06	0.22	4.6
0.1	0.16	5.2
0.2	0.08	5.7
Out-of-plane slit/mm	$A \pm 0.01$	$(\tau \pm 0.1)/\mu s$
0.01	0.33	3.9
0.03	0.31	3.9
0.06	0.29	3.9
0.1	0.26	4.0
0.2	0.24	4.0

Table 6.1: Fitting parameters to Eq. (6.1) for the correlation functions of the vertical FPP membrane of Fig. 6.1. Top: vertical slit fixed at 0.02 mm; bottom: horizontal slit fixed at 0.02 mm; $\omega = 0.30 \pm 0.02\ \mu s^{-1}$, $\phi = 0.3 \pm 0.1$.

The size of the 10 μm pinhole is less or about equal to the vertical and horizontal coherence length, respectively. Hence the radiation passed through has approximately symmetric coherence. For in-plane scattering the projection of the transverse coherence length ξ_{tr} on the surface of the membrane is at the quasi-Bragg angle about 300 μm (the size of the footprint of the beam). In the out-of plane direction it is still about the size of the pinhole. In the latter direction one or just a few speckles are accepted by the detector and further opening of the vertical slit leads to a moderate decrease in contrast. However, in the scattering plane at least
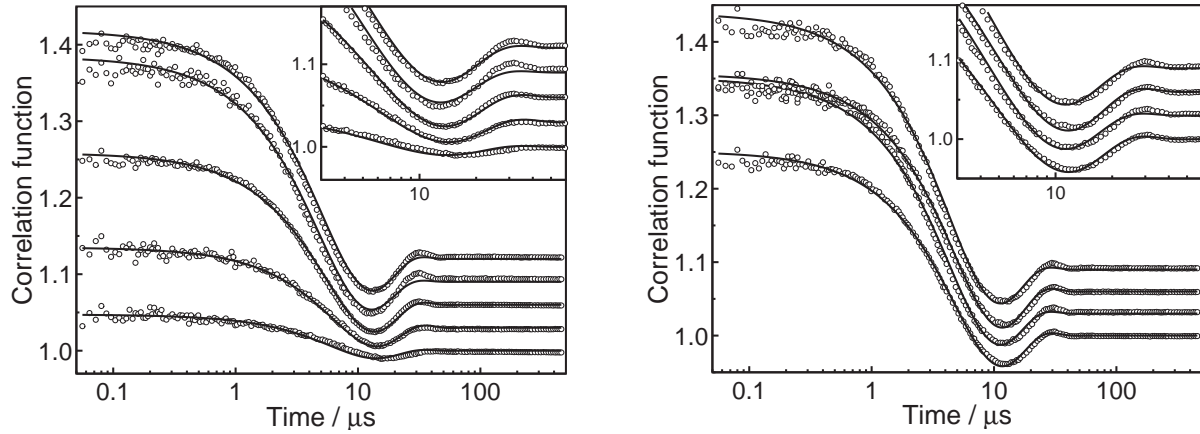
Figure 6.2: Correlation functions from a 1.4 μm horizontal FPP membrane (10 μm pinhole). Left: Horizontal slit fixed at 0.02 mm; vertical slit (from top to bottom): 0.01, 0.03, 0.06, 0.1, 0.2 mm. Right: Vertical slit fixed at 0.02 mm, horizontal slit (from top to bottom): 0.01, 0.03, 0.06, 0.2 mm. Fit parameters in Table 2.

In-plane slit/mm	$A \pm 0.01$	$(\tau \pm 0.1)/\mu s$
0.01	0.33	6.9
0.03	0.34	7.4
0.06	0.22	8.5
0.1	0.12	10.2
0.2	0.05	9.6
Out-of-plane slit/mm	$A \pm 0.01$	$(\tau \pm 0.1)/\mu s$
0.03	0.39	6.2
0.06	0.33	7.1
0.1	0.36	6.2
0.2	0.28	7.1

Table 6.2: Fitting parameters to Eq. 6.1 for the correlation functions of the horizontal FPP membrane of Fig. 6.2 (10 μm pinhole). Left: horizontal slit fixed at 0.02 mm; right: vertical slit fixed at 0.02 mm; $\omega = 0.16 \pm 0.02 \ \mu s^{-1}$, $\phi = 0.4 \pm 0.1$.

ten times more speckles will be received by the detector, and further opening will strongly reduce the contrast which in fact almost disappears. The 'effective' resolution $\Delta q'_x$ (Eq. 2.29) is determined by the largest of the two values $1/\xi_{tr} \leq 10^{-5}$ nm^{-1} and $\Delta q_x \simeq 10^{-4}$ nm^{-1}. Hence for in-plane scattering $\Delta q'_x$ is mainly determined by the resolution of the setup. When we open the detector slits we decrease the resolution, and thus the cut-off wavelength Λ, leading to a larger relaxation time.
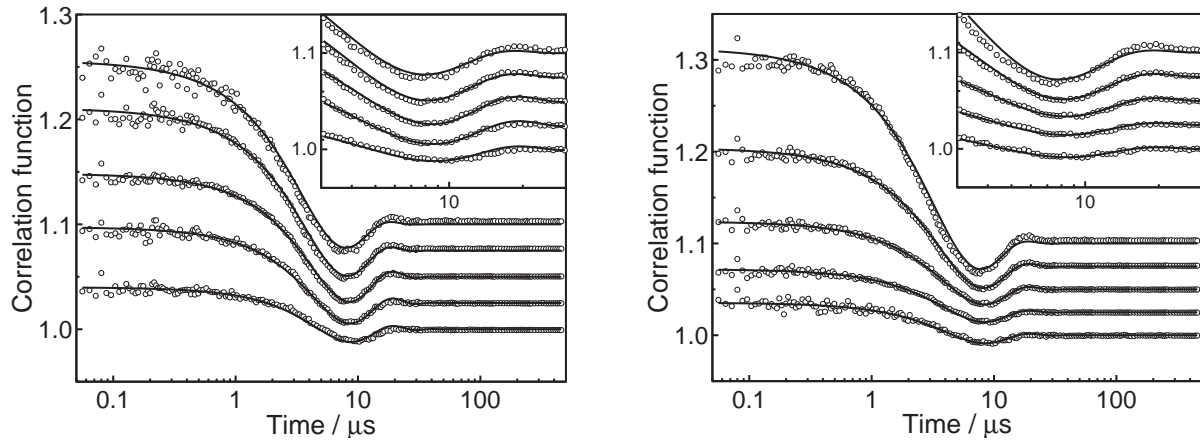
Figure 6.3: Correlation functions from a 1.4 μm vertical FPP membrane (100 μm pinhole). Left: Vertical slit fixed at 0.02 mm, horizontal slit (from top to bottom): 0.01, 0.03, 0.06, 0.1, 0.2 mm. Right: Horizontal slit fixed at 0.02 mm, vertical slit (from top to bottom): 0.01, 0.03, 0.06, 0.1, 0.2 mm. Fit parameters in Table 6.3.

In-plane slit/mm	$A \pm 0.01$	$(\tau \pm 0.1)/\mu s$
0.01	0.16	4.6
0.03	0.14	5.3
0.06	0.1	6.5
0.1	0.07	7.1
0.2	0.04	7.8
Out-of-plane slit/mm	$A \pm 0.01$	$(\tau \pm 0.1)/\mu s$
0.01	0.22	4.3
0.03	0.13	5.3
0.06	0.08	6.0
0.1	0.05	6.1
0.2	0.04	6.5

Table 6.3: Fitting parameters to Eq. (6.1) for the correlation functions of the vertical FPP membrane of Fig. 6.3. Left: vertical slit fixed at 0.02 mm; right: horizontal slit fixed at 0.02 mm; $\omega = 0.29 \pm 0.02\,\mu s^{-1}$, $\phi = 0.2 \pm 0.1$.

For in-plane scattering, in the case of a 100 μm pinhole we have factor 10 larger footprint than for a 10 μm pinhole. However, the projection of the coherence length ξ_{tr} on the surface of the membrane is still about the same. Hence we can apply essentially the same arguments as in the 10 μm case. For the out-of-plane scattering the beam size is now about 100 μm while the coherence length is of the same order. This brings the out-of-plane behavior to the same scale as

discussed for the in-plane scattering, resulting in the similar behavior observed experimentally. In conclusion these results illustrate that in the present coherent experiments the whole set-up after the pinhole should be considered as 'sample'.

6.3 Dependence of the relaxation on q_z

So far we have been working exclusively at the quasi-Bragg peak corresponding to the layer structure of the smectic membranes. Moving along the specular ridge provides a means of varying the projection of the beam (and thus of the coherence length) on the surface of the membrane. To achieve a high enough count rate at different specular positions, we measured a relatively thin 13-layer 4O.8 membrane, giving broad Kiessig fringes (see Fig. 6.4a). Correlation functions taken at the maxima of the Kiessig fringes and at the quasi-Bragg position are shown in Fig. 6.4b. The results of fitting the data to Eq. (6.1) are displayed in Fig. 6.4c, and indicate shorter relaxation times as we move towards larger scattering angles. Finally Fig. 6.4d shows an increase in contrast parallel to the variation of the relaxation time with q_z.

The results can easily be understood within the framework of our model given in the previous section. For in-plane scattering now the projection on the membrane surface of both ξ_{tr} and $1/\Delta q_x$ varies inversely proportional to q_z. Hence it does not matter which quantity is dominant. This projection directly determines the largest wavelength of the detected fluctuation which decreases with increasing scattering angle leading to the observed shift of the correlation function towards faster times. Comparing Figs. 6.4a and 6.4d we note that the contrast increases with decreasing intensity of the Kiessig fringe (or quasi-Bragg peak).

Another potential possibility to vary q_z is to work at the position of the second-order quasi-Bragg peak. In FPP the presence of fluorine leads to an increased intensity ratio of the second and first quasi-Bragg peak of about 10^{-4}, which is for other liquid crystals usually about $10^{-6} - 10^{-7}$. This allowed us to measure correlation functions at both the first- and the second-order Bragg position of a thick FPP membrane, shown in Fig. 5.2. At these positions both the illuminated footprint and the coherence volume differ by a factor two. At the second quasi-Bragg position we should probe maximum fluctuations with a twice shorter wavelength than at the first one. The data show at the first Bragg peak oscillatory relaxation (complex mode, see Fig. 4.2), and at the second Bragg peak a pure exponential relaxation. As the latter slow-mode relaxation time does not depend on the wavelength of the fluctuations, we cannot decide on an exact factor of two difference. However, the change in mode is important, as this is the only example of FPP showing exponential relaxation on the specular ridge.
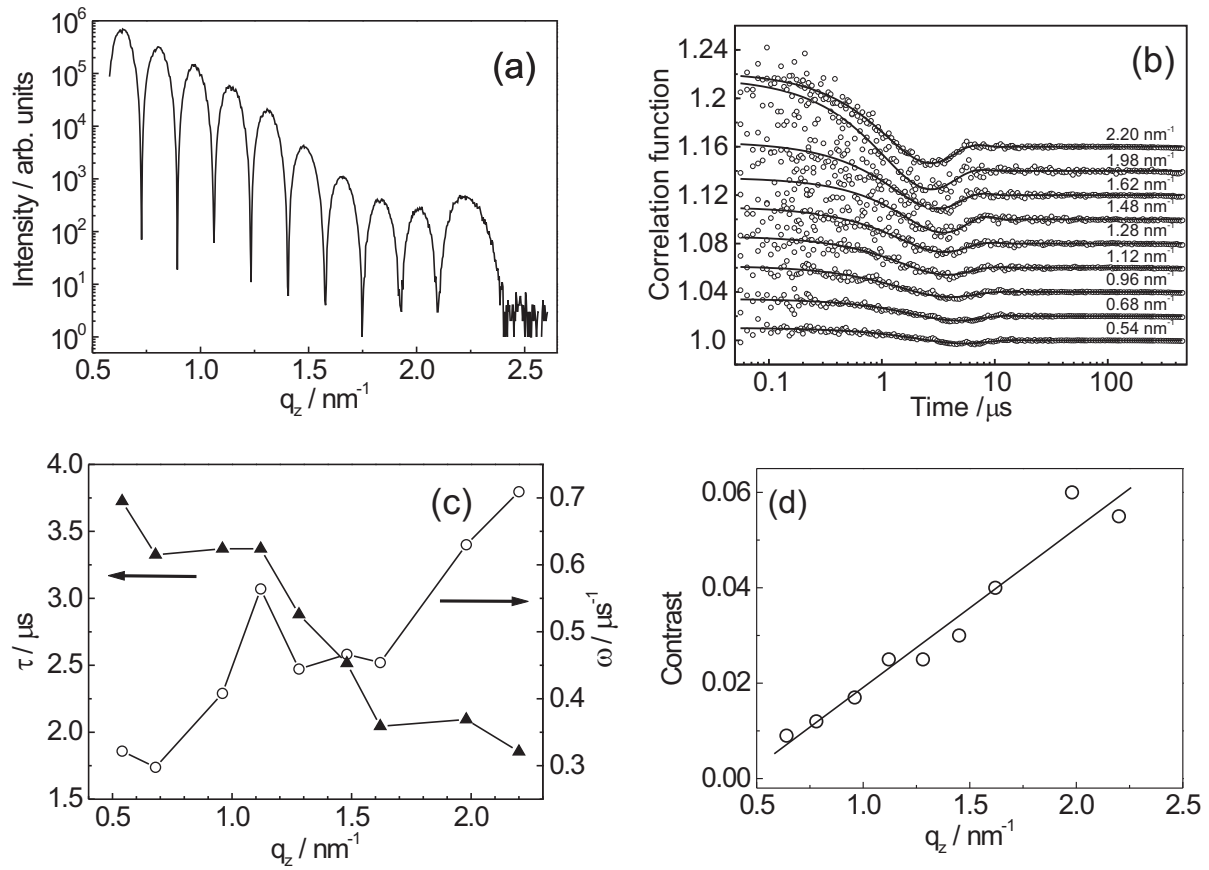
Figure 6.4: Results for a 13-layer 4O.8 membrane at different specular positions. (a) Reflectivity curve. (b) Correlation functions (10 μm pinhole) taken at the maxima of the Kiessig fringes (shifted along the vertical axis with values of q_z indicated). (c) Dependence of the fitting parameters τ (triangles) and ω (circles) on the position along the specular ridge. (d) Ibid for the contrast.

6.4   Coherence-induced modulations

In the reflectivity curves of several thin highly-oriented smectic membranes we observed on top of the standard reflectivity curve additional modulations (Fig. 6.5) with a periodicity of about 20 mdeg. These additional fringes have an M-shape with secondary minima at about half the main period (Fig. 6.6). A standard explanation would attribute such a modulation to different thicknesses of the film. However, several reasons make this unlikely. First this explanation would require rather thick islands on a thin film, which is not very probable. Second the modulation is also observed at the Bragg position. This would not be the case for multiple thicknesses as the Bragg position is the same for all thickness regions. Finally modulations with the same period are observed in samples of different thickness. Hence we conclude that the modulations have an external cause, probably related to the coherent properties of the beam. In perspective it is somewhat difficult to establish exactly the conditions under which

these modulations can be observed. The effect occurred spontaneously in several cases, but no systematic investigations were made. The relevant samples can be characterized as rather thin (thicknesses about $40-50$ nm) and highly oriented (mosaic below 1 mdeg). In all cases the $10\ \mu$m pinhole and the focussing Be lens were in place while the direct beam was not attenuated. Usually a sample in a coherent beam acts to some extent as a diffusor, decreasing the degree of coherence of the beam. Under the conditions described we seem to be in the other limit: the thin highly oriented smectic membranes act as almost perfect mirrors reflecting the coherent beam, of course on top of the Kiessig fringes and the quasi-Bragg peak as given by the reflectivity conditions.
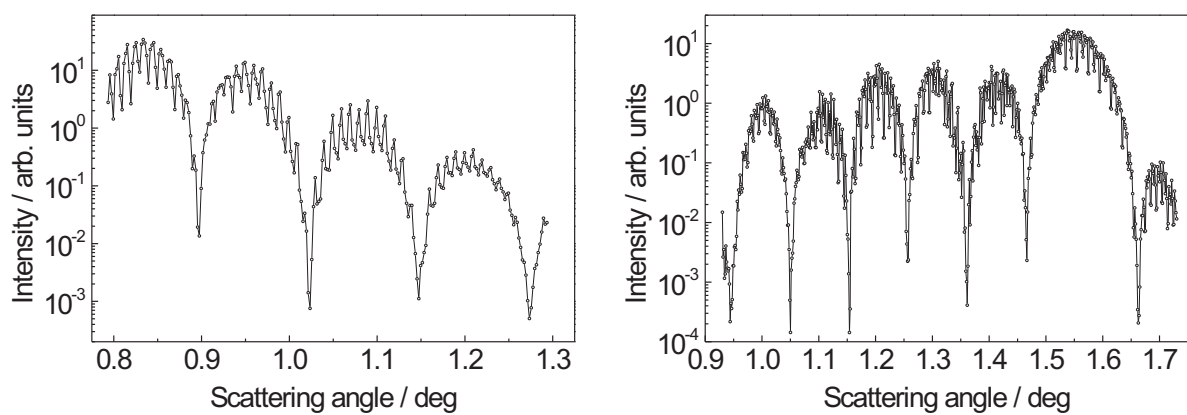

Figure 6.5: Reflectivity curves measured from (a) 35 nm thick FPP and (b) 43 nm thick 4O.8 membranes.
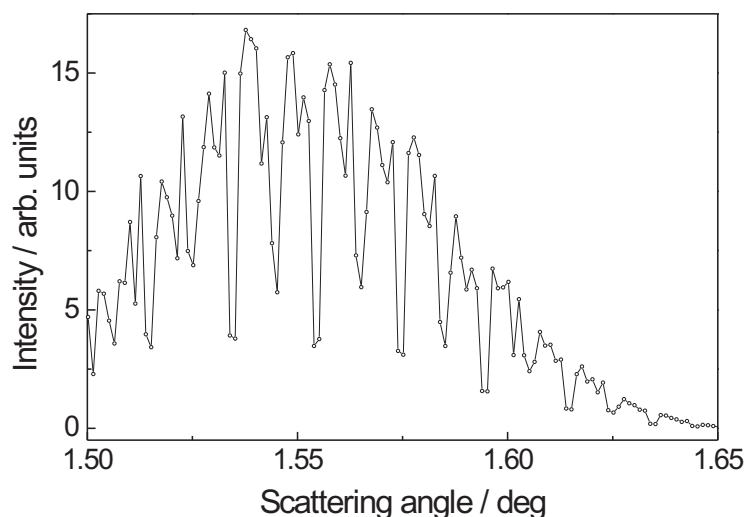

Figure 6.6: Magnification of the Bragg peak region from Fig. 6.5b.

It seems natural to consider these oscillations as a multiplcation of the Fraunhofer diffraction pattern [67] and the reflected intensity from the sample. However, Figs. 6.5 and 6.6 do not

show a static speckle pattern but reflectivity curves as a function of q_z. Hence the scattering from the sample is a convolution of the incident field with the density distribution in the sample. In this situation it is not clear how the Fraunhofer diffraction pattern could survive and lead to oscillations at the detector position.
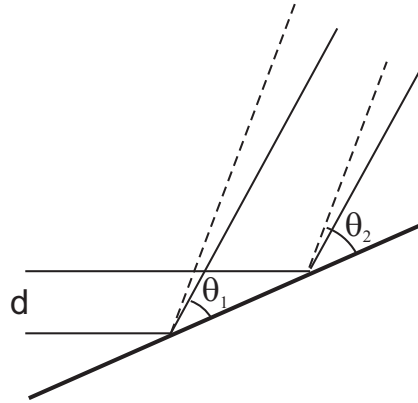

Figure 6.7: Pathway difference for the calculation of the source separation.

The data displayed in Figs. 6.5 and 6.6 resemble strongly a classical two-slit experiment [96, 97]. Hence they can be understood if we assume a split incident beam resulting in two reflection spots on the surface of the membrane. If the two sources are correlated they will create an interference pattern, which will modulate the reflectivity curves. Denoting the distance between the two sources by d and the scattering angles corresponding to two adjacent minima in Fig. 6.6 by θ_1 and θ_2, we can write (see Fig. 6.7):

$$d = \frac{\lambda}{2(\cos\theta_1 - \cos\theta_2)} \sin(\theta) = \frac{\lambda}{4\sin(\Delta\theta/2)\sin(\theta/2)} \sin(\theta) \approx \frac{\lambda}{\Delta\theta} \ . \tag{6.2}$$

Taking $\theta = (\theta_1 + \theta_2)/2 = 1.544°$, $\Delta\theta = \theta_1 - \theta_2 = 0.02°$ and $\lambda = 0.154$ nm, this explanation requires a spacing of the sources $d \simeq 0.4$ μm. Such a splitting could possibly result from a speckle pattern generated by one of the optical elements (monochromator crystal, mirror, Be-window) before the sample. As mentioned in Sec. 3.2, the incident beam was observed to be structured as measured by scanning with a 4 μm pinhole. However, a separation of 0.4 μm is evidently beyond this resolution or any other one that could be set in practice. The correctness of this explanation would be immediately evident from the effect of varying the size of the pinhole. Unfortunately this possibility was not considered at the time of the measurements that were in the first place aimed at unravelling the fluctuation dynamics of the smectic membranes.

6.5   Homodyne/heterodyne detection

As mentioned in Sec. 2.1.2 the density of a fluctuating smectic membrane can be decomposed into a time-independent (average) part and a time-dependent one. The presence or absence of the reference signal results in homodyne and heterodyne detection schemes, respectively. Fig. 6.8a shows some typical experimental results. Around the Bragg position we observe a
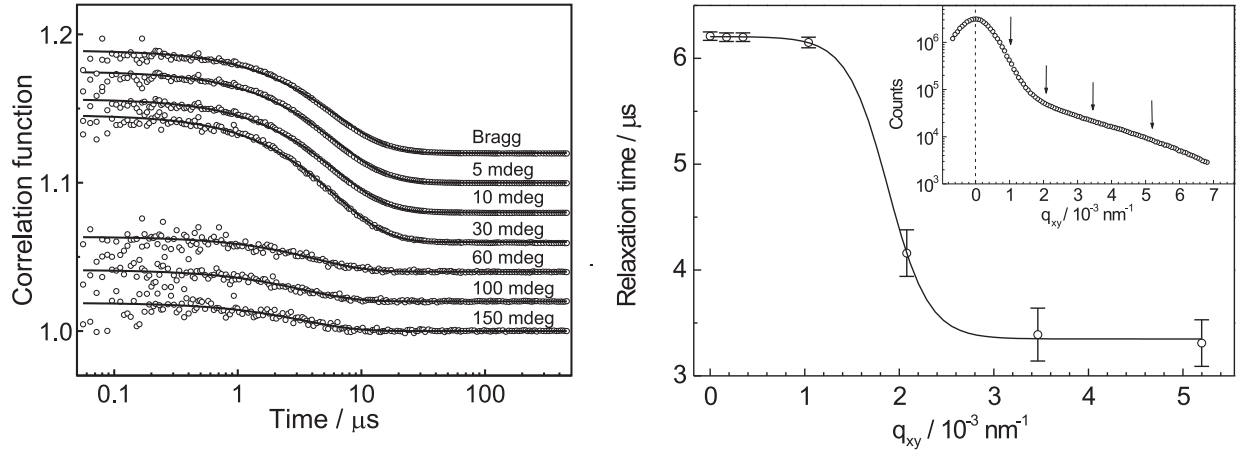

Figure 6.8: XPCS measurements of a 3.8 μm 8CB membrane at specular and off-specular positions. (a) Correlation functions at the positions indicated above each curve. (b) Variation of the relaxation times as a function of the offset. Inset: Rocking curve with arrows indicating the measurement positions.

specular relaxation time of 6.2 μs. After passing a threshold the correlation function transforms into another form with a different relaxation time. This transition manifests the switch from heterodyne to homodyne detection as the contribution of I_{ref} disappears. The threshold is determined by the angle for which the specular reflection falls on the edge of the detector area. The results given in Fig. 6.8b indicate a final off-specular relaxation time of 3.3 μs.

The difference of approximately a factor 2 becomes evident if we consider that in the intensity-intensity correaltion function (see Eq. 2.14) the heterodyne term depends linearly on $g_1(t)$ and the homodyne term on $g_2(t)$ which is proportional to $g_1^2(t)$ via the Siegert relation. If in the heterodyne regime the intensity correlator decays exponentially with a rate constant Γ:

$$\langle I(\mathbf{q}, 0) I(\mathbf{q}, t) \rangle \sim \exp(-\Gamma t), \tag{6.3}$$

we get in homodyne case according to the Siegert relation:

$$\langle I(\mathbf{q}, 0) I(\mathbf{q}, t) \rangle \sim \exp(-2\Gamma t). \tag{6.4}$$

Due to this effect the relaxation times obtained in homodyne scheme by fitting experimental intensity correlation functions to Eq. (6.1) is twice smaller than in heterodyne case [66].
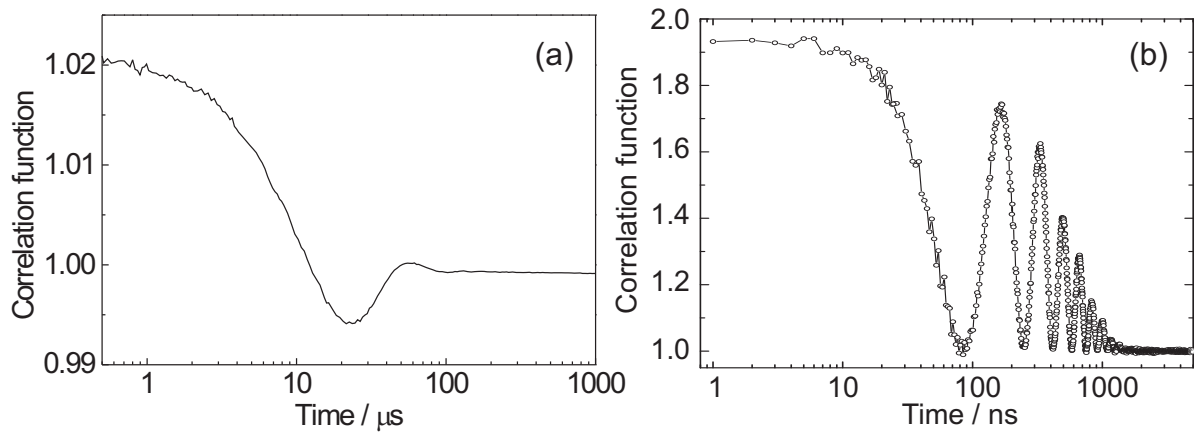

Figure 6.9: Correlation functions of an underdamped mode showing oscillations. (a) XPCS of a 2.5 μm thick 8CB membrane at the specular Bragg position (heterodyne). (b) PCS of a 0.1 μm thick 8CB at a wavelength of at 532 nm and an 3.5° off-specular angle (homodyne) [64].

Figure 6.9 indicates the difference between heterodyne XPCS and homodyne light scattering measurements done using x-ray and laser light, respectively. Figure 6.9a gives specular XPCS data for a thinner 8CB sample that shows in addition to the exponential decay oscillations. The direct consequence of the Siegert relation is that $g_2(t) \geq 1$. For oscillating modes observed in heterodyne case the relevant correlation function $g_1(t)$ is given by scheme an exponentially damped oscillation of the correlation function is given by

$$g_2(t) = 1 + \beta_{\text{het}} \cos(\omega t) \exp(-\Gamma t). \tag{6.5}$$

In homodyne case we get using Siegert relation the following expression for the relevant correlation function $g_2(t)$:

$$g_2(t) = 1 + \beta_{\text{hom}} \cos^2(\omega t) \exp(-2\Gamma t). \tag{6.6}$$

Eqs. 6.5 and 6.6 indicate that the difference in the form of oscillations observed in XPCS and light scattering is due defined by $\cos$ and $\cos^2$ factors, respectively.

Heterodyne detection is more sensitive, as the weak quasi-elastic intensity is not modulated by itself but by the strong elastic signal. In classical dynamic light scattering, one cannot measure at the specular position, and, to take advantage of the heterodyne scheme, an artificial secondary source must be created at off-specular positions. The above discussion suggests that for x rays the elastic intensity at the Bragg reflection or at any other specular position with

enough intensity, can act as a 'natural' secondary source. This opens up new opportunities for probing the dynamics of a variety of systems that produce intense x-ray diffraction patterns, by performing XPCS measurements at Bragg reflections.

6.6 Conclusions

Smectic membranes can be made with an extraordinary uniformity while at the same time they are very stable in the x-ray beam. In combination with the existence of low-dimensional fluctuations these properties make them very suitable for XPCS, allowing in-depth investigations of the technique. We have discussed how in XPCS experiments the coherence properties of the beam influence the time dependence of the measured intensity correlations. The basic assumption is that the coherence volume acts like a filter, selecting fluctuations of the smectic membrane with matching wavelength. Measurements at different scattering angles support this model. Changing the resolution of the setup by variation of the detector slits also influences the time behavior of the correlation function. This indicates a relation with the size of the scattering volume. Both effects can be incorporated in an 'effective' resolution of the setup that accounts for both the resolution and the coherence of the beam. Clear evidence has been provided for a transition in XPCS between heterodyne detection at the specular ridge and homodyne detection for off-specular scattering geometries. In particular a difference in relaxation time of a factor 2 is found as expected. In addition, by comparing propagating modes at the specular ridge (XPCS) and at off-specular positions (PCS with visible light), $\cos$-like and $\cos^2$-like oscillations have been observed as expected for heterodyne and homodyne mixing, respectively. For XPCS heterodyning occurs because of a strong elastic signal present at the specular ridge that acts as a time-independent internal reference source.

Bibliography

[1] P. G. de Gennes and J. Prost, *The physics of liquid crystals*, Oxford, Clarendon Press, 1993.

[2] G. Vertogen and W. H. de Jeu, *Thermotropic Liquid Crystals Fundamentals*, Springer Verlag, 1988.

[3] G. Friedel, Ann. Phys. **18**, 273 (1922).

[4] C. Y. Young, R. Pindak, N. A. Clark, and R. B. Meyer, Phys. Rev. Lett. **40**, 773 (1978).

[5] C. Rosenblatt, R. Pindak, N. A. Clark, and R. B. Meyer, Phys. Rev. Lett. **42**, 1220 (1979).

[6] D. E. Moncton and R. Pindak, Phys. Rev. Lett. **43**, 701 (1979).

[7] P. Pieranski, L. Beliard, J. P. Tournellec, X. Leoncini, C. Furtlehner, H. Dumoulin, E. Riou, B. Jouvin, J. P. Fénerol, P. Palaric, J. Heuving, B. Cartier, and I. Kraus, Physica A **194**, 364 (1993).

[8] W. H. de Jeu, B. I. Ostrovskii, and A. N. Shalaginov, Rev. Mod. Phys. **75**, 181 (2003).

[9] L. D. Landau and E. M. Lifshitzt, *Theory of elasticity*, Oxford, Butterworth-Heinemann, 1999.

[10] R. Hołyst, Phys. Rev. A **44**, 3692 (1991).

[11] R. E. Peierls, Proc. Cambridge Philos. Soc. **32**, 477 (1934).

[12] L. D. Landau, Phys. Z. Sowjetunion **11**, 26 (1937).

[13] A. Caillé, C. R. Acad. Sci. Ser. B **274**, 891 (1972).

[14] L. Gunther, Y. Imry, and J. Lajzerowicz, Phys. Rev. A **22**, 1733 (1980).

[15] J. Als-Nielsen, J. D. Litster, R. J. Birgeneau, M. Kaplan, C. R. Safinya, A. Lindegaard-Andersen, and S. Mathiesen, Phys. Rev. B **22**, 312 (1980).

[16] C. R. Safinya, D. Roux, G. S. Smith, S. K. Sinha, P. Dimon, N. A. Clark, and A. M. Belloq, Phys. Rev. Lett. **57**, 2718 (1986).

[17] V. M. Kaganer, B. I. Ostrovskii, and W. H. de Jeu, Phys. Rev A **44**, 8158 (1991).

[18] See, for example, P. M. Chaikin and T. C. Lubensky, *Principles of Condensed Matter Physics* (Cambridge University Press, Cambridge, England, 1995).

[19] M. Tolan, *X-ray Scattering from Soft-Matter Thin Films*, volume 148 of *Springer Tracts in Modern Physics*, Springer, Berlin, 1999.

[20] J. D. Shindler, E. A. L. Mol, A. N. Shalaginov, and W. H. de Jeu, Phys. Rev. Lett. **74**, 722 (1995).

[21] E. A. L. Mol, J. D. Shindler, A. N. Shalaginov, and W. H. de Jeu, Phys. Rev. E **54**, 536 (1996).

[22] E. A. L. Mol, G. C. L. Wong, J. M. Petit, F. Rieutord, and W. H. de Jeu, Phys. Rev. Lett. **79**, 3439 (1997).

[23] E. A. L. Mol, *Fluctuations in freely suspended smectic A films*, PhD thesis, FOM Institute AMOLF, Amsterdam, 1997.

[24] B. J. Berne and R. Pecora, *Dynamic light scattering with applications to chemistry, biology and physics*, Dover Publications, Inc., 2000.

[25] B. Chu, *Laser Light Scattering: Basic Principles and Practice*, Academic Press, San Diego, USA, 1991.

[26] G. Grübel and F. Zontone, J. Alloys and Compounds **362**, 3 (2004).

[27] S. Dierker, NSLS Newsletter , July 1 (1995).

[28] G. Grübel and D. L. Abernathy, Proc. SPIE **3154**, 103 (1997).

[29] O. Diat, T. Narayanan, D. L. Abernathy, and G. Grübel, Curr. Opin. Coll. Int. Sci. **3**, 305 (1998).

[30] D. L. Abernathy, G. Grübel, S. Brauer, I. McNulty, G. B. Stephenson, S. G. J. Mochrie, A. R. Sandy, N. Mulders, and N. Sutton, J. Synchrotron Radiat. **5**, 37 (1998).

[31] M. Itoh, Jpn. J. Appl. Phys. **38**, 638 (1999).

[32] D. Lumma, L. B. Lurio, S. G. J. Mochrie, and M. Sutton, Rev. Sci. Instrum. **71**, 3274 (2000).

[33] T. Seydel, A. Madsen, M. Sprung, M. Tolan, G. Grübel, and W. Press, Rev. Sci. Instrum. **74**, 4033 (2003).

[34] M. Sutton, K. Laaziri, F. Livet, and F. Bley, Opt. Expr. **11**, 2268 (2003).

[35] S. Brauer, G. B. Stephenson, M. Sutton, R. Bruning, E. Dufresne, S. G. J. Mochrie, G. Grübel, J. Als-Nielsen, and D. L. Abernathy, Phys. Rev. Lett. **74**, 2010 (1995).

[36] S. B. Dierker, R. Pindak, R. M. Fleming, I. K. Robinson, and L. Berman, Phys. Rev. Lett. **75**, 449 (1995).

[37] F. Livet, F. Bley, R. Caudron, E. Geissler, D. Abernathy, C. Detlefs, G. Grübel, and M. Sutton, Phys. Rev. E **63**, 036108 (2001).

[38] L. M. Stadler, B. Sepiol, J. W. Kantelhardt, I. Zizak, G. Grübel, and G. Vogl, Phys. Rev. B **69**, 224301 (2004).

[39] S. G. J. Mochrie, A. M. Mayes, A. R. Sandy, M. Sutton, S. Brauer, G. B. Stephenson, D. L. Abernathy, and G. Grübel, Phys. Rev. Lett. **78**, 1275 (1997).

[40] O. K. C. Tsui and S. G. J. Mochrie, Phys. Rev. E **57**, 2030 (1998).

[41] T. Thurn-Albrecht, G. Meier, P. Müller-Buschbaum, A. Patkowski, W. Steffen, G. Grübel, D. L. Abernathy, O. Diat, M. Winter, M. G. Koch, and M. T. Reetz, Phys. Rev. E **59**, 642 (1999).

[42] L. B. Lurio, D. Lumma, A. R. Sandy, M. A. Borthwick, P. Falus, S. G. J. Mochrie, J. F. Pelletier, M. Sutton, L. Regan, A. Malik, and G. B. Stephenson, Phys. Rev. Lett. **84**, 785 (2000).

[43] D. O. Riese, W. L. Vos, G. H. Wegdam, F. J. Poelwijk, D. L. Abernathy, and G. Grübel, Phys. Rev. E **61**, 1676 (2000).

[44] G. Grübel, D. L. Abernathy, D. O. Riese, W. L. Vos, and G. H. Wegdam, J. Appl. Crystallogr. **33**, 424 (2000).

[45] D. Lumma, L. B. Lurio, M. A. Borthwick, P. Falus, and S. G. J. Mochrie, Phys. Rev. E **62**, 8258 (2000).

[46] T. Seydel, A. Madsen, M. Tolan, G. Grübel, and W. Press, Phys. Rev. B **63**, 3409 (2001).

[47] J. Lal, D. L. Abernathy, L. Auvray, O. Diat, and G. Grübel, Euro. Phys. J. E **4**, 263 (2001).

[48] M. Tolan, T. Seydel, A. Madsen, G. Grübel, W. Press, and S. K. Sinha, Appl. Surf. Sci. **182**, 236 (2001).

[49] H. Kim, A. Rühm, L. B. Lurio, J. K. Basu, J. Lal, D. Lumma, S. G. J. Mochrie, and S. K. Sinha, Phys. Rev. Lett. **90**, 068302 (2003).

[50] A. Madsen, J. Als-Nielsen, and G. Grübel, Phys. Rev. Lett. **90**, 085701 (2003).

[51] S. G. J. Mochrie, L. B. Lurio, A. Rühm, D. Lumma, M. Borthwick, P. Falus, H. J. Kim, J. K. Basu, J. Lal, and S. K. Sinha, Physica B **336**, 173 (2003).

[52] A. Madsen, B. Struth, and G. Grübel, Physica B **336**, 216 (2003).

[53] A. Madsen, T. Seydel, M. Sprung, C. Gutt, M. Tolan, and G. Grübel, Phys. Rev. Lett. **92**, 096104 (2004).

[54] H. Y. Kim, A. Ruhm, L. B. Lurio, J. K. Basu, J. Lal, S. G. J. Mochrie, and S. K. Sinha, Mat. Sci Eng. C **24**, 11 (2004).

[55] S. K. Sinha, Radiat. Phys. Chem. **70**, 633 (2004).

[56] A. C. Price, L. B. Sorensen, S. D. Kevan, J. Toner, A. Poniewierski, and R. Hołyst, Phys. Rev. Lett. **82**, 755 (1999).

[57] A. Fera, I. P. Dolbnya, G. Grübel, H. G. Muller, B. I. Ostrovskii, A. N. Shalaginov, and W. H. de Jeu, Phys. Rev. Lett. **85**, 2316 (2000).

[58] I. Sikharulidze, I. P. Dolbnya, A. Fera, A. Madsen, B. I. Ostrovskii, and W. H. de Jeu, Phys. Rev. Lett. **88**, 115503 (2002).

[59] I. Sikharulidze, B. Farago, I. Dolbnya, A. Madsen, and W. H. de Jeu, Phys. Rev. Lett. **91**, 165504 (2003).

[60] A. Böttger and J. G. H. Joosten, Europhys. Lett. **4**, 1297 (1987).

[61] F. Nallet, D. Roux, and J. Prost, J. Phys. (Paris) **50**, 3147 (1989).

[62] J. C. Earnshaw, Appl. Opt. **36**, 7583 (1997).

[63] C. D. Cantrell, Phys. Rev. A **1**, 672 (1970).

[64] W. H. de Jeu, A. Madsen, I. Sikharulidze, and S. Sprunt, Physica B **355**, in press (2005).

[65] C. Gutt, T. Ghaderi, V. Chamard, A. Madsen, T. Seydel, M. Tolan, M. Sprung, G. Grübel, and S. K. Sinha, Phys. Rev. Lett. **91**, 076104 (2003).

[66] D. Langevin, editor, *Light Scattering by Liquid Surfaces and Complementary Techniques*, New York, Dekker, 1992.

[67] S. K. Sinha, M. Tolan, and A. Gibaud, Phys. Rev. B **57**, 2740 (1998).

[68] D. Sentenac, A. Shalaginov, A. Fera, and W. H. de Jeu, J. Appl. Cryst. **33**, 130 (2000).

[69] B. Lengler, Naturwissenschaften **88**, 249 (2001).

[70] F. Mezei, Z. Phys. **255**, 146 (1972).

[71] F. Mezei, Fundamental of neutron spin echo spectroscopy, in *Neutron spin echo spectroscopy. Basics, trends and applications*, volume 601 of Lecture Notes in Physics, Springer, 2003.

[72] A. Fera, *Ordering and fluctuations in smectic membranes*, PhD thesis, FOM Institute AMOLF, Amsterdam, 2001.

[73] The deuteration (97%) was carried out by H. Zimmerman, Max-Planck Institut für Medizinische Forschung, Heidelberg, Germany.

[74] I. Sikharulidze, I. P. Dolbnya, A. Madsen, and W. H. de Jeu, Optics Commun. **245**, in press (2005).

[75] C. Rosenblatt and N. Amer, Appl. Phys. Lett. **36**, 432 (1980).

[76] I. Kraus, P. Pieranski, E. Demikhov, H. Stegemeyer, and J. Goodby, Phys. Rev. Lett. **48**, 1916 (1993).

[77] T. Thurn-Albrecht, F. Zontone, G. Grübel, W. Steffen, P. Muller-Buschbaum, and A. Patkowski, Phys. Rev. E **68**, 031407 (2003).

[78] A. Q. R. Baron, Hyperfine Interactions **125**, 29 (2000).

[79] J. C. Géminard, C. Laroche, and P. Oswald, Phys. Rev. E **58**, 5923 (1998).

[80] A. Zywocinski, F. Picano, P. Oswald, and J. C. Géminard, Phys. Rev. E **62**, 8133 (2000).

[81] B. Farago, Physica B **268**, 270 (1999).

[82] F. Kohlrausch, Pogg. Ann. Phys. **119**, 352 (1863).

[83] G. Williams and D. C. Watts, Trans. Faraday Soc. **66**, 80 (1970).

[84] A. Arbe, J. Colmenero, M. Monkenbusch, and D. Richter, Phys. Rev. Lett. **81**, 590 (1998).

[85] A. N. Shalaginov and V. P. Romanov, Phys. Rev. E **48**, 1073 (1993).

[86] A. Y. Valkov, V. P. Romanov, and A. N. Shalaginov, Sov. Phys.−Usp. **37**, 139 (1994).

[87] A. Poniewierski, R. Hołyst, A. C. Price, L. B. Sorensen, S. D. Kevan, and J. Toner, Phys. Rev. E **58**, 2027 (1998).

[88] H.-Y. Chen and D. Jasnow, Phys. Rev. E **61**, 493 (2000).

[89] L. V. Mirantsev, Phys. Rev. E **62**, 647 (2000).

[90] A. N. Shalaginov and D. E. Sullivan, Phys. Rev. E **62**, 699 (2000).

[91] V. P. Romanov and S. V. Ul'yanov, Phys. Rev. E **63**, 031706 (2001).

[92] S. V. Ul'yanov, Phys. Rev. E **65**, 021706 (2002).

[93] S. Mora and J. Daillant, Eur. Phys. J. B **27**, 417 (2002).

[94] V. P. Romanov and S. V. Ul'yanov, Sov. Phys.−Usp. **46**, 915 (2003).

[95] I. A. Vartanyants and I. K. Robinson, Opt. Commun. **222**, 29 (2003).

[96] M. Born and E. Wolf, *Principles of Optics*, Pergamon Press, Oxford, 1964.

[97] W. Leitenberger, H. Wendrock, L. Bischoff, T. Panzner, U. Pietsch, J. Grenzer, and A. Pucher, Physica B **336**, 63 (2003).

Summary

This thesis describes x-ray photon correlation spectroscopy (XPCS) and neutron spin echo (NSE) measurements of fluctuations in smectic A (SmA) liquid crystal membranes. XPCS is a classic dynamic light scattering technique extended into the x-ray domain, which opens the possibility to investigate dynamics at molecular length scales. Using a spatially coherent x-ray source available these days at third-generation synchrotrons, the time dependence of the scattered intensity is observed. In XPCS experiments spatially coherent x rays are used while working with a single coherence volume. The scattered intensity changes parallel to the positions of the scatterers in the coherence volume. Constructing the intensity-intensity time correlation function one can extract the relaxation times of the fluctuations in the system. We have extended this technique into the sub-microsecond range, approaching the limit of 2.8 ns determined by the bunch structure of the current in the storage ring of the synchrotron. This allows a comparision with NSE spectroscopy which covers times up to about 100 ns.

Smectic liquid crystal membranes are highly uniformly ordered, strongly fluctuating and scattering systems that constitute excellent models of low-dimensional ordering. SmA liquid crystal membranes consist of stacks of liquid layers of elongated molecules (no positional ordering within the layers). Consequently, one-dimensional ordering exists along the normal to the layers. Thermal fluctuations in such a system increase with the sample size and eventually destroy the ordering (Landau-Peierls instability). Nevertheless, SmA membranes can be prepared with thicknesses ranging from two to several thousand layers, because the divergence of the fluctuations is weak (logarithmic). We have studied three SmA liquid crystals: 4-octyl-4′-cyanobiphenyl (8CB), N-(4-n-butoxybenzilidene)-4-n-octylaniline (4O.8) and 4-heptyl-2-[4-(2-perfluorhexylethyl)phenyl]-pyrimidin (FPP). 8CB differs from the other two by a strongly

polar end group, 4O.8 is characterized by fast equilibration, and FPP membranes are specific because of the presence of fluorine, leading to strong scattering and a low surface tension.

The relaxation behaviour in smectic membranes can be divided into three regimes, characterized by oscillatory relaxation, surface dominated and bulk-elasticity dominated exponential relaxation, respectively. The determining quantity is the largest wavelength from the full spectrum of fluctuations that contributes to the specific situation. Oscillatory relaxations are observed at specular positions for long-wavelength fluctuations. A transition from oscillatory to exponential relaxation is determined by a crossover wave vector q_c. Only fluctuations with wave vectors $q_{mn} > q_c$ show exponential relaxation, which is in first instance surface dominated. The relaxation time in this regime depends on membrane thickness, surface tension and viscosity and does not depend on bulk smectic elastic parameters. Hence, for surface-dominated relaxation the membrane behaves like a liquid film. For larger wave vectors (shorter wavelengths) the relaxation time becomes dependent on the elastic moduli of the membrane while the dependence on membrane thickness and surface tension disappears. In this bulk-elasticity dominated regime the fluctuation pattern is defined exclusively by the bulk smectic elasticity of the membrane. The relaxation time now decreases as $1/q_{mn}^2$ with the wave vector of the fluctuation.

Using XPCS at the Bragg position we observed in thin 4O.8 and 8CB membranes oscillatory relaxations, and in thicker membranes simple exponential relaxation. In contrast, in FPP samples at the first Bragg reflection only oscillatory relaxations were seen. Only by going to the second-order peak we found in FPP exponential relaxation. This can be understood as follows. The finite resolution of the x-ray setup and the size of the coherence volume create a 'window' of wave vectors defining the experimental results. The position of the crossover wave vector q_c in this window determines whether oscillatory or exponential relaxation is observed. As q_c decreases with the thickness of the membrane as $1/\sqrt{L}$, in thin membranes the wave vector 'window' is dominated by fluctuations exhibiting oscillatory relaxations, while in thicker samples exponential relaxation prevails. For off-specular scattering geometries only single fluctuations were probed with a wave vector defined by the rocking angle of the sample. For XPCS, which allows only relatively small offset angles because of intensity considerations, only the surface-dominated exponential relaxation regime was accessed. Scattering at far off-specular angles was possible with NSE revealing the $1/q_{mn}^2$ decay of the relaxation time characteristic for the bulk-elasticity regime.

The role of the coherence volume in determining the 'window' of detected fluctuations was demonstrated in a series of measurements at the different specular scattering angles and for different settings of the detector slits. The results indicate that the relaxation shifts towards larger times for smaller scattering angles, because of the larger coherence volume due to the increased projection of the beam on the membrane surface. Variation of the setting of the detector slits resulted, apart from changes in contrast, also in small shifts of the relaxation times. Finally, XPCS measurements at various off-specular positions close to the specular ridge indicate that the form of the correlation function changes abruptly. Close to specular reflection the finite resolution of the x-ray set-up catches the elastic specular component related to the equilibrium structure of the membrane. This signal acts as a 'natural' reference signal in addition to the fluctuating part, leading to mixing in a heterodyne detection scheme. In the diffuse tails of a rocking curve this reference signal is absent leading to homodyne detection.

Samenvatting

In dit proefschrift wordt het fluctuatiegedrag van smectische A (SmA) vloeibaar kristallijne membranen onderzocht met behulp van *X-ray Photon Correlation Spectroscopy* (XPCS) en *Neutron Spin Echo* (NSE) experimenten. XPCS is een klassieke dynamische lichtverstrooiingstechniek waarbij de tijdsafhankelijkheid van de verstrooide intensiteit wordt geregistreerd, uitgebreid naar het gebied van de röntgenstraling. Dit maakt het mogelijk om dynamische eigenschappen van de materie op het moleculaire niveau te onderzoeken. Een en ander vereist een bron van coherente röntgenstraling, tegenwoordig beschikbaar bij synchrotrons van de derde generatie. In XPCS experimenten wordt de verstrooiing aan één coherente deelvolume in het preparaat gemeten. De verstrooide intensiteit verandert met de posities van de verstrooiende objecten binnen het coherente volume in het preparaat. Berekening van de correlatiefunctie van de intensiteiten in het tijdsdomein geeft de karakteristieke relaxatietijd van de fluctuaties. We hebben deze techniek uitgereid tot het submicroseconde gebied, tot dicht bij de limiet van 2.8 ns welke bepaald wordt door de gepulste structuur van de stroom in het synchrotron. Dit maakt overlap mogelijk met NSE methoden die een tijdschaal tot ongeveer100 ns bestrijken.

Smectische vloeibaar kristallijne membranen zijn uniforme, geordende, sterk fluctuerende en verstrooiende systemen die een excellent model vormen voor de bestudering van laag-dimensionale ordening. SmA membranen bestaan uit een stapeling van vloeibare lagen van langgerekte moleculen (geen ordening van de posities in de lagen). Kenmerkend is dus één-dimensionale ordening van de moleculen in de richting loodrecht op het oppervlak. In een dergelijk systeem nemen de thermische fluctuaties toe met de grootte van het preparaat, waardoor ze uiteindelijk de ordening te niet doen (Landau-Peierls instabiliteit). Toch is het mogelijk stabiele SmA membranen te maken met een dikte van twee tot enkele duizenden lagen, omdat

de divergentie van fluctuaties langzaam verloopt (logaritmisch). We hebben een drietal SmA vloeibare kristallen onderzocht: 4-octyl-4′-cyanobiphenyl (8CB), N-(4-*n*-butoxybenzilidene)-4-*n*-octylaniline (4O.8) en 4-heptyl-2-[4-(2-perfluorhexylethyl)phenyl]-pyrimidin (FPP). 8CB onderscheid zich door een sterk polaire eindgroep, 4O.8 membranen bereiken snel een stabiel evenwicht, terwijl de aanwezigheid van fluor in FPP leidt tot sterke röntgenverstrooiing en een lage oppervlaktespanning.

Het relaxatiegedrag van SmA membranen kan in drie regimes verdeeld worden, gekenmerkt door (1) oscillerende relaxatie, en daarnaast exponentieel verlopende relaxatie gedomineerd door (2) de oppervlaktespanning en (3) door het bulk elastisch gedrag. De beslissende parameter is de grootste golflengte uit het volledige spectrum van fluctuaties die in een bepaalde situatie bijdraagt tot de verstrooiing. Oscillerende relaxaties worden geregistreerd voor speculaire posities en fluctuaties met een grote golflengte. De overgang van oscillerende relaxaties naar het exponentiele regime wordt bepaald door de een golfvector q_c. Alleen fluctuaties met een golfvector $q_{mn} > q_c$ leiden tot exponentiele relaxatie. In eerste instantie hangt de relaxatietijd in dit regime af van de dikte, de oppervlaktespanning en de viscositeit van het membraan en is onafhankelijk van de smectische elasticiteit. Het smectische membraan kan in dit geval dus als een conventioneel vloeibaar membraan beschouwd worden. Voor grotere golfvectoren (kleinere golflengtes) wordt de relaxatietijd in toenemende mate afhankelijk van de elastische moduli van het membraan. De afhankelijkheid van de dikte en de oppervlaktespanning verdwijnen. Uiteindelijk wordt de relaxatie volledig gedomineerd door de smectische volume-elasticiteit. In dit regime varieert de relaxatietijd volgens $1/q_{mn}^2$ met de bepalende golfvector q_{mn} van de fluctuatie.

XPCS experimenten op de Bragg positie geven in dunne 4O.8 en 8CB membranen oscillerende en in dikkere membranen exponentiële relaxaties aan. FPP preparaten tonen voor de eerste Bragg reflectie alleen oscillerende relaxaties, maar voor de tweede Bragg piek wordt exponentiële relaxatie gevonden. Deze resultaten kunnen op de volgende wijze kunnen worden geïnterpreteerd. Het oplossend vermogen van de röntgenapparatuur enerzijds en de grootte van het coherente volume anderzijds, creëren samen een ′venster′ van toegestane golfvectoren welke het resultaat van de XPCS metingen bepalen. Het oscillerende of exponentiele karakter van de relaxatie hangt af van the positie van q_c binnen dit ′venster′. Voor membranen met toenemende dikte L neemt q_c af volgens $1\sqrt{L}$. Binnen het ′venster′ worden dan fluctuaties met een exponentiële relaxatie dominant. Voor dunnere membranen neemt de bijdrage van de oscillerende fluctuaties toe, omdat q_c groter wordt en daardoor binnen het ′venster′ kortere

golflengtes domineren. Door te meten bij niet-speculaire verstrooiingshoeken kan de grootste golfvector die gemeten wordt gecontroleerd worden. In deze situatie is de relaxatie van oppervlakte gedomineerde fluctuaties gemeten. Verstrooiing bij grotere niet-speculare hoeken kon gemeten worden met NSE, waarbij de $1/q_{mn}^2$ afhankelijkheid van de relaxatietijd is gevonden welke karakteristiek is voor het elastische gedomineerde regime.

De rol van coherente gebieden binnen de definitie van het 'venster' is geïllustreerd door metingen bij verschillende speculare posities en met verschillende openingshoeken van de detector. De relaxatie bij kleinere verstrooiingshoeken verschuift naar langere tijden, in overeenstemming met een groter coherent volume vanwege de grotere projectie van de invallende röntgenbundel op het membraanoppervlak. Veranderingen van de openingshoek van de detector leiden naast een variatie in contrast ook tot kleine verschuivingen van de relaxatie profielen. Ten slotte tonen XPCS metingen rondom de speculaire Bragg positie een verandering in de vorm van de correlatie functie. Vanwege het eindige oplossend vermogen van het instrument wordt dicht bij de speculaire positie een sterk elastische signaal gedetecteerd. Deze component wordt bepaald door evenwichtstructuur van het smectische membraan en speelt een rol als 'intrinsiek' referentie signaal dat mengt met de fluctuerende intensiteit in een heterodyne detectieschema. Bij grotere niet-speculaire hoeken is dit signaal afwezig hetgeen resulteert in homodyne detectie.

Curriculum Vitae

Irakli Sikharulidze was born on June 1, 1977 in Tbilisi, Georgia. In 1994 he was admitted to the Faculty of Physics of M.V. Lomonosov Moscow State University. He specialized in polymer physics in the Department of Physics of Polymers and Crystals (Prof.dr. Alexei R. Khokhlov). During his studies he spent one semester at the Humboldt-Universität zu Berlin in the group 'Physics of Macromolecules' (Prof.dr. Jürgen P. Rabe). Irakli Sikharulidze obtained in 1998 his BSc degree and in 2000 his MSc degree in physics. The MSc thesis work 'A SAXS study of the lamellar crystallization of symmetric diblock copolymers' was completed under the supervision of Prof.dr.ir. Wim H. de Jeu in the group 'Order/Disorder in Soft Matter' at the FOM-Institute for Atomic and Molecular Physics in Amsterdam. After his graduation Irakli Sikharulidze returned to work in the same group on a PhD project, investigating relaxations in smectic liquid crystal membranes using x-ray photon correlation spectroscopy and neutron spin echo techniques. The result of this work has been presented in this thesis. Since January 2005 Irakli Sikharulidze is employed in the group 'Biophysical Structural Chemistry' (Prof.dr. Jan Pieter Abrahams) at the Leiden Institute of Chemistry.